First-Principles Modeling and Experimental Investigation of Novel Materials for Energy Storage

by

Isaac M. Markus

A dissertation submitted in partial satisfaction of the

requirements for the degree of

Doctor of Philosophy

in

Engineering - Material Science and Engineering

in the

Graduate Division

of the

University of California, Berkeley

Committee in charge:

Professor Mark Asta, Co-chair
Dr. Marca Doeff, Co-chair
Professor Kristin Persson
Professor Bryan D. McCloskey

Summer 2016

First-Principles Modeling and Experimental Investigation of Novel Materials for Energy Storage

Abstract

First-Principles Modeling and Experimental Investigation of Novel Materials for Energy Storage

by

Isaac M. Markus

Doctor of Philosophy in Engineering - Material Science and Engineering

University of California, Berkeley

Professor Mark Asta, Co-chair

Dr. Marca Doeff, Co-chair

The following dissertation presents several studies aimed at better understanding the behavior of different materials employed in energy storage and conversion applications with the goal of putting forth design criteria that can enhance the performance of fuel cells and batteries with different chemistries. The third chapter models the ion conduction in the rare earth phosphate $DyPO_4$. This material is investigated for use in intermediate temperature solid oxide fuel cells, and the results highlight the benefits for proton conduction associated with a higher symmetry structure, relative to previously studied orthophosphate solid electrolyte materials. The fourth and fifth chapter combines modeling and experiments to understand why Ti substitution of Co in the cathode material $Li(Ni_xMn_xCo_{1-2x})O_2$ results in enhanced capacity and cyclability when used in lithium ion batteries. The results of these studies show that Ti substitution results in a lower intercalation voltage that allows for higher lithium extraction given a set voltage cut-off. Further results indicate that Ti helps suppress the formation of a secondary rocksalt phase that reduces cell efficiency.

The sixth chapter investigates the intercalation mechanism of Li and Na into alkali titanate compounds that are of interest as anode materials in lithium-ion or sodium-ion batteries. The goal is to elucidate the susceptibility of each kind of titanate to phase transformations during the lithiation or sodiation process in a functioning battery. The results indicate that these materials fail to deliver theoretical capacities due to site limitations, that can be further aggravated by solvent uptake. Analysis of sodium energy barriers reveal a strong dependence on the state of charge, and potentially the rate of charging.

The seventh chapter investigates electrolyte concentration effects in lithium-oxygen batteries. The model electrolyte system of lithium triflimide (LiTFSI) dissolved in 1,2- dimethoxyethane (DME) is investigated in order to identify different contributions to the failure mechanism of this class of battery. Combined experimental and computational results indicated that the TFSI anion was susceptible to decomposition, which contributed to cathode passi-

vation in cells employing saturated electrolyte, and to kinetic limitations in cells using dilute electrolytes.

The combined work of this dissertation serves to demonstrate the capabilities of a combined experimental and computational approach to understanding and solving the challenges revolving energy storage and conversion materials. The ability to provide atomistic insights to experimental results allows the creation of design criteria for next generation materials, that leverage the insights gained from this combined approach.

To the people that raise me up and let me fly

Contents

List of Figures

List of Tables

Acknowledgments

I am forever grateful to the mentors that have guided and shaped my research work. Professor Mark Asta, for giving me the chance to come to Berkeley, advising me along this path, and allowing me the freedom to succeed my way. Dr. Marca Doeff for giving me a research direction, full of support and encouragement. Professor Lutgard De Jonghe, for the early mentoring and advice. Dr. Jaime Garcia, for her support and guidance as I transition to the next stage of my life.

A special thank you to all the collaborators that worked with me. Dr. Feng Lin, for always being intellectually curious and hungry for answers. Dr. Mona Shirpour, for sharing and helping solve so many interesting problems. Dr. Kinson Kam, for introducing me to the world of batteries and the research lab. Dr. Nicole Adelstein, for helping me acclimate to Berkeley and setting me up for success in all matters of DFT. Dr. Dennis Nordlund and Dr. Tsu-Chien Weng, for all the support in the various synchrotron beam lines. Dr. Huolin Xin, for TEM measurements and research advice. Dr. Gavin Jones, for support and simulation work. Simon Engelke, Alex Guefen, Edgar Olivera, and Silas Wolff-Goodrich for being great students and helping me on so many projects.

Thank you to Professors Kristin Persson, for serving on my qualifying exam, and forming part of my dissertation committee. Bryan McCloskey, for serving on my qualifying exam, and forming part of my dissertation committee. Thomas Devine, for serving and chairing my qualifying exam.

And of course a special thank you to the people that made grad school so much fun, my best amigos Joo Chuan, Jose, Bryan, Shawn, Tim, Will, Ian, Maarten, Charles, Lei, Max, Benson, Christ, Jonathan, and everyone that brighten my days.

Last but not least to the people that have unconditionally supported and loved me. My mom and dad, who sacrificed so much and showed me how reach my dreams, and my wife for being there every step of the way. You are forever in my heart and mind.

Chapter 1

Introduction and Background

1.1 Motivation

Over the last 10 years there has been a social, political, and economic movement toward the development and integration of novel technologies that can help reduce fossil fuel consumption. In the United States this initiative is motivated in part as an effort to reduce foreign dependence on oil, but more importantly, on a global scale it is part of a series of policies intended to help address man-made climate change [1]. In the United States the implementation of such policies has been spearheaded by the Department of Energy (DOE), which has created several focus areas that it has deemed critical to reduce utilization of fossil fuels. Among these are the improvements in energy conversion and storage technologies that can be applied toward modernizing the electrical grid, commercializing electric vehicles, and developing alternative fuels [2]. For each of these applications there still exist complex problems tied to the lack of suitable materials that can perform in a cost effective manner.

Shifting away from a fossil fuel based economy must occur via the adoption of clean energy sources and alternative clean fuels like hydrogen. This strategy depends on the ability of solar and wind to overcome critical hurdles in order to provide the same reliability at a cost competitive level as fossil fuels. Nuclear energy is also a potential solution to this problem, but continues to be hindered by a lack of public support following unforeseen accidents that defy industry claims that this type of energy production can be made safe. From Fig. 1.1 it can be seen how little change there has been in the last ten years in how we produce energy in the United States. For stationary energy production used in residential, commercial and industrial settings, solar and wind energy production has increased by 6.5 times, but still comprise less than 5% of energy generation. For transportation applications, the reliance on petroleum based fuels has continued even with the commercialization of several electric vehicles, with net consumption of petroleum based fuels down only 10% [3, 4].

The challenge each of these sectors face for continued growth can be traced in part to the electrochemical systems that are required to make large commercial deployment possible. Unlike other renewable energy sources, solar and wind energy have less geographical limita-

tion, but because they are intermittent in nature their production can neither be guaranteed or even be possible at all times. Addressing this challenge requires some form of energy storage that can help match energy demand at all times. Given that the most economical forms of energy storage (pumped hydro and compressed air) have geographical limitations and have already been well developed, future advances rely on improving electrochemical systems such as batteries or fuel cells [5].

Throughout this work both experimental and computational techniques are used to explore changes in the performance of various compounds employed in solid oxide fuel cells and batteries, providing atomistic insights that set forth material design considerations for optimal performance. The main computational method employed in this work is density functional theory (DFT), which is a first principles atomistic computational methodology that was developed from the theories of P. Hohenberg, W. Kohn, and L. Sham [6, 7]. Experimentally, a variety of electrochemical and characterization tests are performed depending on the system being studied. Because a wide variety of electrochemical systems were studied in this dissertation, the remainder of this introduction will cover relevant motivation and technical background related to the materials systems studied.

Thermodynamics of Electrochemical Energy Storage and Conversion

The target applications for this work can be categorized into either fuel cells or batteries, both constituting electrochemical systems with many common features. Figure 1.2 presents a typical diagram for a lithium ion battery and a solid oxide fuel cell. As can be seen both systems require an anode and cathode capable of both ionic and electronic conductivity, and an electrolyte that is only an ionic conductor. The setup is intended to physically separate both electrodes in order for each to have either an oxidation or reduction reaction, where the balancing electrons can be utilized for an outside load. One critical distinction between the two systems is that generally batteries represent closed systems while fuel cells are open, meaning that for fuel cell operation external mass must be added for the electrochemical reaction to proceed while batteries are mainly intended to be self contained. Because of this difference, the electrodes of rechargeable batteries must be capable of reversible reduction and oxidation reactions for charge and discharge processes, such that they can efficiently store energy. In comparison fuel cells can remain in a single operation mode converting a fuel such as hydrogen into electrical energy. While batteries are referred to as energy-storage devices, fuel cells are an example of an electrochemical conversion device.

Given that both systems are converting chemical energy into electrical energy their thermodynamic treatment is also similar. Each electrode in the system will represent a half cell having a unique electrochemical potential that is dependent on the sum of the material constituents. Following the notation from Newman et al. [10] the difference between the two potentials gives the Gibbs free energy as described by equation 1:

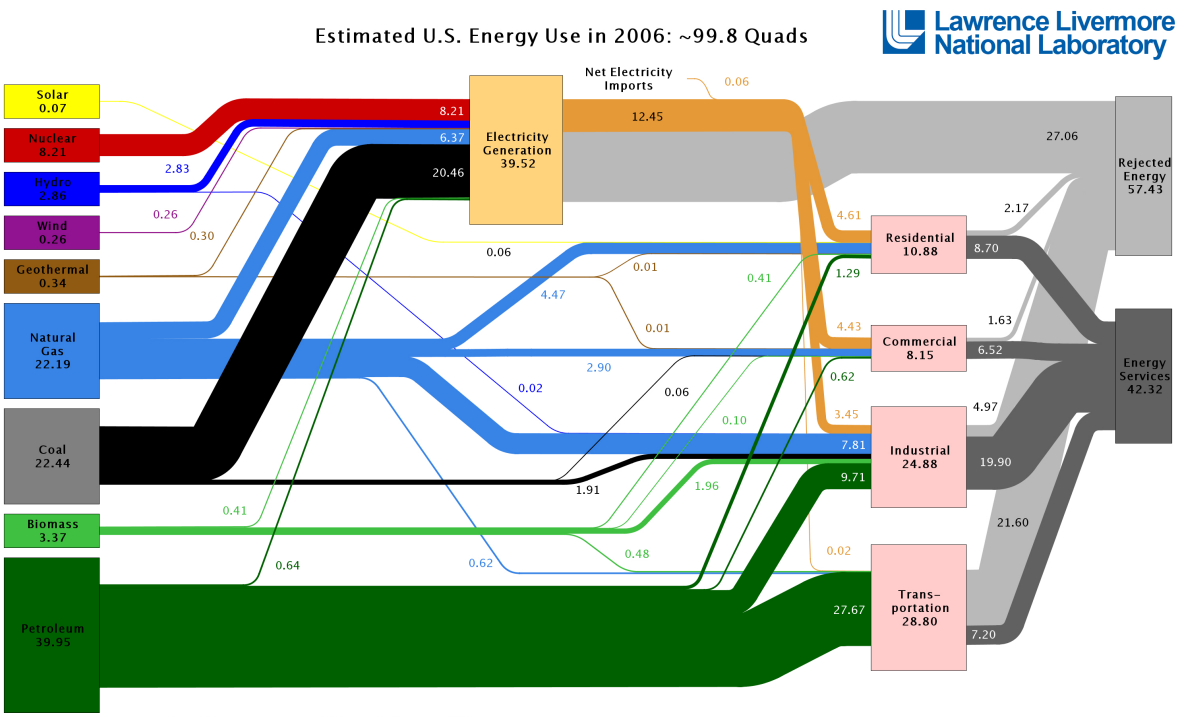

Source: LLNL 2008. Data is based on DOE/EIA-0384(2007), June 2008. If this information or a reproduction of it is used, credit must be given to the Lawrence Livermore National Laboratory and the Department of Energy, under whose auspices the work was performed. Distributed electricity represents only retail electricity sales and does not include self-generation. EIA reports flows for non-thermal resources (i.e., hydro, wind and solar) in BTU-equivalent values by assuming a typical fossil fuel plant "heat rate." The efficiency of electricity production is calculated as the total retail electricity delivered divided by the primary energy input into electricity generation. End use efficiency is estimated as 80% for the residential, commercial and industrial sectors, and as 25% for the transportation sector. Totals may not equal sum of components due to independent rounding. LLNL-MI-410527

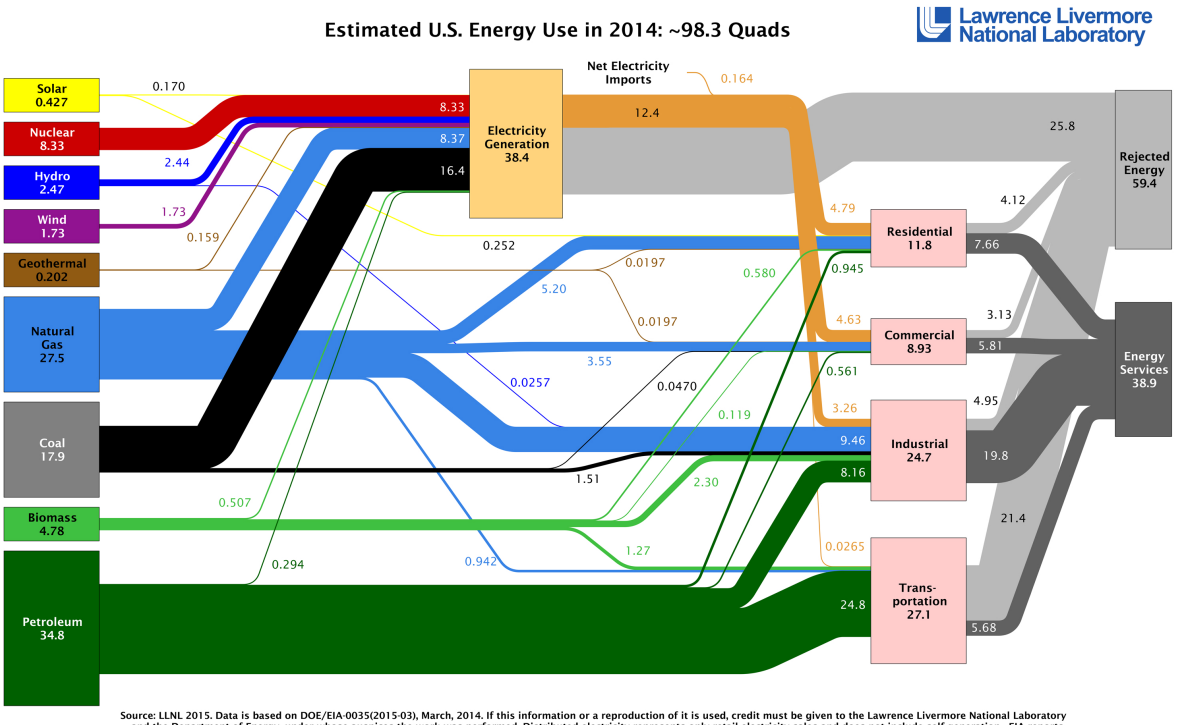

Source: LLNL 2015. Data is based on DOE/EIA-0035(2015-03), March, 2014. If this information or a reproduction of it is used, credit must be given to the Lawrence Livermore National Laboratory and the Department of Energy, under whose auspices the work was performed. Distributed electricity represents only retail electricity sales and does not include self-generation. EIA reports consumption of renewable resources (i.e., hydro, wind, geothermal and solar) for electricity in BTU-equivalent values by assuming a typical fossil fuel plant "heat rate." The efficiency of electricity production is calculated as the total retail electricity delivered divided by the primary energy input into electricity generation. End use efficiency is estimated as 65% for the residential and commercial sectors 80% for the industrial sector, and 21% for the transportation sector. Totals may not equal sum of components due to independent rounding. LLNL-MI-410527

Figure 1.1: Breakdown of the energy source and usage of the United States in 2006 and 2014 [3, 4].

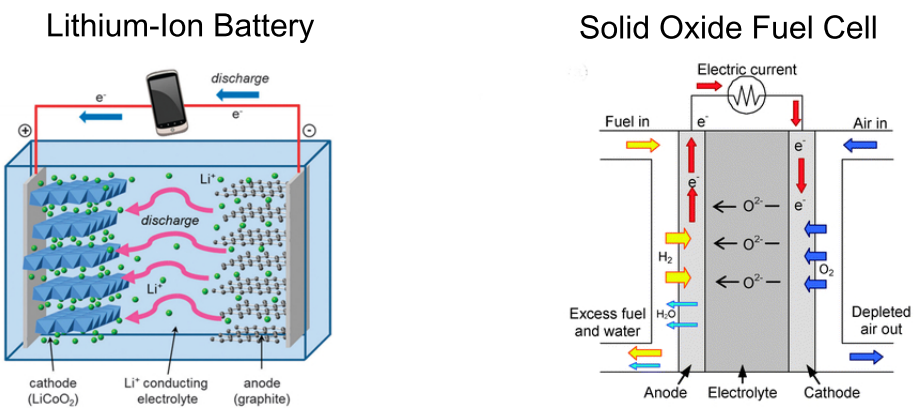

Figure 1.2: Typical battery diagram for a lithium ion battery and a solid oxide fuel cell, showing common components, and functioning mechanism of operation [8, 9].

$$\Delta G = (\sum_i s_i \mu_i)_{electrode1} - (\sum_i s_i \mu_i)_{electrode2} \tag{1.1}$$

where G is the Gibbs free energy, μ_i is the chemical potential of species i, and s_i is the stoichiometric coefficient of species i. When ΔG is negative and the two electrodes are connected the two redox reactions will proceed spontaneously until an equilibrium point is reached. If the two electrodes are connected via an external galvanostat that applies a counter potential to prevent current flow the open circuit potential for the system can be measured, and is described by equation 2:

$$\Delta G = -nFU \tag{1.2}$$

where U is the equilibrium electrostatic potential, F is Faraday's constant, and n is the number of electrons transferred. The importance of Eq. 1.2 is that it provides the means for controlling electrochemical reactions, since depending on the potential applied a reaction can be driven backward or forward. Since this relationship ultimately depends on the compounds involved in each reaction and their concentration its full description requires the following two equations:

$$\mu_i = \mu_i^\theta + RTln(m_i \gamma_i) \tag{1.3}$$

$$U = U^\theta - \frac{RT}{nF} ln(\prod_i m_i^{s_i})_{electrode1} + \frac{RT}{nF} ln(\prod_i m_i^{s_i})_{electrode2} \tag{1.4}$$

where μ_i^θ is the chemical potential independent of concentration, R is the universal gas constant, T is temperature, m_i is the molality of species i, γ_i is the activity coefficient of species i, U^θ is the potential independent from concentration. Equation 1.4 ultimately reduces to the Nersnt equation when the activity coefficients are equal to 1.

Because electrochemical cells permit the control over the direction of chemical reactions they can be divided into two classes, galvanic and electrolytic. The prior type of cell covers the devices in which work is spontaneously produced, this includes fuel cells, primary batteries (non rechargeable), or discharge of secondary batteries (rechargeable). The second type of cell are those that require outside power to drive the chemical reaction, this includes electroplating or the charging of secondary batteries.

1.2 Solid Oxide Fuel Cells

Chapter 3 of this thesis is devoted to the computational investigation of $DyPO_4$ for application as an electrolyte in solid oxide fuel cells (SOFCs). As mentioned previously these are galvanic devices intended to convert chemical energy into electrical energy. Although there are several types of fuel cells, this research has focused particularly on SOFCs which are mainly distinguished by the fact that the electrolyte employed is a solid ceramic capable of conducting ions at temperatures below 1000^o C [9, 11]. These devices have been extensively researched because, unlike traditional combustion engines, their overall efficiencies are not limited by the Carnot cycle. Instead, for SOFCs the overall efficiency is given by:

$$\epsilon = \frac{\Delta G}{\Delta H} \tag{1.5}$$

where ϵ is the efficiency, ΔG and ΔH are the change in Gibbs free energy and enthalpy, respectively, between reactant and products of chemical reaction taking place inside the fuel cells, which for a SOFC employing H_2 as a fuel are:

$$H_2 \rightarrow 2H^+ + 2e^- \tag{1.6}$$

$$\frac{1}{2}O_2 + 2H^+ + 2e^- \rightarrow H_2O \tag{1.7}$$

$$H_2 + \frac{1}{2}O_2 \rightarrow H_2O \tag{1.8}$$

From the chemical reactions, it can also be appreciated that the only waste product is water. Unfortunately, the biggest drawback for SOFCs is that they must operate at temperatures above 600^oC in order to have fast enough oxygen ion diffusion to sustain usable power densities [11, 12]. This leads to higher engineering and operation cost for these devices, limiting the scope of their application. However, because there still exists a wide temperature range between approximately 200^oC and 600^oC, known as the Norby gap [13], where ion diffusion through solids is not fast enough for functional devices, current research is focused on novel electrolyte systems that can operate at this intermediate temperatures. The general approach to fill this gap has been to explore electrolyte materials that are as robust and corrosion resistant as the oxides in SOFC, but that conduct protons like the polymer

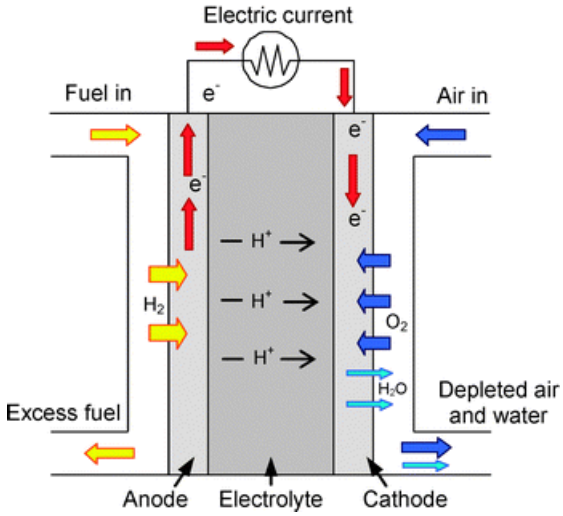

Figure 1.3: Diagram of proton conducting solid oxide fuel cells [9].

membrane fuel cells (PEMFCs) that can operate below 200^oC [14], since this smaller ion has generally a lower activation energy for diffusion. Additionally, this combination is intended to reduce the high operation cost of SOFCs, and eliminate the high material cost of catalysts such as platinum used in PEMFCs [11, 15]. The basis of operation for proton conducting solid oxide fuel cells is dependent on equations 1.6-8 and is summarized by Figure 1.3.

Among the most investigated electrolytes systems are the perovskites $BaCeO_4$, $BaZrO_3$, and $LaMnO_3$ [15, 12], which by complex doping schemes have reached power densities up to 1.5 W/cm^2 at 500^o. However, due to high grain boundary resistance, achieving this high performance requires complex manufacturing, such as the use of pulsed laser deposition, that is not scalable to commercial products. In order to investigate alternatives, several rare earth phosphate compounds have been identified as potential proton-conducting electrolytes. This is motivated by experimental results indicating that doped $LaPO_4$ and $CePO_4$ can reach conductivities between 10^{-3} and 10^{-5} at 800^o S/cm [16], which is comparable to values achieved in the perovskites. However, there are significant variations across the different rare-earth phosphates, from proton uptake to ionic and electronic conductivities, which leaves unanswered several questions regarding transport mechanisms in this class of materials. The work herein seeks to correlate the different crystal structures found in the rare-earth phosphates with different proton transport properties that can be used in the design of next generation devices.

1.3 Batteries

Chapters 4 through 8 of this thesis are dedicated to the investigation of various battery chemistry systems and their material components including lithium-ion, sodium-ion, and lithium-

oxygen batteries (LIBs, NIBs, Li-O_2). The motivation for working on multiple chemistries stems from the broadening scope in which batteries are a limiting factor. Historically the discovery of new energy storage media has permitted the development of numerous other technologies. The lithium-ion battery, which was first commercialized by Sony in 1991 allowed the portable electronic industry to grow exponentially to what we have today, required multiple advances in all its components to be able to work. This included the first intercalation materials synthesized in 1972 by Whittingham at Exxon [17], the eventual discovery of $LiCoO_2$ by Goodenough [18], and the development of organic electrolytes that permitted the formation of a stable solid-electrolyte interphase (SEI) with graphite anodes. However, even with the latest generation of energy dense LIBs, the push for expanded use of renewable energy sources, electric vehicles and increasing living standards across the world, threaten to outpace the available lithium resources worldwide, mandating a need for alternate battery chemistries that can be employed in a cost effective manner [19].

Although each application for energy storage has different constraints, the exploration of alternate battery chemistries is generally guided by the goal of maximizing power or energy density, and longevity while minimizing cost. Achieving this requires a deeper understanding of material behavior at multiple scales, not just to help understand the shortcomings of currently available compounds but to also help in the design and selection of possible alternate compounds. For each chemistry there are multiple approaches to increasing the energy density and longevity of batteries. In this thesis I explored multiple effects that impact at least one of the limiting factors in each system.

Lithium-Ion and Sodium-Ion Electrodes

The success of LIBs is in part due to the high degree of reversibility its electrodes can offer for charging and discharging processes without undergoing chemical or structural decomposition. The class of materials that allows for this are the typical intercalation materials [17, 18], which can reversibly intercalate alkali ions such as lithium for LIBs or sodium for NIBs [20, 8]. The regular mode of operation for such electrodes is that during discharge, the negative electrode (anode) is oxidized, supplying electrons to the outside circuit. These electrons are balanced out by Li^+ or Na^+ that deintercalate from the anode, diffusing across the electrolyte and recombining with the electrons after reinsertion into the positive electrode (cathode). The opposite set of steps occurs during charging, as ions leave the cathode which oxidizes the transition metals that compose it, followed by diffusion across the electrolyte, finalizing with reinsertion of alkali metal ions into the anode in order to recombine with electrons, resulting in the reduction of this electrode. Because LIBs and NIBs are closed systems, several battery metrics that depend on the material components can be theoretically predicted given the compositions of the electrodes, including specific capacities and intercalation voltages. However, it is the multiple side reactions and phase transformations that occur inside the battery that affect lifetime, cycling behavior and safety. This set of reactions and phase transformation are highly system dependant, with material analogues of LIBs and NIBs displaying significantly different behavior, making commong materials for

LIBs such as graphite not applicable to NIBs. A summary of high performance electrodes for LIBs and NIBs are included in Tables 1.1 and 1.2, respectively. From the tables it can be appreciated that each system has its own set of limiting factors, providing a guide for the critical areas of focus to improve performance, cyclability, and safety.

Since the first LIBs were introduced there have been both engineering and material advances that have permitted increased energy storage. On the engineering side, better packaging and manufacturing has resulted in batteries that can pack more active material. From a materials point of view newer materials have been produced that have higher energy densities, since they can reversibly accommodate higher amounts of Li ions per unit mass. However, one of the practical problems in using such materials is that extraction of their theoretical capacities requires moving to higher intercalation voltages, which increases the amount of side reaction and phase transformation that limit safety and longevity of batteries. This type of problem has been typical of the cathode materials, which are widely considered the limiting electrode for capacity. As can be seen in Table 1.1, most anode materials have significantly higher theoretical gravimetric capacities [21, 22], meaning that in a closed system the energy density is strictly set by the lithium content of the cathode, since cell assembly occurs in a discharge state when the cyclable lithium is only present in the cathode. Additionally, because the anode reactions happen close to the plating potential of Li, there is no possibility to increase the voltage window on the anode side without increasing the safety hazards of LIBs. Furthermore, cells are design to prevent anode overlithiation, which means that the amount of anode active material is intentionally higher than needed for the amount of Li present at the cathode. Because of this safety consideration there are newer more energy dense anode materials being actively investigated which can help reduce the amount of active material needed on the anode side. One such material is a silicon, which has ten times the theoretical capacity of graphite, and can theoretically help a battery module increase its specific energy by 30%. However, maximum advantage can only be achieved with higher capacity cathodes that optimize all practical aspect of a battery module.

This general fact means that improvements in the energy density of LIBs requires advances on the cathode materials either by development of new systems with higher capacities that can be accessed in a stable voltage window, or by improvements to the current systems in order to allow them to reach their theoretical values. A third approach, which falls outside the purview of this work, is to focus on developing higher voltage materials. This strategy employs materials with comparable energy densities, that intercalate Li at higher voltages which allows them to deliver higher power densities. However, this requires simultaneous development of electrolytes that are stable in a wider voltage range. In this thesis part of the work focuses on understanding the contributing factors that limit practical capacities of the cathode material $Li(Ni_{1/3}Mn_{1/3}Co_{1/3})O_2$. This compound is more energy dense that the typical $LiCoO_2$ cathode. However, access to the additional capacity of this material occurs at higher voltages which places a practical limit. Chapters 4 and 5 seeks to investigate how specific cation substitution in the cathode $Li(Ni_{1/3}Mn_{1/3}Co_{1/3})O_2$, can result in performance enhancements of up to 15% in capacity and cyclability when employing the same cycling conditions.

Chapter 6 of this thesis shifts focus to the exploration of suitable anodes for NIBs. From Table 1.2 it can be appreciated that the typical graphite anode is not listed, which is due to the fact that this simple and economical carbon phase can not intercalate appreciable amounts of Na ions [20]. Due to a size mismatch, Na encounters unfavorable energetics for intercalation between graphite layers. Alternative soft and hard carbons are required for favorable Na insertion, however, the high temperatures required for the fabrication of such materials creates a disincentive for their application [23, 24, 25]. Furthermore, safety considerations should eliminate carbons from consideration, since intercalation typically occurs very close to the plating potential, which given the higher chemical reactivity of Na presents a high risk for explosions. One alternative class of anode that has worked for LIBs are alloying materials such as Si or Sn. However, the larger Na ion size further aggravates the large volume expansions (>400%) these materials experience during lithiation or sodiation [26, 27, 28]. These drawback results in a lack of energy dense materials that are economical, safe, and reliable, making oxides potentially the only viable option for NIBs. Because these materials have rather low gravimetric capacities, the anode is at present the limiting factor for increasing the energy density in NIBs. To address this situation several sodium titanates with corrugated layered structures were investigated. The work described in chapter 6 focused on novel systems with a specific effort to provide criteria for future material selection and preparation that can help maximize energy densities in NIBS.

Lithium Oxygen Batteries

Given the scale of modern day energy needs, finding electrochemical storage options that can be economically applied requires significant improvements in the energy density and longevity in available devices. Achieving this will not be possible by just gradual increases in batteries that are already available, but instead new chemistries that can offer order-of-magnitude improvements are required. Among such battery systems are those based on the lithium-air or lithium-oxygen (Li-O_2) chemistry. This type of battery has been demonstrated in multiple formats, but the leading option is the non-aqueous lithium-air battery shown in Fig. 1.3. These cells have a specific energy of 3458 W*h/Kg, which is almost 10X the theoretical value for LIBs of 387 W*h/Kg, based on the $LiCoO_2$/C electrodes [31, 32, 33, 34]. However, because the chemistry not only kinetically prevents reaching theoretical values, but also requires additional equipment not necessary in other cell types, most practical estimates project practical specific energy of 500-700 W*h/Kg. Understanding the large discrepancy has required deeper knowledge of the actual mechanisms by which this type of battery operates. The currently accepted mechanism is [32]:

$$2Li \leftrightarrow 2Li^+ + 2e^-(Anode) \tag{1.9}$$

$$Li^+ + e^- + O_2^* \leftrightarrow LiO_2^*(Cathode) \tag{1.10}$$

Table 1.1: Select Electrodes for Lithium-ion Batteries [21, 29, 22, 30]

Framework	Compound	Specific Capacity mAh/g (Practical Capacity)	Average Voltage (V vs. Li/Li)
Cathodes			
Layered	$LiCoO_2$	272 (140)	4.2
	$LiNi_{1/3}Mn_{1/3}Co_{1/3}O_2$	272(160)	4.0
Spinel	$LiMn_2O_4$	148(120)	4.1
	$LiMn_{3/2}Ni_{1/2}O_4$	148(120)	4.7
Olivine	$LiFePO_4$	170(160)	3.45
	$LiFe_{1/2}Mn_{1/2}PO_4$	170(160)	3.4/4.1
Anode			
Carbon	Graphite	372	<0.1
	Hard Carbon	700	0.2
Alloy	Silicon	4200 (900)	0.4
	Tin	994	0.6
Metal Oxide	$Li_4Ti_5O_{12}$	175	1.6

$$Li^+ + e^- + LiO_2^* \leftrightarrow Li_2O_2^*(Cathode) \tag{1.11}$$

$$LiO_2^* + LiO_2^* \leftrightarrow Li_2O_2^* + O_2(Cathode) \tag{1.12}$$

The molecules with an * correspond to surface absorbed species. The forward reactions correspond to the process of discharge, and the backward arrows correspond to the charging mechanism. As can be appreciated from the equations and Fig. 1.3, the overall reaction takes lithium metal and oxygen to produce lithium peroxide. However, because these reactions require a surface to catalyze the process and provide a surface for Li_2O_2 to deposit, porous cathodes such as carbon are needed for the reaction to proceed. This results in one of the main problems of the Li-O_2 system, which is that given that Li_2O_2 is insulating, the battery self passivates limiting a significant portion of the theoretical energy density of the chemistry [32]. Further problems associated with this requirement are that multiple non reversible side reactions are possible due to the formation of highly active intermediate species that can decompose the supporting cathode and/or electrolyte components [35]. These side reactions are one of the main contributors to cell inefficiencies that reduce cyclability and pose one the largest obstacles for future development of this battery chemistry. In order to develop new electrolytes and supporting cathode materials a deeper understanding of these side reactions

Table 1.2: Select Electrodes for Sodium-ion Batteries [26, 20]

Framework	Compound	Specific Capacity mAh/g (Practical Capacity)	Average Voltage (V vs. Na/Na)
Cathodes			
Layered	$NaCoO_2$	(140)	3.5
	$NaFe_{1/2}Mn_{1/2}O_2$	(190)	3.7
	$NaFe_{1/2}Co_{1/2}O_2$	(160)	3.7
Polyanions & Pyrophosphates	$Na_3V_2(PO_4)_3$	(100)	3.2
	$NaFePO_4$	(120)	2.7
Organic	$Na_6C_8H_2O_6$	(200)	1.8
Prussian Blue	$NaMnFe(CN)_6$	(160)	2.8
Anodes			
Carbon	Hard Carbon	(300)	0.1
Alloys	Sn	847	0.2
Oxides	$Na_2Ti_3O_7$	200	0.3

is needed. Chapter 8 of this thesis explores different failure mechanisms of Li-O_2 batteries that employ one of the most stable electrolyte compositions currently used, lithium triflimide (LiTFSI) in 1,2-dimethoxyethane (DME).

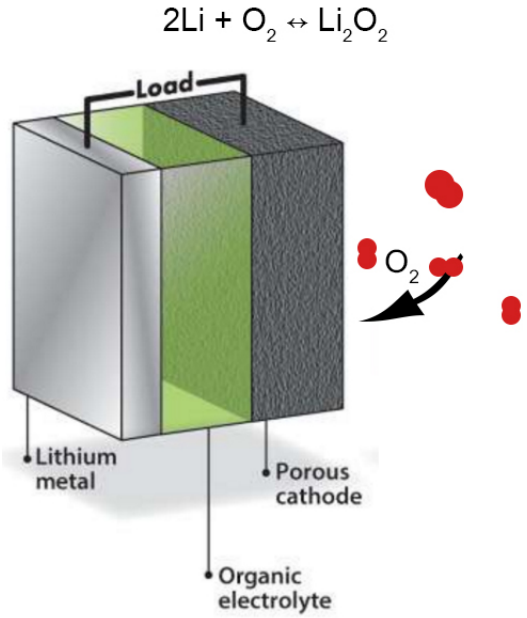

Chapter 2

Basic Theory and Methodology

2.1 Density Functional Theory

The main simulation tool employed in this dissertation was density functional theory (DFT), which is a first principles technique that allows for atomistic insight and understanding of the multiple processes and reactions experimentally tested herein. This theory is based on the seminal papers from P. Hohenberg, W. Kohn, and L. Sham [6, 7]. In their work they implement a series of formulation and approximations that permit numerical solutions of multi-body quantum mechanic problems. The description is particularly suitable to crystalline solids where an ensemble of N nuclei at positions $(R_1, R_2, \ldots, R_{N-1}, R_N)$ and n_e electrons located at $(r_1, r_2, \ldots, r_{n-1}, r_{n_e})$ is periodically repeated. The energy of such an ensemble is described by the Schrödinger equation in Eq. 2.1, in which H is the Hamiltonian, Ψ the wave function and E the total energy of the system [36].

$$H\Psi = E\Psi \tag{2.1}$$

The Hamiltonian operator is further described in equation 2.2, which separates the kinetic and potential energy contributions, encompassing the kinetic energy of electrons and nuclei as well as the electrostatic interactions between all of them.

$$H = \underbrace{\overbrace{-\frac{\hbar^2}{2m_e}\sum_i \nabla_i^2}^{T_e} \overbrace{-\frac{\hbar^2}{2M_\alpha}\sum_\alpha \nabla_\alpha^2}^{T_n}}_{T} + \underbrace{\overbrace{\frac{1}{2}\sum_{i\neq j}\frac{e^2}{|r_i - r_j|}}^{V_{ee}} \overbrace{-\sum_{\alpha,i}\frac{e^2 Z_\alpha}{|r_i - R_\alpha|}}^{V_{en}} + \overbrace{\frac{1}{2}\sum_{\alpha\neq\beta}\frac{e^2 Z_\alpha Z_\beta}{|R_\alpha - R_\beta|}}^{V_{nn}}}_{V} \tag{2.2}$$

For the above equation the first two terms correspond to total kinetic contribution (T), and it is the sum of electrons (T_e) and nuclei (T_n) parts. The remaining three components make up the potential energy (V) description, with V_{ee}, V_{en}, and V_{nn} describing electron-electron, electron-nuclei, and nuclei-nuclei interactions, respectively. Additionally, m_e denotes electron mass, M_α denotes nucleus mass and e and $Z_\alpha e$ represent electron charge and nuclear

charge, respectively, and Z_α is the atomic number for nucleus α.

Given the complexity of employing the above Hamiltonian, one of the common approximations used to simplify the system is to ignore the potential contribution from nuclei-nuclei interactions, also known as the Born-Oppenheimer approximation [37]. Because the nuclei have masses on the order of 1000X that of the electrons, it is reasonable to assume that the nuclei will dominate this interaction with electrons adapting to nuclei movements. This results in a simpler Hamiltonian for the electrons:

$$H = T_e + V_{ee} + V_{en} \tag{2.3}$$

However, given the multi-body nature of the electron-electron interactions, further approximations were needed to make this a tractable problem. The first of the Hohenberg-Kohn theorems states that for a system consisting of n interacting electrons and an external potential $V_{ext}(\vec{r})$, the total energy is a unique functional ($F\left[n(\vec{r})\right]$) of the electron density $n(\vec{r})$, and is given by [6]:

$$E\left[n(\vec{r})\right] = F\left[n(\vec{r})\right] + \int n(\vec{r}) V_{ext}(\vec{r}) \tag{2.4}$$

Because the exact functional is not actually known, the second theorem from Hohenberg and Kohn postulated that for a given $V_{ext}(\vec{r})$, the ground state electron density $n_0(\vec{r})$ and ground state energy E_0 correspond to the minimum value of the functional E [6]:

$$E_0 = E\left[n_0(\vec{r})\right] = min\left\{E\left[n(\vec{r})\right]\right\} \tag{2.5}$$

Part of the importance of the two theorems from Hohenberg and Kohn is that it permits the Schrödinger equation to be solved in terms of a single spatially varying function, instead of a wave function. This allowed Kohn and Sham to replace the full many-body problem with an approximation of non-interacting electrons in an effective external potential V_{eff} [38]. By further splitting the functional from equation 2.4 into three parts, the energy of the electronic system could be described by:

$$E\left[n(\vec{r})\right] = T_s\left[n(\vec{r})\right] + E_H\left[n(\vec{r})\right] + E_{xc}\left[n(\vec{r})\right] + \int n(\vec{r}) V_{ext}(\vec{r}) \tag{2.6}$$

where $T_s\left[n(\vec{r})\right]$ denotes the kinetic energy of the non-interacting electrons, $E_H\left[n(\vec{r})\right]$ represents the Hatree approximation to the Coulomb energy characterizing the interaction of the electrons, and $E_{xc}\left[n(\vec{r})\right]$ is the exchange-correlation energy. Each one of these terms is dependent on the electron density which can be calculated from the Kohn-Sham orbitals according to:

$$n(\vec{r}) = -e \sum_{i=1}^{n_e} \left|\phi_i(\vec{r})\right|^2 \tag{2.7}$$

The electron density is required to calculate the Coulomb-energy term, $E_H\left[n(\vec{r})\right]$, which is given by:

$$E_H\left[n(\vec{r})\right] = \frac{1}{2}\int \frac{n(\vec{r})n(\vec{r'})}{\left|\vec{r}-\vec{r'}\right|} \tag{2.8}$$

The implementation of the functional term is still dependent on some approximate description of the exchange-correlation energy, $E_{xc}\left[n(\vec{r})\right]$. Whereas $T_s\left[n(\vec{r})\right]$ and $E_H\left[n(\vec{r})\right]$ are physically accurate terms (taking into account the Born-Oppenheimer approximation), there is no exact $E_{xc}\left[n(\vec{r})\right]$, resulting in the principle source of error to DFT calculations. The different approximations to this term are what give rise to several of the potentials commonly used in DFT simulations. Among the most widely used exchange correlation functionals are the local density approximation (LDA) [39, 40] and the generalized gradient approximation (GGA) [41, 42, 43]. For the prior approximation the functional depends only on the density at the coordinate where the functional is evaluated, and is calculated by:

$$E_{xc}^{LDA}\left[n(\vec{r})\right] = \int n(\vec{r})\epsilon_{xc}\left[n(\vec{r})\right] d\vec{r} \tag{2.9}$$

where ϵ_{xc} is the exchange-correlation energy per particle of a homogeneous electron gas

For the GGA functional in addition to considering the local density, the gradient of the electron density is also taken into account as a means of measuring the rate of variation of the charge density, according to:

$$E_{xc}^{GGA}\left[n(\vec{r})\right] = \int n(\vec{r})\epsilon_{xc}\left[n(\vec{r})\right] F_{XC}\left[n(\vec{r}), \nabla n(\vec{r})\right] d\vec{r} \tag{2.10}$$

where $F_{XC}\left[n(\vec{r}), \nabla n(\vec{r})\right]$ serves as a correction factor to the LDA exchange-correlation energy potential. Additional corrections are need in specific scenarios to correct shortcomings of the functional. For oxide and other insulator systems that contain transition metals with $d-$ and $f-$ electrons, these orbitals are highly localized which result in electron self-interaction errors. This arises as a consequence of employing functionals where the sum of electron-electron interaction is actually captured by the integral seen in equation 2.8. Because for any system where there is at least one electron, $E_H\left[n(\vec{r})\right]$ is a non-zero term, it depends on the on $E_{xc}^{LDA}\left[n(\vec{r})\right]$ to cancel out any error. However since there still does not exist an exact exchange correlation functionals, this error can become significant for systems like the ones previously described. Among the most commonly used methods to correct this type of error is the Hubbard-U correction. Although there are different formalisms available, in this work the Dudarev et al. method is employed [44], where a system and element dependent correction is added to the exchange correlation functional according to:

$$E\left[n(\vec{r})\right] = E\left[n(\vec{r})\right] + \frac{U-J}{2}\sum_{\sigma}(n_{m,\sigma} - n_{m,\sigma}^2) \tag{2.11}$$

where U and J are screened Coulomb and exchange parameters, respectively, with the difference of the two terms known as an effective Hubbard-U (U_{eff}). $n_{m,\sigma}$ are the electron occupations for orbital m and spin σ, such that the total number of electrons, $N_\sigma = \sum_\sigma n_{m,\sigma}$. The implication of equation 2.11 is that an energy penalty is placed on partial occupancy

of orbitals, such that orbitals are either fully occupied or empty. This minimizes the error associated with the self-interaction effect.

Hartree-Fock Method

An alternative method for solving the time-independent Schrödinger equation is the Hartree-Fock method, which is another iterative method that assumes that traditionally was accounted for in formalisms in which the electron wavefunctions are expanded in a linear combination of atomic orbitals. Because this method seeks to provides a formally "exact" description of the exchange contribution to the electronic energy it is considerably more expensive, and was traditionally applied in calculations for molecules. In the approach, the exchange interactions are described through the Fock operator [45]:

$$\widehat{F}[\phi_j](1) = \widehat{H}^{core}(1) + \sum_{j=1}^{N/2}[2\widehat{J}_j(1) - \widehat{K}_j(1)] \tag{2.12}$$

where $\widehat{F}[\phi_j](1)$ is the one electron Fock operator generated by orbitals ϕ_j, $\widehat{H}^{core}(1)$ is the one electron core Hamiltonian, $\widehat{J}_j(1)$ is the Coulomb operator for electron-electron interaction in the j^{th} orbital, and $\widehat{K}_j(1)$ is the exchange operator. The one-electron wave function is treated as an eigenvalue problem according to:

$$\widehat{F}(1)\phi_i(1) = \epsilon_i\phi_i(1) \tag{2.13}$$

where $\phi_i(1)$ are a set of one-electron wave functions, called the Hartree-Fock molecular orbitals. In the applications of this approach in the current work the orbitals are described as linear combinations of atomic orbitals by either Slate-type orbitals or more commonly Gaussian-type orbitals, with the overall linear combination of the functions forming basis sets [46, 47, 48]. In this work the 6-311+G(2d,p) basis set [48, 47, 49] was employed with the dispersion-corrected B3LYP-D3 density functional method [50, 51, 52].

Numerical Approach to DFT Calculations

It is worth noting that both the Kohn-Sham and Hartree-Fock methods require a numerical iterative process that must be converged to set criterion in order to determine any structure or properties.

For the Kohn-Sham approach the ultimate calculations also reduce to an eigenvalue problem similar to Eq. 2.13, which is:

$$\left[-\frac{1}{2}\nabla^2 + V_{eff}(\vec{r})\right]\phi_i(\vec{r}) = \epsilon_i\phi_i(\vec{r}) \tag{2.14}$$

From this equation we need to calculate $V_{eff}(\vec{r})$, but in order to do so requires the electron density ($n(\vec{r})$, which is a function of the Kohn-Sham orbitals ($\phi_i(\vec{r})$). Solving this eigenvalue problem is performed by various software packages that implement the iterative approach

using basis sets such as plane waves to represent the wave functions. These wave functions are representation of the electrons in a given system, where, according to the accuracy required, the electrons (i.e. the wavefunctions) can be divided into valence or core, $\psi_i^v(\vec{r})$ and $\psi_i^c(\vec{r})$, respectively. Because most of the systems modeled in this dissertation were in the solid state, it is valid to employ pseudopotentials that only consider the valence electrons engaged in bonding. This allows for a simpler eigenvalue problem to be solved according to:

$$\left[-\frac{1}{2}\nabla^2 + V_{ext}^{ps}\right]\tilde{\psi}_i^v(\vec{r}) = \epsilon_i\tilde{\psi}_i^v(\vec{r}) \tag{2.15}$$

The $\tilde{\psi}_i^v$ must be solutions to the Kohn-Sham equation, but they may themselves describe an electron density different from that used in the Kohn-Sham potentials. Subsequently, from this output density the eigenfunction is solved, yielding a new electron density that can be iterated until a converge criteria is reached, resulting in a self-consistent result.

The approach in the Hartree-Fock method is effectively the same, as it also requires an iterative solution to a self-consistent solution.

2.2 Nudged Elastic Band Method

The nudged elastic band (NEB) method is one of the best established approaches to determining the minimum energy path (MEP) for a system to transition from one known state to another [53]. This method is commonly used to calculate energy barriers for certain chemical events such as chemical reactions, diffusion in solids, or conformation changes in molecules. This approach depends on knowing the energy and forces associated with a system in the two end points of a transition (initial and final configuration). To build up the MEP a set of images or states that connect the two end configurations is established, which when relaxed give a saddle point corresponding to an energy of activation [54]. The images can be connected by springs with zero natural length, with the object function:

$$S^{PEB}(\vec{R}_1, ..., \vec{R}_{P-1}) = \sum_{i=0}^{P} V(\vec{R}_i) + \sum_{i=1}^{P} \frac{Pk}{2}(\vec{R}_i - \vec{R}_{i-1})^2 \tag{2.16}$$

where k is the spring constant, $\vec{R}_i - \vec{R}_{i-1}$ is the length between two images, and $V(\vec{R}_i)$ is a potential energy term associated with each image. The above equation is used in a simpler method called the plain elastic band (PEB) method, which when minimized with regard to the energy of each image can be used to obtain MEPs [55, 53]. One drawback of this method is that the energy path calculated will drift from the MEP to reduce the forces between images when there are strong non-parallel forces. The mathematical description of the forces at each image are:

$$\vec{F}_i = -\vec{\nabla}V(\vec{R}_i) + \vec{F}_i^s \tag{2.17}$$

where

$$\vec{F}_i^s \equiv k_{i+1}(\vec{R}_{i+1} - \vec{R}_i) - k_i(\vec{R}_i - \vec{R}_{i-1}) \tag{2.18}$$

Because the stiffness of the spring between each image can not be infinite, any non-parallel forces will act to shift an image off the MEP, with this approach only working when the apex is somewhat symmetric, with other scenarios resulting in corner cutting.

A solution to this problem is to increase the number of images, however, this approach could require a computationally prohibitive number of in-between states. An alternative approach that overcomes this problem is by splitting the forces on each image between parallel and perpendicular to more efficiently described the MEP with a lower number of images. By describing the force on an image by:

$$\vec{F}_i^0 = -\vec{\nabla}V(\vec{R}_i)|_\perp + \vec{F}_i^s \cdot \hat{\tau}_{||}\hat{\tau}_{||} \tag{2.19}$$

where $\hat{\tau}_{||}$ is the unit tangent to the path. This approach traces the forces onto the MEP, but still can result in kinks that make convergence to the path difficult [56]. To overcome this effect an additional switching function is introduced, making the force on an image i:

$$\vec{F}_i^{NEB} = \vec{F}_i^0 + f(\phi_i) + (\vec{F}_i^s - \vec{F}_i^s \cdot \hat{\tau}_{||}\hat{\tau}_{||}) \tag{2.20}$$

where the switching function is:

$$f(\phi_i) = \frac{1}{2}(1 + \cos(\pi(\cos\phi))) \tag{2.21}$$

and

$$\cos\phi_i = \frac{(\vec{R}_{i+1} - \vec{R}_i) \cdot (\vec{R}_i - \vec{R}_{i-1})}{(|\vec{R}_{i+1} - \vec{R}_i||\vec{R}_i - \vec{R}_{i-1}|)} \tag{2.22}$$

By shifting any perpendicular force when the angle between images is zero it is possible to avoid cutting corners as long as enough images are included. Furthermore, since some part of the perpendicular force will be included at any angle between 90^o and 0^o the kinks will be smoothed out accelerating convergence [57, 55, 53].

Chapter 3

Ab Initio Calculation of the Proton Transfer Mechanisms in $DyPO_4$

3.1 Foreword

The work presented in this chapter was published by I. M. Markus, N. Adelstein, M. Asta, L. C. De Jonghe, in the Journal of Physical Chemistry C, vol. 118, issue 10, pages 5073-5080 (2014), and is reproduced here with the permission of co-authors and publishers (American Chemical Society).

3.2 Abstract

Proton mobilities in xenotime-structured $DyPO_4$ have been investigated through first-principles calculations of hopping rates. The calculated mobility is highly anisotropic, consistent with the tetragonal symmetry of the xenotime crystal structure. Due to the presence of one-dimensional channels along the c axis in the xenotime structure, the hopping rate is significant along this direction. The activation energy for hopping along the a and b axes is computed to be 0.45 eV away from aliovalent dopant impurities, while the calculated energy barrier within the channels that run along the c axis is 0.15 eV. The corresponding hopping rates along the c-axis channels are more than two orders of magnitude larger than those calculated previously for the monoclinic monazite-structured $LaPO_4$ compound. The effects of aliovalent dopants on proton migration were investigated, considering the case of Ca^{2+} substitution for Dy^{3+}. These calculations reveal a dopant-proton binding energy of approximately 0.4 eV, and an increase in the hopping barriers near the dopant by up to 0.2 eV. These dopant effects were found to be relatively localized, with minimal changes to the energetics of the protons obtained more than approximately 5 Å away from the aliovalent impurity.

3.3 Introduction

The development of electrochemical devices such as fuel cells and membrane separators has focused attention on the need for electrolyte materials capable of operating between 300° and 600°C. In this intermediate temperature range, expensive noble-metal catalysts can be avoided, and material incompatibilities and degradation processes often associated with higher temperatures are significantly reduced [58]. New solid electrolytes for applications at intermediate temperatures have been mainly focused on solid proton conductors, since the diffusion of protons typically has a smaller activation energy compared to other multivalent ions[59, 60] , such as O^{-2}.

The most widely studied ceramic proton conductors are doped perovskite-structured oxides such as $BaCeO_3$ and $BaZrO_3$ [61, 62, 63, 64, 15] . Work on these compounds has highlighted several factors affecting proton mobilities and incorporation, such as bond lengths, crystal symmetry, binding to cation dopants, and the effects of micro-structural features such as grain boundaries and nanophase inclusions [65, 66, 67] . Several of these factors arise due to the nature of the bonding of protons in oxides, which typically involves the formation of a short hydroxyl bond with an oxygen ion, and a longer hydrogen bond with another neighboring oxygen ion. As reviewed in Ref. 5 (see also references therein) the optimal stability and conduction of protons in oxides is achieved when the oxygen-oxygen separation is in the range of 2.5-3.0 Å. This spacing enables the protons to form stable hydrogen and hydroxide bonds while also allowing fast hopping rates to neighboring binding sites. The energetics underlying proton hopping have been shown to be highly sensitive to changes in the local structural and chemical environments. For example, as the size of the A-site cation increases in a perovskite compound (ABO_3), the neighboring BO_6 octahedra become distorted, leading to a reduction in symmetry [68] . Such structural distortions can change the proton-oxygen bond angles and bond lengths which consequently affect ionic conductivity. Furthermore, the addition of dopants, precipitates or inclusions changes the local crystal symmetry and electrostatic potential, leading to possible proton traps.

Alternative compounds that are also considered promising candidates for fuel cell and sensor applications include ortho-niobates, ortho-tantalates and ortho-phosphates [69, 64]. It has been demonstrated that these materials can exhibit proton conductivities in the range of $10^{-4} - 10^{-3} S * cm^{-1}$ below 800^oC. One class of these materials that has not been fully investigated for proton-conducting electrolyte applications includes the rare-earth phosphates (REPs). To date, most experimental and computational work on REPs has focused on compounds with the monoclinic monazite structure, in particular $LaPO_4$ and $CePO_4$ aliovalently doped with divalent cations [70, 71] . While these materials exhibit high protonic conduction with negligible oxygen-ion transport [59, 72] , in the temperature range of interest they feature lower conductivities than traditional oxygen ion conductors [65].

In the present work we examine proton conduction in an alternative REP, $DyPO_4$, employing computational methods based on density-functional theory (DFT) [73]. The work is motivated by the insights gained from the previous studies of perovskite proton conductors summarized above, which suggest that the replacement of La^{3+} or Ce^{3+} cations by Dy^{3+}

should increase proton mobility. Specifically, the Dy^{3+} cation has a smaller ionic radius of 1.083 Å compared to either La^{3+} or Ce^{3+}, 1.216 Å and 1.196 Å respectively [74] . The smaller cation size correlates with the formation of a higher symmetry structure, *i.e.* the xenotime structure shown in Fig. 3.1. Here, the oxygen atoms occupy a single unique symmetry site and are separated by approximately 2.56 Å[75] , which falls in the optimal range of neighboring oxygen distance identified in the studies of proton-conducting oxides mentioned above. By comparing the current calculated results with previous computational and experimental studies of $LaPO_4$ and $CePO_4$ [76, 70, 77] , we aim to derive insights, similar to those developed for the perovskite-structured oxides, to guide the selection and engineering of REP compounds and other related tetrahedral moiety structures for proton-conductor applications.

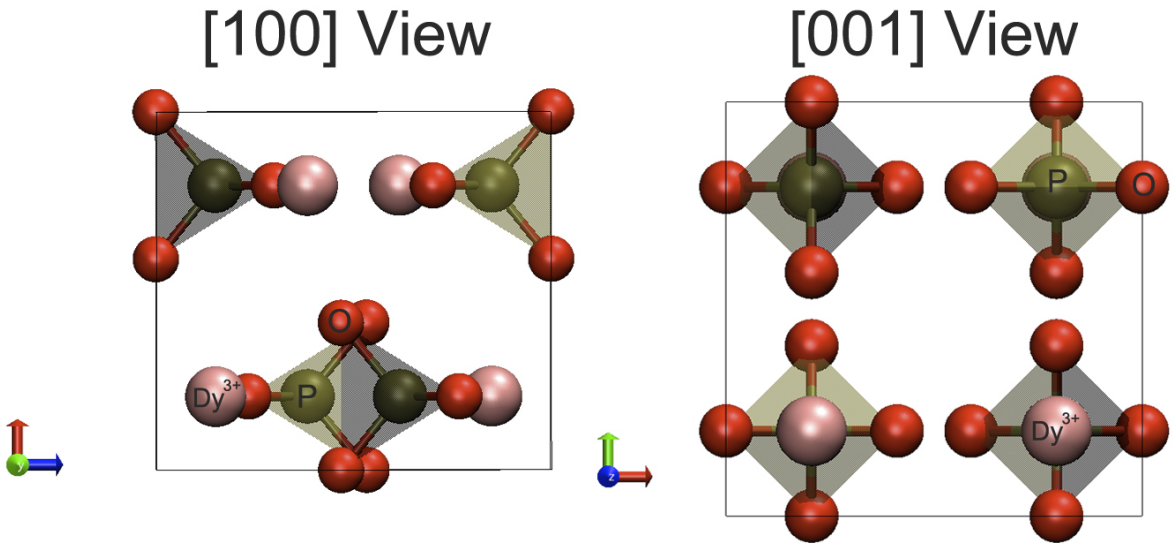

Figure 3.1: $DyPO_4$ has a tetragonal unit cell with a xenotime structure with $I4_1/amd$ space group. The conventional tetragonal unit cell contains 4 dysprosium atoms (pink balls) and 4 tetrahedral phosphate PO_4 anions (green balls denotes phosphorous, surrounded by a tetrahedron of red oxygens).

3.4 Computational Methods

To investigate proton mobility in $DyPO_4$ we begin by computing the potential energy landscape for protons using DFT . Subsequently the energy barriers for proton hopping are calculated using the climbing image nudge elastic method (CI-NEB) [78, 79, 80, 81] . The attempt frequency for each symmetry distinct migration path is then estimated using harmonic transition-state theory [54] based on calculated vibrational frequencies for protons in the minimum energy and saddle point positions. Dopant binding effects on proton mobilities

[82, 83, 71] are investigated through 3% substitution of Ca^{2+} for Dy^{3+}. From the calculated hopping rates the two distinct elements of the diffusivity tensor (D_{11} corresponding to the diffusion along either of the symmetry equivalent a or b directions, and D_{33} corresponding to diffusion along the c axis) were calculated neglecting dopant effects. The results provide limiting values for the proton mobilities far from dopant cations, and enable a comparison with previous related calculations for monazite-structured REPs.

DFT Calculation

The DFT calculations were carried out using Kohn-Sham density functional theory with the projector augmented wave (PAW) method to treat the nuclei and core states [84, 85] , as implemented in the Vienna *ab-initio* simulation package (VASP) code [86, 87] . For the exchange and correlation functional we used the generalized gradient approximation (GGA) of Perdew, Burke, and Ernzerhof (PBE) [88] . For calculations of the $DyPO_4$ crystal structure parameters (lattice constants and ion positions), all computations used the conventional tetragonal unit cell illustrated in Fig. 3.1. The electronic wave functions were expanded in a plane wave basis set with an energy cutoff of 600 eV. The electron states were sampled over the Brillouin zone using the Monkhorst-Pack method [89] with a k-point grid of 8x8x8 for a single unit cell or 4x4x4 k-point grid for 2x2x2 supercell calculations. A 2x2x2 grid of kpoints was used for the phonon frequency calculation due to computational constraints. Calculations were performed to test the convergence of the energy with respect to the number of k-points and plane-wave cutoff, and the energy barriers for proton transport are estimated to be converged to within approximately 0.01 eV. In the structural relaxations, the ionic positions were optimized until the forces on the ions were converged to 10 meV/Å. The PAW potentials used had 5 valence electrons for P ($3s^2 3p^3$), and 6 valence electrons for O ($2s^2 2p^4$). For Dy we used the VASP-PAW potential for which the f electrons in the 3+ ion are treated as core states. For the Ca dopant cation the PAW potential used 10 valence electrons ($3s^2 3p^6 4s^2$).

To investigate the potential energy landscape for protons in $DyPO_4$ we introduced H atoms into a single unit cell (1x1x1, containing four formula units) and reduced the number of electrons (relative to that corresponding to a charge-neutral system) by one for each proton incorporated. This reduction in the number of electrons leads to the formation of a positively charged proton, and a uniform negative background charge is included to maintain the overall charge neutrality of the system. Low energy sites were determined by systematically sampling 30 symmetry-distinct initial positions and performing structure relaxations with respect to ion positions, unit cell shape and volume. As shown in Fig. 3.2, the procedure yielded two symmetry-distinct local energy minima for protons in bulk $DyPO_4$, which were subsequently used as initial conditions for calculations of the energy barriers for proton hopping in larger 2x2x2 supercells, as described in the next sub-section.

Dopant effects were studied through the use of 2x2x2 supercells where one Dy^{3+} cation was replaced by Ca^{2+} , for a dopant concentration of 3 %, which is comparable to the doping levels employed in previous experimental studies of proton conduction in REPs [59, 60, 77]

. Proton binding in these charge-neutral supercells was investigated by placing a H atom at different distances from the dopant cation and allowing the structure to relax.

Proton Hopping Rates

Minimum energy pathways (MEPs) for proton hopping were determined using the climbing-image nudged elastic band (CI-NEB) method [78, 79, 80, 81] with 2x2x2 supercells. Initial and final states were selected from the proton local energy minimum identified using the procedure described above. The activation energy for proton hopping was determined from the energy difference between the initial position and the maximum along the MEPs. Phonon analysis (see below) was subsequently used to verify that the MEP maxima identified by the CI-NEB method corresponded to true saddle point configurations on the potential energy surface (*i.e.*, phonon analysis verified that the positions where characterized by one imaginary phonon frequency with all other frequencies being real).

Within the framework of harmonic transition-state theory [54] the jump frequencies (Γ) for proton transfer between energy minimum positions were computed from the formula:

$$\Gamma = \nu_o e^{-E_B/k_B T} \tag{3.1}$$

where k_B and T denote Boltzmann's constant and temperature respectively. The activation energy for proton hopping is given as $E_B = E_{sadd} - E_{init}$, where E_{sadd} and E_{init} denote the energies corresponding to saddle-point and initial proton positions. For the attempt frequency (ν_0) in Eq. (3.1) we used the high-temperature limit of the expression given by harmonic transition-state theory, corresponding to a ratio of the product of the real phonon frequencies in the initial and saddle-point configurations. We thus neglect anharmonic contributions, as well as the quantum corrections associated with zero-point motion, freezing out of phonon occupancies and tunneling contributions. The importance of quantum-mechanical effects on proton hopping rates has been assessed in previous work [90, 91, 92] for $BaZrO_3$, where it was found that classical harmonic transition state theory gives reasonably accurate hopping rates for temperatures above approximately 600 K. By analogy we will assume that the hopping rates determined by classical harmonic transition state theory provide a reasonably accurate description of proton mobilities over the temperature range of 600 to 1400 K considered in the present work. Further, the use of classical harmonic transition-state theory allows us to make a direct comparison to previous calculations in $LaPO_4$ [70, 76] , which have been based on the same formalism.

For both the stable binding and saddle point configurations the vibrational frequencies entering into the transition-state-theory expressions for the hopping rates were calculated using the central finite-difference force-constant method implemented in VASP. In these calculations we considered a single proton in a 2x2x2 supercell, and computed all Γ point phonon frequencies, derived from the calculated changes in forces resulting from finite atom displacements of 0.015 Å. The calculated phonon frequencies in both the binding and saddle point geometries are available in the the supplemental information. Dopant binding effects

Table 3.1: Calculated and experimentally measured [75, 96] unit-cell structural parameters for $DyPO_4$.

Parameter	Calculated			Experimental		
a, b, c (Å)	6.961	6.961	6.058	6.907[75]	6.907[75]	6.046[75]
				6.917[96]	6.917[96]	6.053[96]
Atomic Position	x	y	z	x	y	z
Dy	0.0	0.75	0.125	0.0	0.75	0.125
P	0.0	0.25	0.375	0.0	0.25	0.375
O	0.0	0.076	0.215	0.0	0.0646[75]	0.1967[75]
				0.0	0.076[96]	0.2162[96]
Distance P-O (Å)	1.554			1.537[75]		
Distance Dy-O (Å)	2.331			2.318[75]		
Intra-Tetrahedral O(1)-O(2) (Å)	2.41			2.431[75]		
Intra-Tetrahedral O(1)-O(3) (Å)	2.58			2.562[75]		

were also investigated by utilizing the different binding geometries found in the bulk calculations to investigate changes in the energy barriers and attempt frequencies at different distances from the dopant ion. Proton mobilities along each crystallographic direction were calculated analytically using the Einstein-Smoluchowski equation [93, 94, 95] , as described in the next section.

3.5 Results

Structural Properties of Bulk $DyPO_4$

In the experimentally observed xenotime crystal structure, the $DyPO_4$ unit cell is constructed from four PO_4 tetrahedra and four Dy atoms. With origin choice 2 for the $I4_1/amd$ space group the Dy atoms are located at the 4a Wyckoff position, the P atoms occupy the 4b Wyckoff position, and the O atoms occupy the 16h Wyckoff position. The oxygen atom positions feature two cell-internal structural degrees of freedom, corresponding to the y and z position of the 16h Wyckoff site. The calculated and experimentally measured parameters for the lattice vectors, atomic positions, and inter-atomic distances are presented in Table 3.1. The calculated lattice parameters slightly overestimate the measured values, but by no more than 1 %. The calculated bond lengths also overestimate the measured values by approximately 1%. Overall the good level of agreement between experiment and measurements for the $DyPO_4$ structural parameters suggests that the chosen functionals, PAW potentials, and numerical settings in the VASP calculations provide an accurate description of the bonding in this compound.

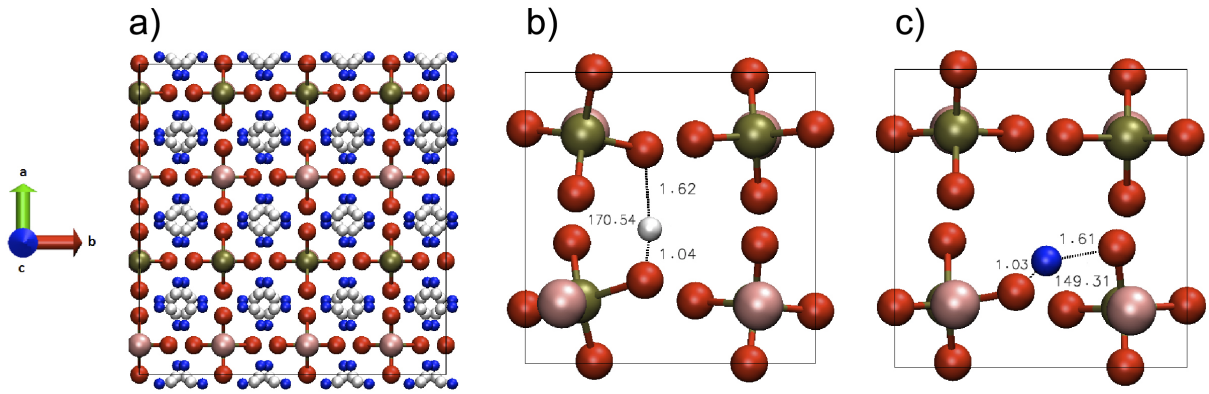

Figure 3.2: Proton Binding Sites: (a) 4x4 unit cell of $DyPO_4$ viewed along the *c* axis, illustrating the calculated global (white atoms) and local (blue atoms) minima energy sites for a proton. (b) A single relaxed unit cell with a proton incorporated at one of the global minima energy sites. The bond lengths for the short hydroxyl and longer hydrogen bonds are 1.04 Å and 1.62 Å, respectively. The angle between these bonds is 170.54 °. (c) A single relaxed unit cell with a proton incorporated at one of the local minima energy sites. The bond lengths for the short hydroxyl and longer hydrogen bonds are 1.03 Å and 1.61 Å, respectively. The angle between these bonds is 149.31 °.

Proton Binding Sites

Sampling of the potential energy surface was performed in a 1x1x1 cell and yielded 32 global minimum energy positions that are related through symmetry to a single unique site, correspond to a 32i Wyckoff position. There are also 32 symmetry-related positions corresponding to local minima in the potential energy landscape, with 0.2 eV higher energy compared to the global minimum in the potential-energy landscape. Figure 3.2a shows 4 unit cells viewed along the *c* axis; the global and local minimum energy sites for protons are shown in white and blue, respectively. The low energy sites lie along channels as far removed from the Dy and P ions as possible.

Figures 3.2(b) and (c) show the relaxed bonding geometry of the proton in the global and local minimum energy positions. In both positions the proton bonds with two oxygen atoms from different phosphate tetrahedra, with a hydroxyl bond length of 1.03 or 1.04 Å and a longer hydrogen bond of 1.61 or 1.62 Å. The formation of these bonds gives rise to a distortion of the two neighboring tetrahedra, with the two oxygen ions moving towards the proton. The bond angles between the hydrogen and hydroxyl bond in the global and local energy minimum positions are 171° and 149°, respectively.

The higher symmetry crystal structure of $DyPO_4$ leads to a simpler energy landscape for proton binding compared to other orthophosphates like $LaPO_4$ or oxides with tetrahedral moieties like $LaBaGaO_4$ [64] . Similar to these other proton-conducting compounds the stable binding sites feature hydrogen and hydroxyl bonds between oxygen ions of two adjacent

Table 3.2: Proton Jump Types in $DyPO_4$

Jump Type	Jump Distance (Å)	Energy of Activation (eV)	Attempt Frequency (THz)
Oscillatory	0.45	0.075	3.61
Inter-Tetrahedral	1.65	0.15	5.24
Intra-Tetrahedral (1)	2.65	0.45	19.6
Intra-Tetrahedral (2)	1.60	1.22	-

tetrahedra. However, for $LaPO_4$ or $LaBaGaO_4$ each oxygen in the tetrahedron has a unique Wyckoff position which results in wide array of distinct binding sites, with energy differences varying by up to 0.70 eV [76] .

Proton Hopping Barriers

The minimum energy paths (MEPs) connecting the energy-minimum positions identified in the previous section were computed using the CI-NEB method. Table 3.2 lists the main proton transition types identified in these calculations, along with the respective jump length, energy barrier, and attempt frequency, as derived by DFT calculations using 2x2x2 supercells. The MEPs for each proton jump type are illustrated in Figure 3.3 a-d. The images show for each path the initial position (panel 1), the saddle-point position (panel 2) and the final position (panel 3).

Conduction along the channels parallel to the c direction requires only the oscillatory and inter-tetrahedral proton jump, with a maximum energy barrier of 0.15 eV. This low energy barrier results from the concentration of energy minimum sites along the channels in this crystallographic direction. For conduction along the a and b directions the minimum energy path requires oscillatory, inter-tetrahedral and intra-tetrahedral (of type (2) in Fig. 3.3) proton jumps, with a maximum energy barrier of 0.45 eV. This higher energy barrier results from the proton having to pass through areas of high Coulombic repulsion between adjacent tetrahedra due to the nearby positively charged P ions. The MEP results indicate that $DyPO_4$ should exhibit anisotropic conduction, with fast channels forming along the c axis and slower conduction in the b and a axis.

Dopant Binding Effects

Dopant impurities are used experimentally to introduce proton charge carriers into REP and perovskite compounds [61, 62, 63, 64, 15, 59, 60] . It has been shown in recent computational studies [97, 98] that protons can bind strongly to such dopants, leading to a reduction in proton conductivity. Dopant effects in $DyPO_4$ are investigated here considering the case of Ca^{2+} substitution for Dy^{3+}, with a total dopant concentration of approximately 3 %, as described in section II, which matches with experimental values. The valence difference between the Ca and Dy cations creates a charged defect that allows a proton to be introduced

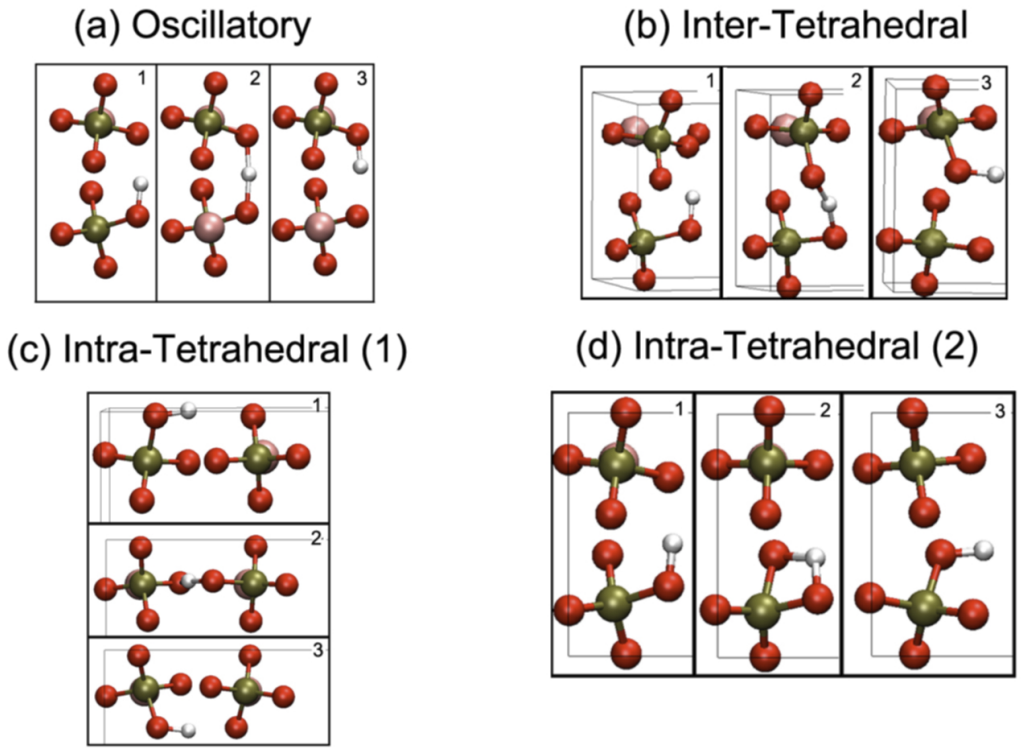

Figure 3.3: The minimum energy paths for each jump type in Table 3.2 a) MEP for an oscillatory proton jump. b) MEP for an inter-tetrahedral proton jump. c) MEP for the low energy barrier intra-tetrahedral proton jump. d) MEP for the high energy barrier intra-tetrahedral proton jump.

into the structure without the need for a charge-compensating background charge in the supercell calculations.

The calculated energies for protons in their stable bonding configuration are plotted as a function of distance from the Ca dopant in Fig. 3.4. In this plot all energies are referenced to the value corresponding to the proton position furthest from the dopant. The plot shows an increasingly negative energy as the proton is moved closer to the dopant, with a maximum attractive proton-dopant energy of approximately 0.4 eV. This value is slightly larger than the binding energies of 0.20 eV and 0.31 eV reported for protons in the Ba-$LaPO_4$ [98] and Sr-$LaPO_4$ [76, 97] systems, respectively, suggesting that the choice of other dopants for the $DyPO_4$ system may lead to smaller binding effects.

We consider next the effect of the dopant on the activation energy for proton hopping. Table 3.3 lists the calculated energy barriers and jump attempt frequencies for hopping at different distances from the dopant. It is found that the activation energies and attempt frequencies for inter-tetrahedral jumps are changed by approximately 0.03 eV and 1.5 THz respectively, as the proton is moved away from the dopant; the values listed in Table 3.3 are

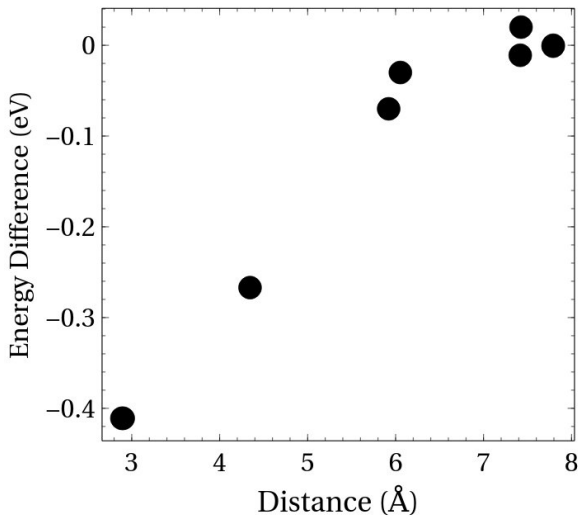

Figure 3.4: Protons will be locally stabilized and bound the more proximal they are to a Ca dopant cation, with an energy difference from bulk of up to 0.4eV

Table 3.3: Dopant Effect on Proton Mobility in $DyPO_4$

Jump Type	Distance from Dopant (Å)	Energy of Activation (eV)	Attempt Frequency (THz)
Inter-Tetrahedral	3-4.5	0.15	2.14
Inter-Tetrahedral	7.5	0.12	3.64
Intra-Tetrahedral (1)	3-4.5	0.20	15.5
Intra-Tetrahedral (1)	7.5	0.42	29.6

close to those obtained for the charged supercells (with compensating background charge) in the absence of an explicit dopant. For the intra-tetrahedral jump the activation energy and attempt frequency for hops nearest to the dopant are both lower by approximately a factor of two, relative to the sites farthest from the dopant. The activation energy for the inter-tetrahedral jump furthest from the dopant is within 0.03 eV of the value obtained from the charged-supercell calculations, while the attempt frequency is higher by roughly 30 %. Overall, the results demonstrate fairly significant effects of the dopant on the inter-tetrahedral hopping rates, but with a reasonably localized spatial extent, i.e., the effects are strongest within approximately 5 Å of the dopant.

Proton Diffusion Coefficients in $DyPO_4$

In this section we use the proton hopping rates presented in section 3.3 to compute the two components of the proton diffusivity tensor (D_{11} for diffusion along the a or b axes, and D_{33} for diffusion along the c axis). In these calculations we use the values of the proton hopping rates from Table 3.2, computed in the bulk structure. While the results in section 3.4 demonstrate

that the presence of dopants in a real sample will clearly affect the proton diffusivities, we focus in this section on results for the "intrinsic diffusivity" computed without accounting for such dopant effects. These results are of interest for two main reasons. First, they are viewed to represent an upper bound that provides a value for the mobility (μ) for the protons (through the Einstein relation $\mu = qD/kT$) in regions of the crystal far from dopants; this upper bound could in principle be realized in channels that are not blocked by dopants in thin-film samples, or though selection of proper divalent cations to minimize the effects of dopant binding. Second, such intrinsic diffusivities have been computed previously for $LaPO_4$ [70, 76] and a comparison of these values with the present results provides a framework for analyzing the effect of crystal structure on proton mobilities in REP compounds.

To estimate the intrinsic proton diffusivities in $DyPO_4$ we make use of the Einstein-Smoluchowski formula [93, 94, 95] :

$$D = \frac{\bar{x}^2}{2 * t} \tag{3.2}$$

where $\bar{x}$ is the mean jump length, and t is the residence time, which can be equated to Γ^{-1}. In the application of this formula, we assume that along each crystallographic direction proton diffusion will be rate limited by the smallest energy barrier available for continuous transport. For diffusion along the c axis, this is the inter-tetrahedral hop with energy barrier of 0.15 eV, while along the a and b axes, it is the intra-tetrahedral jump with energy barrier 0.45 eV. To check the accuracy of these assumptions we employed kinetic-Monte-Carlo (KMC) simulations employing all of the hops with activation energies less than 1 eV. The values of D_{11} and D_{33} obtained with Eq. (3.2) agree quantitatively with the KMC simulations, with a maximum discrepancy of 35 % which indicates that diffusion along each direction is rate limited by the smallest energy barrier available. The resulting estimates of the diffusion coefficients are as follows:

$$\mathrm{D_{11} = D_{22} = 6.88 \times 10^{-3} \exp\left[-0.45eV/k_BT\right]\ cm^2s^{-1}} \tag{3.3}$$

$$\mathrm{D_{33} = 7.6 \times 10^{-4} \exp\left[-0.15eV/k_BT\right]\ cm^2s^{-1}} \tag{3.4}$$

At a temperature of 600 K, which represents the lower bound of operating temperatures for intermediate-temperature SOFC applications, the corresponding values are $D_{11} = 1.13^{-6}$ cm^2 s^{-1}, and $D_{33}= 7.42^{-5}$ cm^2 s^{-1}. These values demonstrate the highly anisotropic nature of the intrinsic proton mobilities in the xenotime structure: along the channels parallel to the c axis the intrinsic mobility is a factor of 65 larger than along the directions perpendicular at a temperature of 600 K. The pronounced anisotropy in the intrinsic diffusivities are further illustrated in Fig. 3.5 which provides an Arrhenius plot of the diffusivities given by Eqs. (3.3) and (3.4).

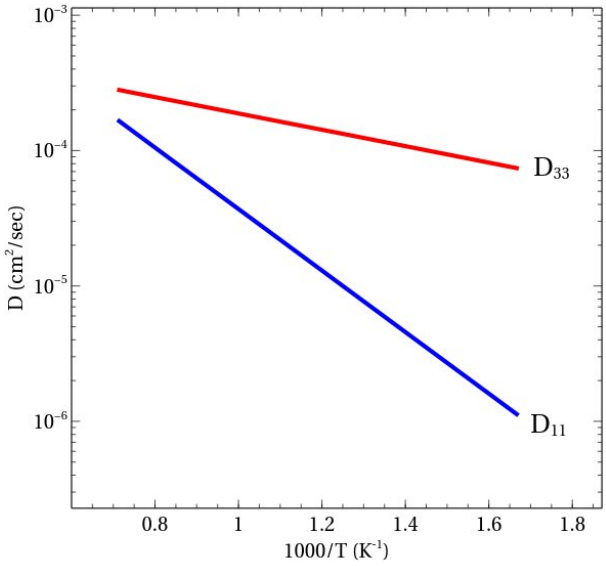

Figure 3.5: Calculated diffusion coefficient for each crystallographic direction in the temperature range of 600-1400 K. The blue and red line correspond to the D_{11} direction and D_{33} direction respectevely.

3.6 Discussion

$DyPO_4$ exhibits anisotropy in its diffusion tensor consistent with the tetragonal symmetry of the xenotime crystal structure. The close spacing of low energy sites in the channels parallel to the [001] crystallographic direction facilitates fast proton conduction along this direction. By contrast, conduction along the *a* or *b* directions involves higher-energy jumps that bring the proton near the positively charged P ion, leading to much slower mobilities in these directions. The present results for $DyPO_4$ are in contrast to those obtained previously for $LaPO_4$ [70, 76] , for which the the monoclinic monazite structure features more distinct energy minima for proton binding and several different competing diffusion paths. At 800 K the intrinsic diffusivity obtained along the *c*-axis channels obtained here is 7.42^{-5} cm^2 s^{-1}, which is more than two orders of magnitude higher than corresponding values calculated previously for $LaPO_4$ at the same temperature [76] . It should be noted that GGA used in this work is known to underestimate the magnitudes of proton-hopping energy barriers since proton-oxygen binding energies are underestimated [99]; however, the comparison between calculated results for $DyPO_4$ and $LaPO_4$, both obtained with the GGA, is expected to be unaffected by such systematic errors.

Using a similar computational methodology to that employed in the current work, Toyoura *et al.* [76] recently calculated energy barriers for proton hopping between different symmetry-inequivalent sites, separated by distinct jump distances, in $LaPO_4$. Comparing

their results to those obtained in the present study, we find similar jump types with comparable proton-oxygen bond lengths. The key differentiator for fast proton conduction in $DyPO_4$ versus $LaPO_4$ is that along the [001] crystallographic direction in the former compound, protons are able to migrate continuously by 0.15 eV inter-tetrahedral jumps that connect every phosphate tetrahedra along this direction. While proton jumps with similarly low activation energies are present for $LaPO_4$, they are not linked to form a continuous path in the monazite crystal structure. Thus, the lower symmetry of this monoclinic structure forces the protons to cross through sites with higher energy barriers regardless of the crystallographic direction.

The benefit of the channels featuring high intrinsic proton mobilities in the xenotime structure relative to the monazite structure would likely be diminished by the presence of the dopant cations, as these are sites for strong binding of the protons. Nevertheless, the fast conduction along the c axis in regions far from the dopants should lead to an overall improvement in proton conductivity in $DyPO_4$ relative to the monazite compounds. Particularly once optimal dopants or co-doping strategies are adopted in textured thin films, the intrinsically high proton conductivity in $DyPO_4$ could lead to significantly enhanced performance as proton-conducting electrolytes relative to other RE-phosphate compounds studied to date.

3.7 Conclusions

Proton diffusion in $DyPO_4$ has been investigated from first principles through DFT total-energy calculations. From the calculated energy barriers and jump attempt frequencies we compute intrinsic proton diffusivities that are highly anisotropic, with an order of magnitude difference between symmetry-distinct components D_{11} and D_{33} at 800 K. The anisotropy of the diffusivity originates from the xenotime structure of this compound which features binding sites for protons that are concentrated within one-dimensional channels running along the c axis. As a consequence, the proton-transfer mechanism in $DyPO_4$ is distinctly different from that found previously for other rare-earth orthophosphate compounds with the monazite crystal structure [76, 70] , and the value of D_{33} for diffusion along the c axis is calculated to be two orders of magnitude larger than computed results for $LaPO_4$ reported in previous calculations at 800K. The addition of divalent dopant cations, which are commonly required to drive proton incorporation in REPs [61, 62, 63, 64, 15, 59, 60] , are expected to lower proton mobilities relative to the intrinsic values reported in the present study. For example, calculations presented here for Ca^{2+} dopants, suggest that these dopants bind protons with an energy of approximately 0.4 eV. Nevertheless, the present calculations suggest that $DyPO_4$ has the potential for high proton conductivity in oriented thin films grown along the c axis with optimized dopant selection and concentration.

3.8 Acknowledgements

This research was supported by the Director, Office of Science, Office of Basic Energy Sciences, Materials Sciences and Engineering Division, of the U.S. Department of Energy under Contract No. DE-AC02-05CH11231. This work made use of computational resources provided by the National Energy Research Supercomputer Center (NERSC), which is supported by the Office of Science of the US Department of Energy under Contract No. DE-AC03-76SF00098. I.M. would like to acknowledge helpful discussions with Hannah Ray and Jonathan Solomon and the support from the University of California Berkeley Chancellor Fellowship.

Chapter 4

Surface Reconstruction and Chemical Evolution of Stoichiometric Layered Cathode Materials for Lithium-Ion Batteries

4.1 Foreword

The work presented in this chapter was published by F. Lin, I. M. Markus, D. Nordlund, T. Weng, M. Asta, M. Doeff, in Nature Communications, vol. 5, article number 3529 (2014), and is reproduced here with the permission of co-authors and publishers (Nature Publishing Group).

4.2 Abstract

The present study sheds light on the long-standing challenges associated with high-voltage operation of $LiNi_xMn_xCo_{1-2x}O_2$ cathode materials for lithium-ion batteries. Using correlated ensemble-averaged high-throughput X-ray absorption spectroscopy and spatially resolved electron microscopy and spectroscopy, here we report structural reconstruction (formation of a surface reduced layer, $R\bar{3}m$ to $Fm\bar{3}m$ transition) and chemical evolution (formation of a surface reaction layer) at the surface of $LiNi_xMn_xCo_{1-2x}O_2$ particles. These are primarily responsible for the prevailing capacity fading and impedance buildup under high-voltage cycling conditions, as well as the first-cycle coulombic inefficiency. It was found that the surface reconstruction exhibits a strong anisotropic characteristic, which predominantly occurs along lithium diffusion channels. Furthermore, the surface reaction layer is composed of lithium fluoride embedded in a complex organic matrix. This work sets a refined example for the study of surface reconstruction and chemical evolution in battery materials using combined diagnostic tools at complementary length scales.

4.3 Introduction

Chemical evolution and structural transformations at the surface of a material directly influence characteristics relevant to a wide range of prominent applications including heterogeneous catalysis[100, 101, 102] and energy storage[103, 104]. Structural and/or chemical rearrangements at surfaces determine the way a material interacts with its surrounding environment, thus controlling the functionalities of the material[105, 106, 107, 108, 109]. Specifically, the surfaces of lithium-ion battery electrodes evolve simultaneously with charge-discharge cycling (that is, $in-situ$ surface reconstruction and formation of a surface reaction layer (SRL)) that can lead to deterioration of performance[103, 104, 110]. An improved understanding of $in-situ$ surface reconstruction phenomena imparts knowledge not only for understanding degradation mechanisms for battery electrodes but also to provide insights into the surface functionalization for enhanced cyclability[111, 112].

The investigation of $in-situ$ surface reconstruction of layered cathode materials, such as stoichiometric $LiNi_xMn_xCo_{1-2x}O_2$ (i.e., NMC), lithium-rich $Li(Li_yNi_{x-y}Mn_xCo_{1-2x})O_2$, lithium-rich/manganese-rich (composite layered-layered) $xLi_2MnO_3(1\text{-}x)LiMO_2$ (M = Mn, Ni, Co, etc) materials, is technologically significant as they represent a group of materials with the potential to improve energy densities and reduce costs for plug-in hybrid electric vehicles (PHEVs) and electric vehicles (EVs) [113, 114, 115, 116]. Practical implementation of some of these materials is thwarted by their high first-cycle coulombic inefficiencies [116, 117, 118, 119], capacity fading [117, 120] and voltage instability [119, 120, 121], especially during high-voltage operation. Specifically, high-voltage charge capacities achieved in lithium-rich/manganese-rich layered cathodes are directly associated with various irreversible electrochemical processes including oxygen loss and concomitant lithium ion removal [122] and electrode/electrolyte reactions [123]. With respect to regular NMC materials, although improved high-voltage cyclability (2.0-4.7 V vs. Li^+/Li) was recently achieved when a small percentage of Co was substituted with Ti (<4%), capacity fading still occurred after extended charge-discharge cycles [117]. Due to the structural and chemical complexities of these layered structures, their fading mechanisms have not been fully resolved. Electron microscopy studies indicated that, in lithium and manganese-rich materials, the capacity fading and voltage decay were partially attributed to structural reconstruction inducing a transition from the layered structure to spinel and/or rock-salt structures at the surface and/or in the bulk [104, 116, 124, 125]. A recent study investigated the atomic structure of Li_2MnO_3 after partial delithiation and re-lithiation to enable improved understanding of lithium-rich/manganese-rich materials [126]. However, these studies were mainly performed using spatially resolved techniques, which fail to account for the inhomogeneous nature of battery electrodes [127, 128, 129]. In addition, the role of electrode-electrolyte interactions in the surface reconstruction and chemical evolution has been rarely studied. The elucidation of the surface reconstruction of stoichiometric NMC materials should provide insights into the fading mechanisms not only for these compounds but also complement the mechanistic paradigm for more complex layered structures including lithium-rich and manganese-rich materials. In order to achieve a statistically viable and spatially visible elucidation (in real

space) for surface phenomena on electrode materials, diagnostic techniques with complementary length scales should be implemented, including high-throughput synchrotron X-ray absorption spectroscopy (XAS) and atomic-scale scanning transmission electron microscopy (STEM) and electron energy loss spectroscopy (EELS).

Here, we report on the surface reconstruction and chemical evolution of stoichiometric NMC layered structures, using ensemble-averaged synchrotron XAS coupled with atomic-scale STEM-EELS, where the surface reconstruction and chemical evolution refer to the formations of surface reduced layer ($R\bar{3}m$ to $Fm\bar{3}m$ transition) and surface reaction layer (SRL), respectively. Our results reveal that the surface reconstruction occurs simultaneously with charge-discharge cycles and is strongly determined by the upper voltage limits used during cycling, electrolyte exposure, and crystal orientations. Furthermore, the major lithium-containing phase in the SRL is identified as lithium fluoride embedded in a complex amorphous organic matrix. The present study provides insights into the surface reconstruction and chemical evolution in NMC materials and directly illustrates the origin(s) of the long-standing challenges involved in cycling NMC materials to high voltages, such as capacity fading, impedance increases and first-cycle coulombic inefficiency. Finally, the study complements the mechanistic understanding of the surface reconstruction in layered materials and sheds light on the possible advantages of conformal functionalization on the surfaces of NMC particles.

4.4 Methods

Preparation of electrode materials

$LiNi_{0.4}Mn_{0.4}Co_{0.18}Ti_{0.02}O_2$ materials were synthesized using a co-precipitation method. For the synthesis of $LiNi_{0.4}Mn_{0.4}Co_{0.18}Ti_{0.02}O_2$, 250 mL of an aqueous solution of transition metal nitrates (0.16 M $Ni(NO_3)_2$, 0.16 M $Mn(NO_3)_2$, 0.072 M $Co(NO_3)_2$), 0.008 M $TiO(SO_4)\bullet xH_2O$ and 250 mL of 0.8 M LiOH aqueous solution were dripped simultaneously into a beaker using a Masterflex C/L peristaltic pump and stirred continuously. The precipitate was collected, filtered and washed with DI water, and then dried overnight at 100^oC in the oven. The dried precipitate was ball-milled with LiOH or Li_2CO_3 and then heated in air at 900^oC for 3 h with a ramp of 2 ^oC/min. The use of Li_2CO_3 led to smaller NMC particles than that of LiOH.

Coin cell preparation and electrochemical measurements

Composite electrodes were prepared with 84 wt% active material, 8 wt% polyvinylidene fluoride (Kureha Chemical Ind. Co. Ltd), 4 wt% acetylene carbon black (Denka, 50% compressed) and 4 wt% SFG-6 synthetic graphite (Timcal Ltd., Graphites and Technologies) in N-methyl-2-pyrrolidinone and cast onto carbon-coated aluminum current collectors (Exopack Advanced Coatings) with typical active material loadings of 6-7 mg/cm^2. 2032 coin

cells were assembled in a helium-filled glove box using the composite electrode as the positive electrode and Li metal as the negative electrode. A Celgard 2400 separator and 1M $LiPF_6$ electrolyte solution in 1:2 w/w ethylene carbonate/dimethyl carbonate (Ferro Corporation) were used to fabricate the coin cells. Battery testing was performed on a computer controlled VMP3 potentiostat/galvanostat (BioLogic). 1C was defined as fully charging a cathode in 1 h, corresponding to a specific current density of 280 mA/g. Electrochemical impedance spectra were collected using a 10 mV AC signal ranging from 10mHz to 100 kHz using this same instrument. The electrodes were removed from coin cells, rinsed with dimethyl carbonate and dried in a helium-filled glove box for further study. The electrodes were sealed under helium and then transferred to the synchrotron beam-line. For electron microscopy and spectroscopy measurements, the electrode particles were scratched off and deposited onto TEM grids.

Materials Characterization

X-ray diffraction (XRD) on powder samples was performed on a Bruker D2 Phaser diffractometer using CuK_α radiation. Scanning electron microscopy (SEM) was performed on a JEOL JSM-7000F with a Thermo Scientific Inc. EDS (energy dispersive x-ray spectroscopy) detector. XAS measurements were performed on the 31-pole wiggler beam-line 10-1 at Stanford Synchrotron Radiation Lightsource (SSRL) using a ring current of 350 mA and a 1000 lmm^{-1} spherical grating monochromator with 20 μm entrance and exit slits, providing 1011 phs^{-1} at 0.2 eV resolution in a 1 mm^2 beam spot. During the measurements, all battery electrode samples were attached to an aluminum sample holder using conductive carbon. Data were acquired under ultrahigh vacuum (10^{-9} Torr) in a single load at room temperature using total electron yield (TEY), Auger electron yield (AEY) and fluorescence yield (FY). The sample drain current was collected for TEY. Auger electron yield (AEY) was collected with a Cylindrical Mirror Analyzer using a pass energy of 200 eV and a kinetic energy window of 2 eV near the main Auger for oxygen and nitrogen, respectively. A silicon diode (IRD AXUV-100) was used to collect the fluorescence yield (FY) positioned near the sample surface. Contributions from visible light were carefully minimized before the acquisition, and all spectra were normalized by the current from freshly evaporated gold on a fine grid positioned upstream of the main chamber. XAS signals were collected at several positions on individual electrodes to ensure that data was representative of the sample. A 200 keV and 300 keV probe-corrected field-emission scanning/transmission electron microscopes (S/TEM) were used for annular dark-field STEM (ADF-STEM) imaging and spatially resolved electron energy loss spectroscopy (EELS). Spectroscopic imaging was performed with an Enfina spectrometer on a Hitachi 2700C dedicated STEM.

Calculation Method

The calculations were carried out using Kohn-Sham density functional theory with the projector augmented wave (PAW) method, as implemented in the Vienna ab initio Sim-

ulation Package (VASP). For the exchange and correlation functional, we use a standard DFT+U framework with spin dependent generalized gradient approximation (GGA) of Perdew, Burke, and Ernzerhof (PBE) [84, 130, 86, 131, 85, 132]. The electron states were sampled using a k-point grid of 2x2x2 centered at the origin. The electronic wave functions were expanded in a plane wave basis set with an energy cutoff of 500 eV, and the ionic positions were optimized until the forces on the ions were converged to 10 meV/Å. The layered NMC material was modeled employing 27 unit cells with a superstructure with space group $P3_112$, while the rock salt structured used space group $Fm\bar{3}m$ employing the same configurational order for the cations as the NMC material. The GGA+U formalism developed by Dudarev et al. [133] was employed for the 3d electrons of each transition-metal cation species. The values of these Hubbard-U parameters for Ni, Mn and Co were initially determined from previous computational work on Li intercalation compounds, and subsequently optimized by iteratively calculating the voltage profile as described by Meng and Dompablo [134], to the values of 5.5 eV, 7.0 eV and 5.0 eV, respectively. In order to determine the relative stability of the layered versus rock salt structure the reaction free energy was calculated for the following reaction at different initial lithium concentrations.

$$2Li_x(Ni_{1/3}Co_{1/3}Mn1/3)O_2 \rightarrow 2(Ni_{1/3}Co_{1/3}Mn1/3)O + O_2 + 2xLi \tag{4.1}$$

The Gibbs free energy for solid species were approximated by the zero-temperature energies, neglecting vibrational contributions and assuming that the configurational disorder in the Ni, Co and Mn sublattice is frozen in at the temperatures of interest. For the oxygen molecule energy the Gibbs free energy was computed using a standard ab-initio thermodynamics formalism, in which the free energy is decomposed into three parts: (i) a zero-temperature energy calculated from DFT, and corrected by an overbinding error as described by Zhou et al. [135], (ii) the zero-point energy of the oxygen molecule, (iii) finite-temperature contributions arising from vibrational, translational and orientational motion, and taken from experimental measurements corresponding to a temperature of 298 K and a partial pressure of 1 atm, and (iv) a term $RTln(p_{o_2}$ to account for variations of the oxygen partial pressure for 1 atm, 10^{-6} atm and 10^{-12} atm.

4.5 Results

Characterization of pristine materials. $LiNi_{0.4}Mn_{0.4}Co_{0.18}Ti_{0.02}O_2$ (abbreviated NMC hereafter) powders with different particle size distributions were used for this study, because previous studies have shown that partial Ti substitution in NMCs results in higher practical specific capacities, better capacity retention upon cycling to 4.7 V versus Li^+/Li, and decreased first-cycle coulombic inefficiencies compared with baseline electrodes [118]. The ratio of transition metals was verified to be close to stoichiometric $LiNi_{0.4}Mn_{0.4}Co_{0.18}Ti_{0.02}O_2$ (Figure A.1). Extensive analysis was performed on the pristine materials to verify the homogeneity of the surface and bulk prior to electrochemical implementation. The combinatorial evaluation was done using a variety of X-ray and electron-based techniques and is shown in

Fig. 4.1. The irregularly shaped primary particles of the NMC powder ranged in size from 100-250 nm across (Fig. 4.1a), indicating that the surface is terminated with various crystal orientations.

The specific surface area of the material was measured to be 9 m^2/g by N_2 physisorption using the Brunauer-Emmett-Teller method (Fig. A.2). An extensive number of atomic resolution annular dark-field STEM (ADF-STEM) images were obtained and representative ones are shown in Fig. 4.1b,c. STEM/EELS analysis was performed for the particle shown in Fig. 4.1b, and it was found that the transition metal oxidation state remains constant from the surface to the bulk (Fig. A.3). Because ADF-STEM images approximately reflect the Z-contrast of materials, the images demonstrate that the material exhibits a well-defined layered structure, and the position of transition metals (3*b* sites) are atomically resolved along the [100] zone axis (Fig. 4.1c). Note that lithium (3*a* sites) and oxygen (6*c* sites) are not visible in the Z-contrast ADF-STEM image due to their low atomic masses. Powder X-ray diffraction (XRD) confirmed that the NMC has the expected $R\bar{3}m$ layered structure (Fig. 4.1d). The refined lattice parameters are consistent with those reported previously for this composition[117] and are summarized in Supplementary Table 1. Depth profiling of the electronic structure was carried out using XAS and STEM-EELS. Transition metal L-edge XAS and EELS measure the dipole allowed transitions from metal 2*p* orbitals to unoccupied metal 3*d* orbitals[136, 137, 138] and indirectly probe the local hybridization states for metal-oxygen octahedral units[139] in an NMC material. Transition metal L-edge XAS is superior to K-edge XAS in terms of resolving local hybridization states, as the former directly probes the unoccupied 3*d* states in the metal 3*d*-oxygen 2*p* hybridized octahedral crystal field. Furthermore, L-edge XAS allows different sample depths to be probed from surface to bulk, depending on the detection modes. In the configuration used for this study, Auger electron yield (AEY), total electron yield (TEY) and fluorescence yield (FY) yield information about the chemical environments with depth sensitivities of 1-2 nm, 2-5 nm and 50 nm, respectively. Note that the FY probing depth is smaller than the particle size of the NMC materials, thus the signal primarily originates from the NMC particles on the top layer of the electrode rather than in the bulk of the composite electrode (typical thickness $\sim$76 μm, Fig. A.4). XAS L-edge spectra of the transition metals exhibit almost identical shapes (for example, $Ni3p_{3/2}$ and $Ni3p_{1/2}$ splitting features) and L2,3 normalized intensities in AEY, TEY and FY modes (Fig. 4.1e-g), which suggest an ensemble-averaged chemical homogeneity in the NMC material. Finally, the formal oxidation states of Ni, Mn and Co are determined to be +2, +4 and +3, respectively, as expected[136, 140, 141, 142]. Furthermore, the formal oxidation state of Ti is +4, and the shape of L-edge verifies the Ti substitution in the $R\bar{3}m$ layered lattice (Fig. A.6). A series of EELS area integrated spectra was recorded to directly assess the homogeneity of the chemical environment in a single NMC particle (Fig. 4.1h) and representative ones are displayed in Fig. 4.1i. The corresponding transition metal L-edge spectra exhibit no variation in the shapes or L3/L2 ratios at different probing positions. Furthermore, the O K-edge shows identical pre-edge peaks that are associated with the transitions from O 1s to O 2p-metal 3d hybridized states and are sensitive to the oxidation states of transition metals[143, 144], which implies that the average oxidation

states of transition metals remain constant from the top surfaces to volumes deep in the bulk. The above ensemble-averaged and spatially resolved spectroscopic studies allow us to conclude that the pristine NMC material exhibits a well-defined $R\bar{3}m$ crystal structure with a homogenous distribution of the electronic structure. Such comprehensive investigation of homogeneity is rarely reported in the literature, although its establishment is critical for resolving the effects of electrochemistry on surface reconstruction and chemical evolution.

Electrochemical Tests of NMC Materials

The electrochemical performances of the NMC materials were evaluated in lithium half-cells, and the cycled electrodes were collected for the subsequent synchrotron X-ray and electron spectroscopy based investigation. There are distinct differences in behavior between the high-voltage cycling (2.0-4.7 V) and lower-voltage cycling (2.0-4.3 V). The NMC material shows a gradually sloping charge profile with no evidence of the high-voltage plateau associated with irreversible loss of lithium and oxygen, commonly seen during electrochemical oxidation of lithium-excess compounds under these conditions[115, 121]. Nevertheless, when repeatedly charged to 4.7 V versus Li^+/Li, the capacity of the NMC electrode decreased with each cycle, while it fades very little during cycling between 2.0-4.3 V (Fig. 4.2a-c). Furthermore, the potential hysteresis between lithium deintercalation (charging) and intercalation (discharging) increased gradually during high-voltage cycling (indicated by the arrows in Fig. 4.2a); namely, larger overpotentials were observed for both processes. Because cycling was carried out between set voltage limits, this impedance rise also contributed to the apparent capacity fading. In contrast, capacity retention was much better when using a lower-voltage limit on charge, that is, when cycling between 2.0-4.3 V (Fig. 4.2b,c). Such pronounced dependence on the voltage cutoff is partially caused by increased cell impedance under the high-voltage cycling conditions, as shown in Fig. 4.2d. The Nyquist plots of the impedance data are composed of a semicircle at high frequencies and Warburg tails at low frequencies, which correspond to charge transfer resistance and mass transfer resistance, respectively. Both charge transfer resistance and mass transfer resistance markedly increased after the extended high-voltage cycling indicated by the increased semicircle radius and the decreased slope of Warburg tail (Fig. 4.2d). In contrast, the charge transfer resistance slightly decreased after lower-voltage cycling between 2.0-4.3 V (Fig. 4.2d), which is likely attributed to cell conditioning and minimal surface reconstruction between 2.0-4.3 V (discussed below). An impedance rise was also observed when the NMC electrode was exposed to the electrolytic solution for an extended period (Fig. 4.2e) without being cycled. The similarities in the behavior suggest that the NMC electrodes undergo similar modifications under conditions of cycling and electrolytic solution exposure, although to a lesser degree for the latter.

Post Analysis of NMC Materials

A correlated study using XAS, EELS and STEM imaging was performed to elucidate the mechanism of capacity fading and impedance rise in NMC cathodes under high-voltage cy-

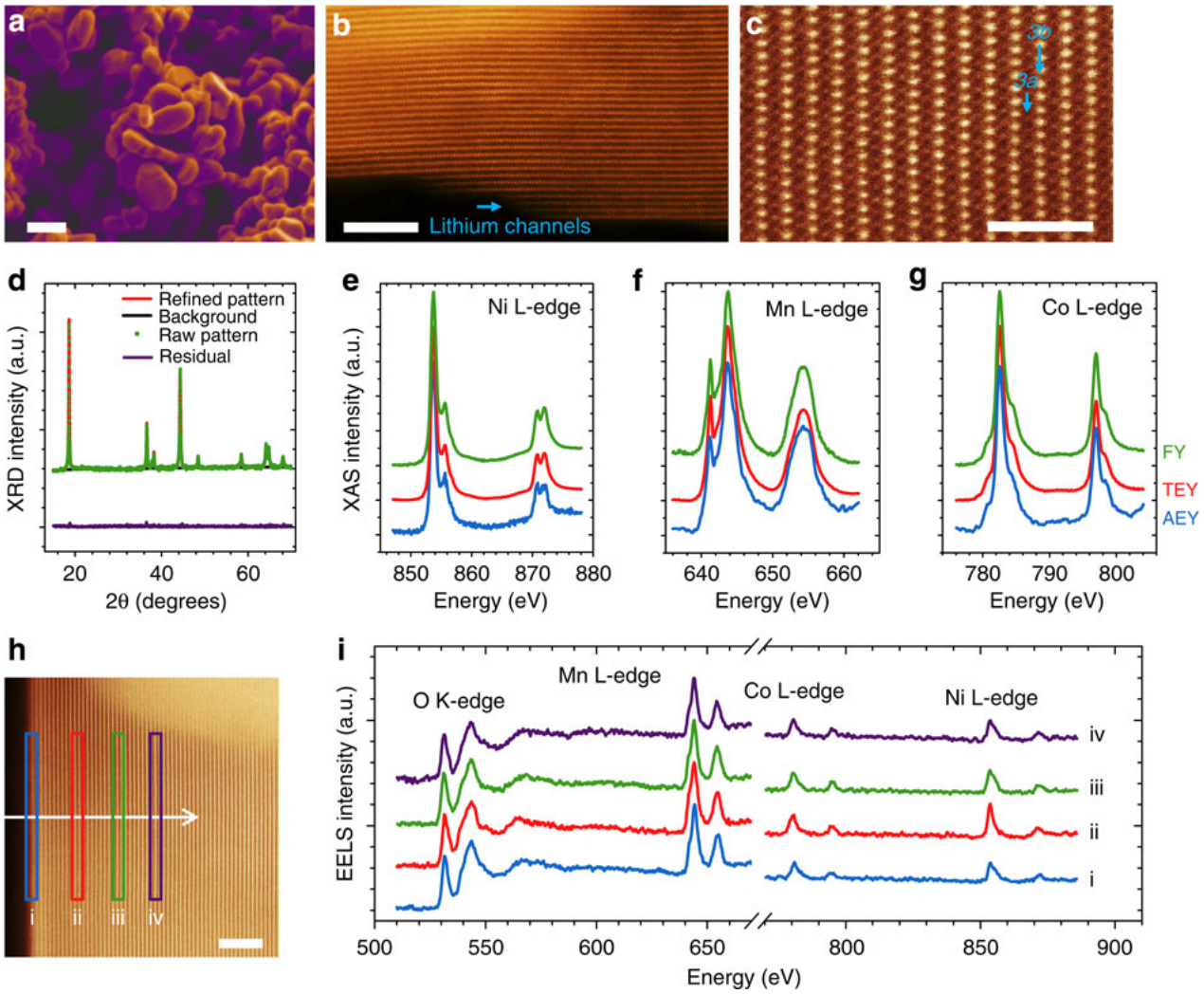

Figure 4.1: (a) SEM image. (b) High-resolution Z-contrast ADF-STEM image. (c) Atomic resolution Z-contrast ADF-STEM image along the [100] zone axis, with the 3*a* and 3*b* sites indicated in the image. (d) XRD pattern with Rietveld refinement (fitted parameters are given in Supplementary Table 1). XAS spectra of (e) Ni L-edge, (f) Mn L-edge and (g) Co L-edge using AEY (blue), TEY (red) and FY (green) modes. (h,i) EELS spectra integrated from areas (i), (ii), (iii) and (iv); see also Fig. A.3 for the spectroscopic imaging of the pristine surface. The scale bars in a,b,c and h are 200nm, 5nm, 2nm and 5nm, respectively.

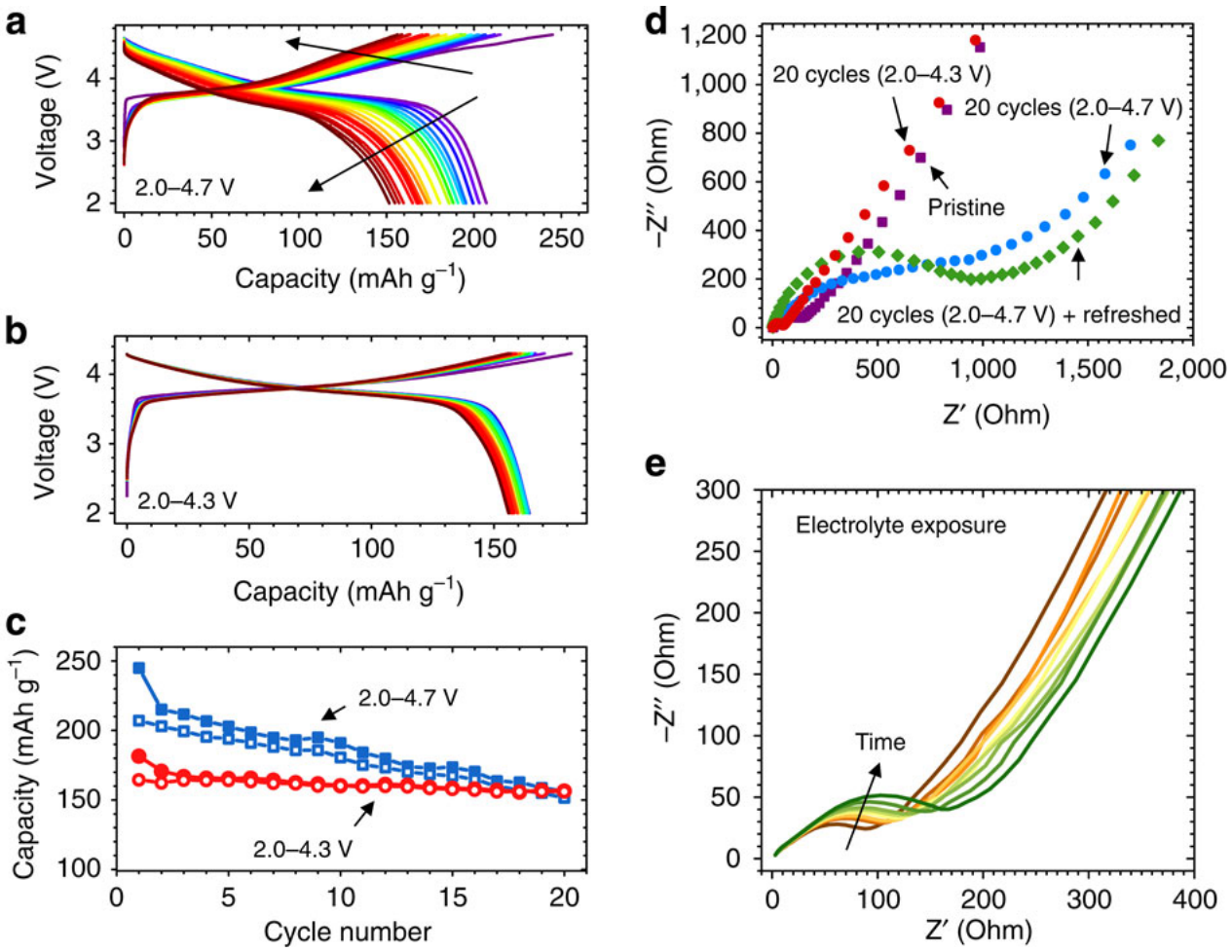

Figure 4.2: Battery cycling performance of NMC materials. (a) Charge-discharge profiles at 2.0-4.7 V for 20 cycles at C/20, where the dashed arrows indicate the gradual capacity fading. (b) Charge-discharge profiles at 2.0-4.3 V for 20 cycles at C/20. (c) Charge and discharge capacities as functions of cycle number at 2.0-4.7 V (blue square) and 2.0-4.3 V (red circle), respectively. The solid and open data points represent charge and discharge capacities, respectively. (d) Nyquist plots of impedance data obtained on cells containing electrodes in the pristine state, cycled at 2.0-4.3 V for 20 cycles, cycled at 2.0-4.7 V for 20 cycles, and in the refreshed state (i.e., rinsed with DMC, reassembled with fresh electrolyte after 20 cycles at 2.0-4.7 V). (e) A series of Nyquist plots for a pristine NMC electrode exposed to electrolytic solution for various periods up to 7 days. The exposure durations were 0 h (pristine), 5 h, 10 h, 1 day, 2 days, 3 days, 4 days, 5 days, and 7 days.

cling conditions. XAS/TEY is suitable for probing electronic structures at the top few nanometers due to the limited penetration depth of soft X-rays[145]. Because the measurements were performed on electrodes in the fully discharged state, nickel consistently showed a formal oxidation state of +2 after extended charge-discharge cycles (Fig. A.7). In contrast, manganese and cobalt underwent significant changes upon cycling. The contribution from the low-energy shoulders of Mn L3- and Co L3-edges grew gradually with increasing numbers of cycles (Fig. 4.3a,b), indicating an evolution of transition metal $3d$ bands to higher occupancies, that is, reduced oxidation states[140, 141, 146]. Furthermore, the oxidation states of transition metals exhibited depth-dependent characteristics, as shown by the direct comparison of AEY, TEY and FY spectra in Fig. 4.3c,d. The low-energy components of Mn L-edge and Co L-edge spectra were more obvious in the AEY mode than those in the TEY and FY modes. Therefore, the reduced Mn and Co species are primarily located at the surface. However, the high-energy component of the L3-edge was always present even in the surface-sensitive AEY mode, which suggests that the reduced Mn and Co species were not evenly distributed on individual NMC particles at the surfaces of the NMC electrodes. This observation coincides with previous studies that show that the charge distribution on the electrode surfaces is inhomogeneous in nature[129]. It is plausible that the reduced species were dominant on certain facets of individual NMC crystals, and that some surfaces exposed to incident X-rays retained the pristine electronic structure. Our subsequent investigation by ADF-STEM imaging further supports this hypothesis. An EELS line scanning profile was obtained on a particle cycled five times (Fig. 3e-h). The variation of the Mn oxidation state along the scanning direction is evident by the blue shift of the absolute energy onset and the reduced L3/L2 ratio[138]. A calculation based on the linear combination of Mn^{2+} and Mn^{4+} was performed and the corresponding concentration profiles are presented in Fig. 4.3h. The concentrations of Mn and Mn were inversely correlated along the scanning reduced layer increased to 3.4 nm (Fig. A.8).

The concentrations of Mn^{2+} and Mn^{4+} were inversely correlated along the scanning direction, with Mn^{2+} primarily dominant on the surface. The thickness of the surface reduced layer was 2nm for this particle, determined by using the intersections of Mn^{2+} and Mn^{4+} concentration profiles (4.3h). An equivalent experimental protocol was applied to an NMC particle cycled 20 times. Along the identical crystal orientation, the thickness of the surface reduced layer increased to $\sim$3.4nm (Fig. A.8). However, low-voltage cycling (2.0-4.3 V) yielded a surface reduced layer with a thickness of 2 nm after 20 cycles (Fig A.9). Another NMC material with identical composition yet smaller particle size was studied to probe the effect of particle size on the surface reduced layer, and the results show that the particle size imposes negligible effects on surface reduced layer within the range in this study (Fig. A.10), and had similar cycling behavior (Fig. A.11).

In addition to the surface reduced layer on the active NMC materials, a surface reaction layer (SRL) was observed after extended charge-discharge cycles (Figure A.12). EELS revealed that the SRL consisted of a lithium fluoride (LiF) phase in a complex organic matrix (Figure A.12). The SRL buildup is partially responsible for the impedance rise (Figure 4.2d). The emergence of the SRL is mainly attributed to the repeated high-voltage electrochemical

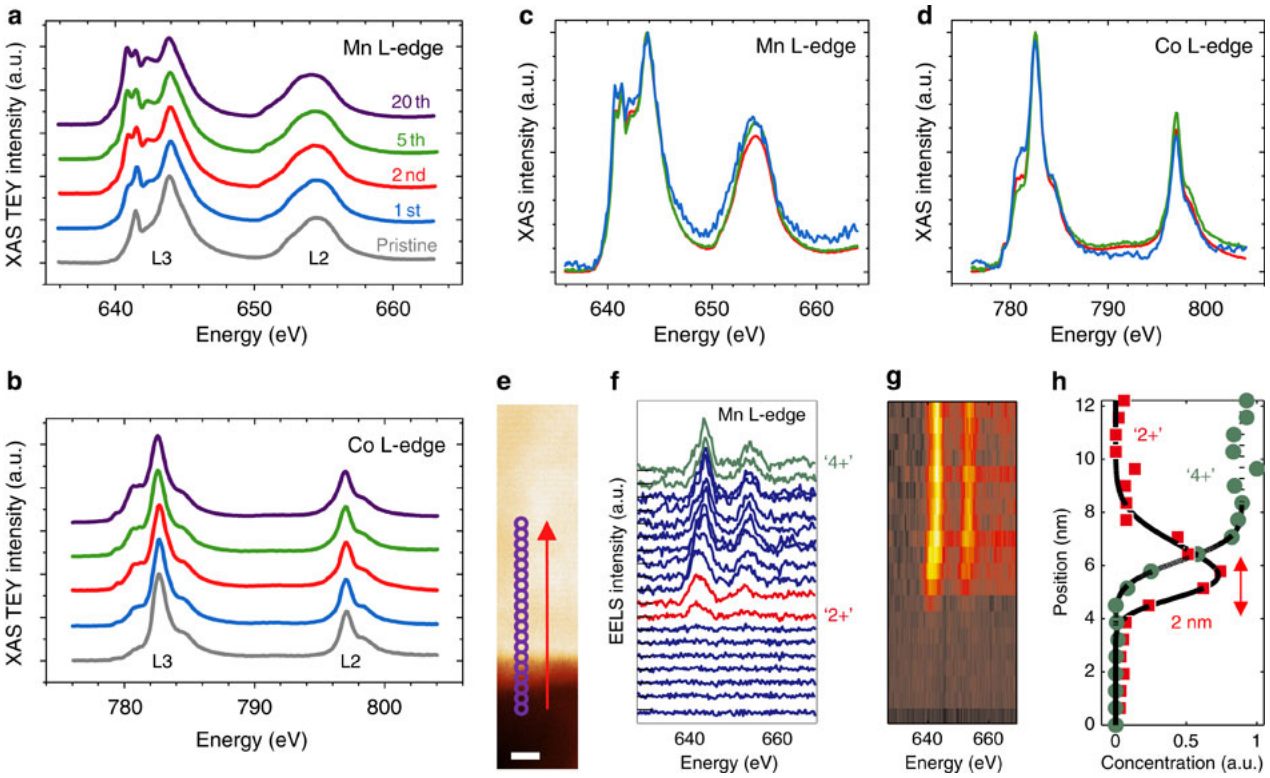

Figure 4.3: (a) Mn L-edge XAS/TEY spectra and (b) Co L-edge XAS/TEY spectra after the designated number of cycles. (c) Mn L-edge XAS spectra and (d) Co L-edge XAS spectra for an electrode after two charge-discharge cycles in the AEY (blue), TEY (red) and FY (green) modes. EELS line scan profile for an NMC particle along the <001> direction after five cycles: (e) STEM image for the scanning pathway, (f) Mn L-edge EELS spectra along the scanning pathway, (g) 2D EELS map visualizing the peak shift and (h) concentration profiles for Mn^{2+} and Mn^{4+} obtained from the data using a linear combination method. All the measurements were performed on electrodes in the fully discharged state after cycling between 2-4.7V versus Li^+/Li. The scale bar in (e) is 2nm.

processes, because it was barely observed in the electrode that was cycled to the low voltage (Fig. A.13) or exposed to the $LiPF_6$/EC-DMC solution for 7 days, without being cycled (Fig. A.14).

The capacity retention of NMC materials is compromised when high-voltage cycling, such as 4.7 V vs. Li/Li^+, is used. Here we show that the surface reduced layer is related to the inferior capacity retention observed under high-voltage cycling conditions. As shown in Figures 4.4a and 4.4b, the relative amounts of reduced transition metals were higher after high-voltage cycling (2.0-4.7 V vs. Li/Li^+) than after lower-voltage cycling (2.0-4.3 V vs. Li/Li^+). These results suggest that the layered lattice is disrupted at high voltages resulting in a formation of a metastable phase that is readily reduced under discharging condi-

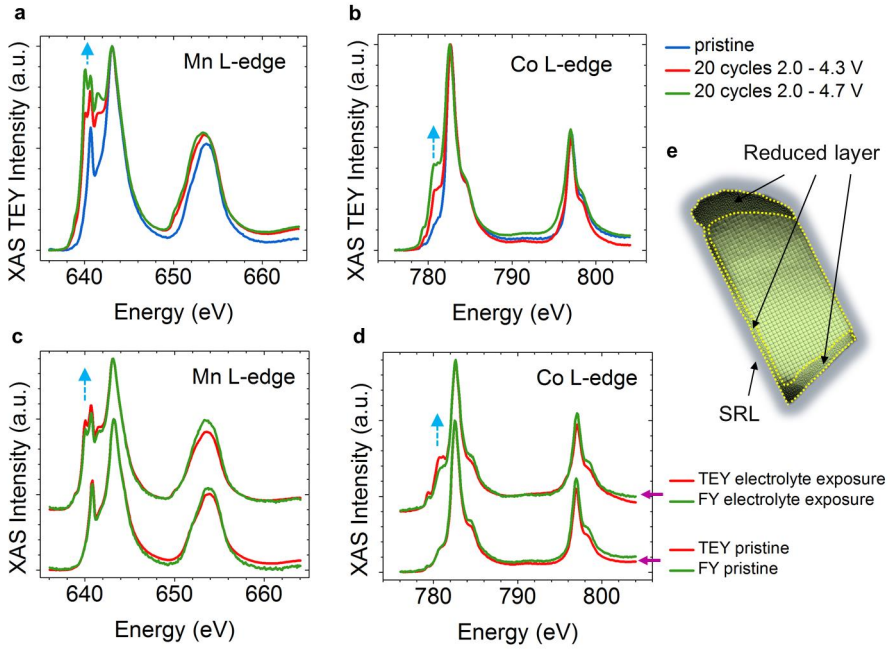

Figure 4.4: Dependence of surface reduced layer on cycling voltages and electrolyte exposure. (a) Mn L-edge XAS/TEY spectra, (b) Co L-edge XAS/TEY spectra and (c) Mn L-edge XAS spectra of pristine and cycled electrodes (20 cycles). (d) Co L-edge XAS/TEY and FY spectra of a pristine electrode and one exposed to electrolytic solution for 7 days. The blue dashed arrows in (a-d) indicate the increase of transition metals having low oxidation states. (e) Schematic model of a NMC particle with a surface reduced layer and a SRL.

tions. Presumably, the surface reduced layer creates a passivation layer that inhibits efficient lithium diffusion, thus adversely impacting capacity retention. This hypothesis is further justified by several control experiments. First, after high-voltage cycling, the electrodes could not be revitalized to the initial state by reassembling the cell with fresh electrolytic solution (Fig. A.15a), because this did not reduce the impedance (Figure 4.2d). Second, the capacity normally obtained with low-voltage cycling (2.0-4.3 V vs. Li/Li^+) could not be restored after high-voltage cycling (Fig. A.15b). Third, the high-voltage capacity could be improved only by using an extremely slow charge/discharge rate even after 20 high-voltage cycles (Fig. A.15c). These observations indicate that the cycling losses imposed by high-voltage cycling are mainly due to the impedance rise caused by the surface reduced layer and surface reaction layer rather than changes in the bulk electrode material. Previous studies have attributed the surface reduced layer mainly to electrochemical processes with little attention dedicated to the effects of electrode-electrolyte reactivity [147, 104, 116]. Here we found that a surface reduced layer similar to the ones observed during high-voltage cycling is also created after an NMC electrode was immersed in the electrolyte (Figures 4.4c and 4.4d), although it is thinner. In addition, its buildup leads to gradually increased charge transfer resistance (Figure

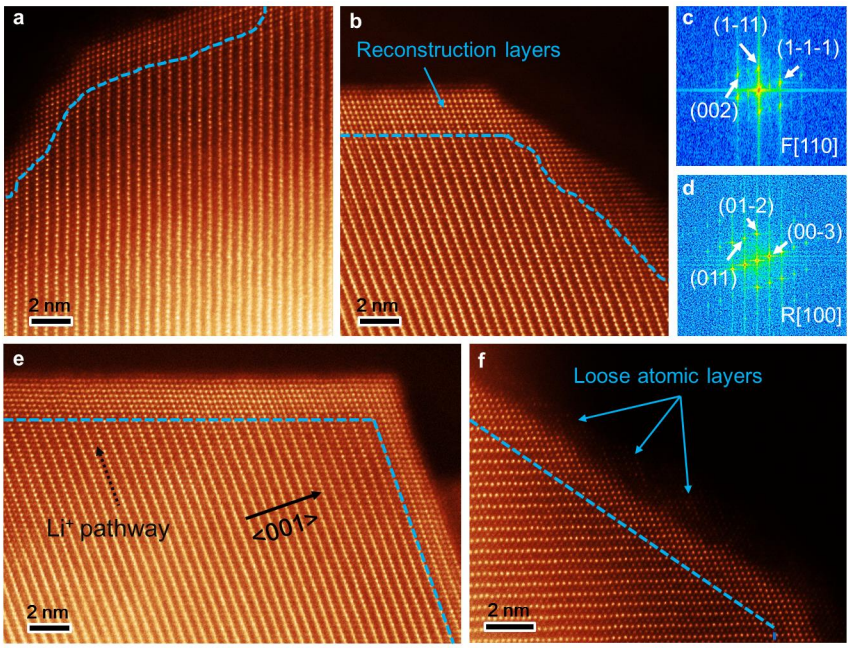

Figure 4.5: Atomic resolution ADF-STEM images of NMC particles. (a) After electrolyte exposure (the exposure time is approximately 30 hours, equivalent to the time used for one full cycle in this study). (b) After 1 cycle; the blue arrow indicates the surface reconstruction layer. (c and d) FFT results showing the surface reconstruction layer ($Fm\bar{3}m$ [110] zone axis) and the NMC layered structure ($R\bar{3}m$ [100] zone axis) respectively in (b). (e) Showing variation of the surface reconstruction layer thickness on orientation after 1 cycle. (f) Image showing loose atomic layers on an NMC particle, after 1 cycle. Dashed lines indicate the boundaries between the NMC layered structure and surface reconstruction layer in all images.

4.2e). After extended cycling, the surface reduced layer originates from dual effects involving both the electrode-electrolyte reactivity and electrochemical activation. The immediate generation of the reduced surface upon exposure to electrolyte may also be responsible for the first-cycle coulombic inefficiencies that are usually observed with NMC electrodes even when cycled conservatively, using voltage limits well below the oxidative stability limit of the electrolytic solution.

In the above discussion, XAS and EELS spectroscopies provided correlated evidence for the surface reduced layer and chemical evolution via the elucidation of local electronic structures primarily at the vicinity of NMC particle surfaces. The changes in electronic structures must be associated with the collapse and rearrangement of local crystal structures; i.e., lattice reconstruction. The atomic-resolution ADF-STEM imaging allows the visualization of the localized structural rearrangements at surfaces with the sensitivity of a single atom. A surface reconstruction layer is readily observed after the electrolyte exposure experiment (Figure 4.5a), where the blue line indicates the boundary between the NMC $R\bar{3}m$ layered

structure and the surface reconstruction layer. The thickness of the surface reconstruction layer increased after one complete cycle between 2.0-4.7 V (Figure 4.5b) relative to that observed on the particle that was exposed to the electrolytic solution without electrochemical cycling (although the duration of the two experiments was identical). The observation visually validates our previous conclusion that this layer originated from dual effects involving both electrode-electrolyte reactivity and electrochemical activation. The crystal structure of the reconstruction layer consists primarily of an $Fm\bar{3}m$ rock-salt structure (Figures 4.5c and 4.5d), with a few atomic layers of spinel structure as a bridge between the layered structure (containing Ni^{2+}, Mn^{4+} and Co^{3+}) and rock-salt structure (containing Ni^{2+}, Mn^{2+} and Co^{2+}). By analyzing a large number of ADF-STEM images, we found that the surface reconstruction layer was greatly influenced by crystal orientations. Figure 4.5e shows a typical example of orientation-dependent surface reconstruction (more relevant images are available in Supplementary Fig. A.16) . Furthermore, reconstruction-poor and -rich surfaces are occasionally observed on the same NMC particle after cycling (Fig. A.16). Due to the random orientation of NMC particles on the electrode surfaces, surface-sensitive XAS spectroscopy (i.e., AEY, TEY) yields an average of the electronic structures for reconstruction-poor and -rich surfaces, and thus the high-energy components of XAS/AEY and XAS/TEY are still present in the electrodes that have been cycled (Figures 4.3c and 4.3d). In general, the thicker surface reconstruction layers are observed along lithium diffusion channels relative to other orientations (e.g., <001>), suggesting that surface reconstruction is promoted by lithium removal during charging, and the reconstruction is more severe in the regions that undergo dynamic lithium transport. Interestingly, we also observed dangling layers (i.e., loose atomic layers) of the cubic rock-salt structure (indicated by blue arrows in Figure 4.5f) at the external surface of reconstruction layers. These loosely attached atomic layers are susceptible to dissolution into electrolytes and coincide with the suspected Mn2+ dissolution in a variety of Mn-containing cathodes [148, 149, 103]. It has been shown in Figure A.15c that, after 20 high-voltage cycles, the discharge capacity could be nearly recovered at a slow rate (190 mAh/g, compared to the first cycle discharge capacity of 210 mAh/g). Therefore, the transition metal dissolution accounts for a capacity loss of no more than 20 mA/g. Finally, we performed DFT calculations of the energy of formation of the rock salt structure from the layered structure as a function of lithium concentration (Fig 4.6). Under oxygen partial pressure ranging from 10^{-12} atm to 1 atm we found that after about 60% of lithium has been removed from the NMC structure, it becomes favorable to form the rock salt structure (i.e., negative formation energy). This supports the above results showing that the high-voltage cycling (i.e., more lithium ions are removed) leads to a much more severe buildup of the surface reduced layer (i.e., rock salt structure). Our experimental results showed that the $R\bar{3}m$ to $Fm\bar{3}m$ transition primarily occurred at the surface and direct exposure to electrolytic solution assisted the kinetics of this phase transition.

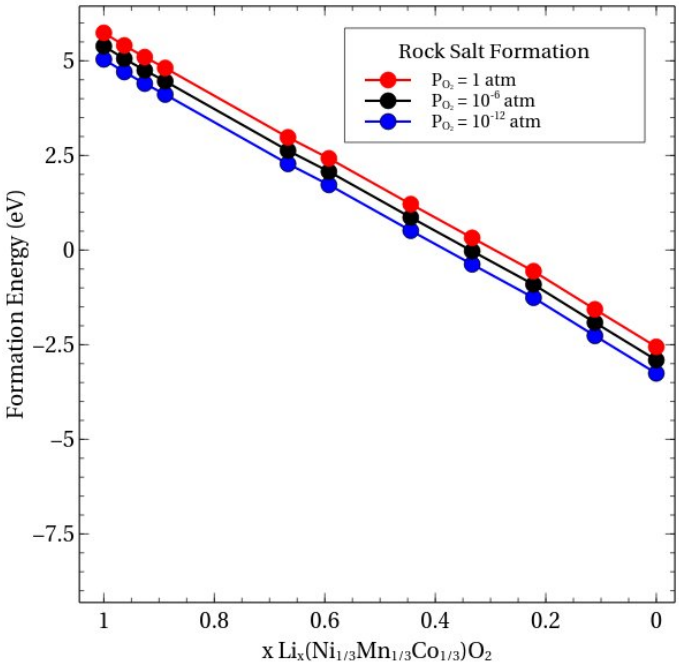

Figure 4.6: Formation energies of rock salt structure as functions of lithium stoichiometry and oxygen partial pressure.

4.6 Conclusion

We correlated cycling performance with the observation of structural reconstruction and chemical evolution at the surfaces of stoichiometric NMC materials using statistically viable high-throughput ensemble-averaged XAS as well as spatially resolved EELS and atomically resolved ADF-STEM imaging. The structural reconstruction was directly evidenced by the changes in the transition metal oxidation states and the atomic packing, which were achieved by synchrotron XAS and ADF-STEM, respectively. Our findings show that the challenge of achieving stable high-voltage cycling of the NMC electrodes lies with structural and chemical metastability at the surfaces. Upon cycling and/or electrolyte exposure, the surfaces of NMC particles undergo progressive reconstruction (i.e., lower transition metal oxidation states, Figures 4.3a and 4.3b) from an $R\bar{3}m$ layered structure to an $Fm\bar{3}m$ rock-salt structure in addition to the buildup of a complex surface reaction layer containing LiF and organic components (i.e., chemical evolution). These observations provide new insights into the capacity degradation and impedance buildup in stoichiometric NMC materials undergoing high-voltage cycling conditions. Interestingly, the structural reconstruction at the surface is highly anisotropic, and primarily occurs along the lithium ion transport direction. This phenomenon would not have been observed without such a study at complementary length scales. This finding suggests that conformal protection coatings on certain orientations of

NMC particles should be more beneficial than those on other orientations provided that the conformal coating is capable of inhibiting surface reconstruction and allows for efficient lithium diffusion.

4.7 Acknowledgment

This work was supported by the Assistant Secretary for Energy Efficiency and Renewable Energy, Office of Vehicle Technologies of the U.S. Department of Energy under Contract No. DE-AC02-05CH11231 under the Batteries for Advanced Transportation Technologies (BATT) Program. The synchrotron X-ray portions of this research were carried out at the Stanford Synchrotron Radiation Lightsource, a Directorate of SLAC National Accelerator Laboratory and an Office of Science User Facility operated for the U.S. Department of Energy Office of Science by Stanford University. S/TEM and EELS experiments were performed at the Center for Functional Nanomaterials, Brookhaven National Laboratory, which is supported by the U.S. Department of Energy, Office of Basic Energy Sciences under Contract No. DE-AC02-98CH10886, and at National Center for Electron Microscopy (NCEM) of the Lawrence Berkeley National Laboratory (LBNL), which is supported by the U.S. Department of Energy (DOE) under Contract No. DE-AC02-05CH11231. This work made use of computational resources provided by the National Energy Research Supercomputer Center (NERSC), which is supported by the Office of Science of the US Department of Energy under Contract DE-AC03-76SF00098. I.M.M acknowledges the support of the NSF graduate research fellowship program.

Chapter 5

Computational and Experimental Investigation of Ti Substitution in $Li_1(Ni_xMn_xCo_{1-2x-y}Ti_y)O_2$ for Lithium-Ion Batteries

5.1 Foreword

The work presented in this chapter was published by I. M. Markus, F. Lin, K. Kam, M. Asta, M. Doeff, in the Journal of Physical Chemistry Letters, vol. 5, issue 21, pages 3649-3655 (2014), and is reproduced here with the permission of co-authors and publishers (American Chemical Society).

5.2 Abstract

Aliovalent substitution of cations in layered transition metal cathode materials has been demonstrated to provide a pathway for improvement of the energy and power densities of lithium-ion batteries, yet the mechanisms underlying such effects remain incompletely understood. The reasons for performance enhancement associated with Ti substitution of Co in the layered cathode material $Li_1(Ni_xMn_xCo_{1-2x})O_2$ were investigated using density functional theory calculations, including Hubbard-U corrections. An examination of the structural and electronic modifications at different degrees of lithium removal revealed that Ti substitution reduces the structural distortions occurring during delithiation, due to the larger cation radius of Ti^{4+} relative to Co^{3+}, and the presence of an electron polaron on Mn cations induced by aliovalent Ti substitution. The structural differences were found to correlate with a decrease in the lithium intercalation voltage at lower lithium concentrations, which is consistent with the quasi-equilibrium voltage obtained by integrating data from a stepped potential experiment. Further, Ti is found to stabilize thermodynamically the

layered structure, suppressing the formation of a secondary rocksalt phase at high voltage. Our results provide insights into the ways selective doping can enhance the performance of Li-ion cathodes by tuning specific parameters such as the equilibrium intercalation voltage. These enhancements are critical for maximizing the power density and lifetime of batteries that employ current organic electrolytes.

5.3 Introduction

Over the last two decades rechargeable Li-ion batteries have been successfully used in portable electronic devices, and more recently advances in performance and manufacturing have permitted commercial endeavors to be taken for grid storage and transportation applications. In order to further enable Li-ion batteries for these newer applications and properly leverage the expertise and manufacturing investments already made, additional improvements in cost, lifetime, and power density are required [19, 149]. The class of stoichiometric layered compounds $Li_1(Ni_xMn_xCo_{1-2x})O_2$ known as NMCs, illustrated in Fig.5.1, are attractive cathode materials for Li-ion batteries due to the high rate capability, high capacity, reduced Co content compared to $LiCoO_2$, and superior structural stability relative to lithium rich compounds [150, 151, 152, 153]. Recently NMCs have been reported to exhibit enhanced performance when Ti^{4+} substitutes Co^{3+} by 2-4% [154], exhibiting better first cycle Coulombic efficiency, increased capacity, and enhanced cycling stability. Some of these improvements have also been reported for NMCs containing less than 5% of La, Ce, Pr, Mo or Al [155, 156, 157, 158, 159, 160] as well as in doped $LiFePO_4$ and $LiMn_2O_4$ [161, 162, 163]. Collectively, these results demonstrate the capability of tuning electrode performance by selective atomic substitutions. For this strategy to be successfully implemented the exact mechanism by which such improvements occur should be better understood, which requires detailed investigations into the ways in which substitutions affects the properties of the system [155].

In this letter, we consider the correlation between electronic and structural changes achieved by small (<5%) Ti substitution of Co in NMCs and the subsequent impact on thermodynamic properties in the context of improved cell performance. By employing density-functional theory (DFT) calculations we show how the local structural distortions generated through Ti substitution at different lithium concentrations affect the lithium intercalation voltage and the formation energy of a secondary rocksalt structure. We find that Ti decreases overall changes in the lithium interstitial volume during cycling, which coincides with a decrease in the intercalation voltages at the lower lithium concentrations. Furthermore, we find that Ti substitution suppresses the formation of a secondary rocksalt phase, which has recently been shown to increase the overall battery impedance leading to capacity fading when cycling to voltages above 4.5V and constant C rates[164]. This finding can be significant for other cathode systems that undergo similar electrochemically activated transformations at high voltages. One such case is seen for the Li_2MnO_3 structure, which is believed to be the component of the high capacity Li rich composite cathodes [165] active beyond 4.4 V.

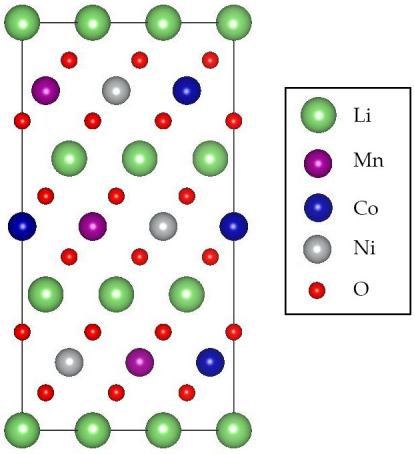

Figure 5.1: Computational model of the crystal structure of NMC with space group $P3_112$.

Because the transformation for these compounds is not reversible it leads to voltage fading preventing their use at higher voltages, thus reducing their overall power density.

5.4 Methods

Computational

DFT calculations were performed with the projector augmented wave (PAW) method [84, 85], as implemented in the Vienna Ab-initio Simulation Package (VASP) [86, 87]. The calculations made use of the spin-dependent generalized gradient approximation of Perdew, Burke and Ernzerhof (PBE) [**Perdew1997**], including Hubbard-U corrections following the formalism developed by Dudarev et al. [166]. The electron states were sampled using a k-point grid of 2x2x2 centered at the origin. The electronic wave functions were expanded in a plane wave basis set with an energy cutoff of 600 eV, and the ionic positions were optimized until the forces on the ions were converged to 10 meV/Å. The values for the Hubbard-U parameters for Ni, Mn and Co were initially determined from previous computational work on Li intercalation compounds [167], and subsequently optimized by iteratively calculating lithium intercalation voltage profiles that also exhibit the order of oxidation previously reported in the literature of Ni^{2+}/Ni^{3+}, Ni^{3+}/Ni^{4+}, and Co^{3+}/Co^{4+} [155, 168]. The final values of used for the calculations were 5.5 eV, 7.0 eV and 5.0 eV for Ni, Mn and Co, respectively. Detailed results associated with the selection of the Hubbard-U parameters are provided in the supplemental material.

The calculations for NMC compounds made use of a supercell geometry containing 27 formula units (see Fig. 5.1) and a space group $P3_112$ [169]. This structure exhibits a local ordering of the transition metals, and thus a lower symmetry than the $R\bar{3}m$ space group corresponding to a disordered solid solution. The supercell model was selected in order to

minimize the number of different structural arrangements in the metal layer, with the additional consideration that the periodic boundary conditions would also create an ordered system. The impact of the supercell geometry was checked by generating an additional structure that had equal distribution of each transition metal by layer but with local ordering generated only by the periodic boundary conditions. We found that lattice parameter changes and lithium intercalation values did not significantly change, with the results falling within the standard errors in the mean reported. Structural parameter changes and lithium intercalation voltage differences were calculated at each lithium concentration by averaging over five structures with different lithium arrangements for normal and substituted NMC.

In order to determine the relative stability of the layered versus rock salt structure the reaction free energy was calculated for the following reaction at different initial lithium concentrations.

$$2Li_x(Ni_{1/3}Co_{1/3-y}Mn_{1/3}Ti_y)O_2 \rightarrow 2(Ni_{1/3}Co_{1/3-y}Mn_{1/3}Ti_y)O + O_2 + 2xLi \qquad (5.1)$$

Where the first term represent the NMC structure previously described, followed by the rocksalt structure (space group $Fm\bar{3}m$) which is also modeled with a supercell containing 27 formula units with the same transition metal arrangement as the layered structure. The last two terms correspond to the oxygen dimer and bcc lithium metal, respectively. The Gibbs free energy for solid species were approximated by the zero-temperature energies, neglecting vibrational contributions and assuming that the configuration disorder in the Ni, Co and Mn sublattice is frozen in at the temperatures of interest. For the oxygen molecule the Gibbs free energy was computed using a standard ab-initio thermodynamics formalism, in which the free energy is decomposed into three parts: (i) a zero-temperature energy calculated from DFT, and corrected by an over-binding error as described by Wang2006a, (ii) the zero-point energy of the oxygen molecule, (iii) finite-temperature contributions arising from vibrational, translational and orientational motion, and taken from experimental measurements corresponding to a temperature of 298 K and a partial pressure of 1 atm, and (iv) a term RT $ln(p_{O_2})$ to account for variations of the oxygen partial pressure of 10^{-6} atm. The low partial pressure was selected to simulate typical oxygen concentrations during battery cell assembly, approximately 0.5 ppm.

Experimental

$Li_1(Ni_{0.33}Mn_{0.33}Co_{0.33-y}Ti_y)O_2$ compounds were synthesized by the glycine-nitrate combustion process described by Kam *et.* al[154]. To prepare electrodes, the active material was mixed with polyvinylidene fluoride (PVdF, Kureha Chemical Ind. Co. Ltd.), acetylene black (Denka, 50% compressed) and SFG-6 synthetic graphite (Timcal Ltd., Graphites and Technologies) in the ratios 84:8:4:4, in N-methyl-2-pyrrolidinone to make a slurry. Once homogenized, the slurry was cast onto a carbon-coated Al-foil current collector (Exopack Advanced Coatings) and dried in air and under vacuum at 120 for 12 hours. Electrodes

were then cut to size and 2032 coin cells were assembled using Celgard 3401 soaked with a solution of 1M $LiPF_6$ in 1:2 ethylene carbonate: dimethyl carbonate (EC-DMC, Ferro Corp.) as the electrolytic solution and lithium foils as anodes. Slow stepped potential experiments were carried out on a MacPile II (Bio-logic, S.A., Claix, France) galvanostat/potentiostat. For these experiments, 10 mV potential steps were used, and the next step was taken when the current fell to 1/60000 of the initial value or an absolute value of 0.008 mA, whichever came first. This was equivalent to a rate of approximately C/100 (removal of one lithium per formula unit in 100 hours). Data was integrated to produce quasi-equilibrium V vs. x curves.

To investigate the effect of Ti substitution on NMCs we considered the different experimental results observed and provide insights derived from electronic-structure calculations based on density functional theory with Hubbard-U corrections.. We first consider the structural changes that occur during delithiation of the NMC structure. Experimentally, Ti substitution is found to lead to a smaller decrease in the overall volume change during cell cycling relative to the unsubstituted material [154]. The smaller volume change during cycling should provide added structural stability, particularly when charging to high voltage (4.7V vs. Li^+/Li). Figure 5.2a and 5.2b shows the calculated change in the lattice parameters during lithium removal along with experimental measurements taken from Kam *et.* al[154]. The calculations reproduce the experimental trends, in that Ti substitution reduces the change in the a parameter at lower Li content while not significantly affecting the change in the c parameter. Figure 5.2c shows the average lithium interstitial volume calculated as a function of lithium concentration. The interstitial volume was calculated using the agorithm of Swanson and Peterson [170], as implemented in the VESTA molecular viewer software [171]. The results show that the lithium interstitial volume is less expanded during charging for the Ti substituted structure. Changes to the lithium interstitial volume has been previously related to the mobility of lithium in the NMC structure [160] which is related to the overall stability of lithium in the structure. Figures 5.2d and 5.2e show the MO_6 octahedron around each lithium after two thirds have been removed from the structure, and illustrate distortions in the regular NMC compared to the Ti substituted structure.

Our calculations show that the structural differences can be attributed first to the substitution of Co^{3+} with the larger Ti^{4+} cation, which expands the surrounding MO_6 octahedra, and, second, to the formation of a charge compensating electron polaron on a nearby Mn^{+3} (Fig. 5.3) that also expands the surrounding MO_6 octahedra. These two new structural features evolve differently once lithium is removed. As expected the distortions around the Ti cation persist since Ti^{+4} is electrochemically inactive, while the electron polaron will oxidize once lithium is removed. However, because aliovalent substitution provides an extra electron, for a given delithiation amount we find fewer of the Ni/Co redox centers fully oxidized, which aids in volume preservation. Table 5.1 shows the average bond length between oxygen and each transition metal with their different oxidation states. As expected the more oxidized species have shorter bonds, which combined with the larger Ti cation size, results in a decrease of structural changes during cycling.

Figure 5.4a shows the calculated intercalation voltage for regular NMC and Ti substituted

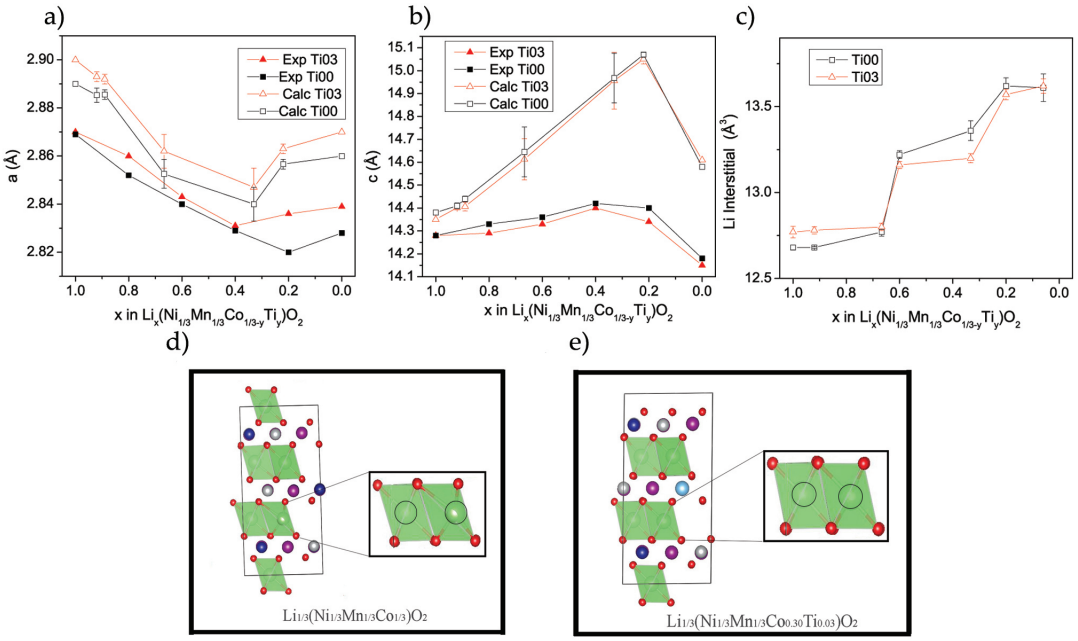

Figure 5.2: (a) and (b) Experimental and calculated changes in a and c lattice parameters as a function of lithium concentration for regular and Ti substituted NMC. Experimental data was taken from Kam et al.[154] and is labeled "Exp Ti00" or "Exp Ti03" indicating the Ti content. Calculated lattice parameters are labeled "Calc Ti00"' or "Ti 03" also indicating Ti content of zero or 3 %, respectively. c) Changes in the Li interstitial volume. (d) and (e) Shows oxygen octahedra around lithium cations after 2/3 of lithium has been removed for regular and Ti substituted NMC. In panels (a) - (c) the error bars denote the standard error in the mean value averaged over 5 different randomly generated configurations for Lithium at each concentration.

NMC. Taking the average intercalation voltage of at least 5 different lithium arrangements, we calculated that Ti substitution should decrease the intercalation voltage at low lithium content. This finding matches experimental results for stepped potential charging (Figure 5.4b), which indicates that under equilibrium conditions Ti substitution lowers the intercalation voltage. This lower equilibrium potential reduces the overpotential required to drive lithium deintercalation allowing more lithium to be accessed, providing an explanation for the increased capacity found experimentally. These results are analogous to previous findings that through Fe addition to NMC the intercalation voltage can be raised [155]. These findings demonstrate the capability for tuning electrode performance by manipulating the voltage of NMCs in order to deliver superior energy density for batteries.

Another contributing factor for the increased capacity found experimentally comes from the improved first cycle coulombic efficiency and decreased discharge capacity fading with prolonged cycling. This effect becomes more pronounced when cells are charged to higher

Table 5.1: Average calculated O-M bond lengths

Metal - O	Average bond length (Å)
Mn^{+3} - O	1.98
Mn^{+4} - O	1.93
Ni^{+2} - O	2.07
Ni^{+3} - O	1.92
Ni^{+4} - O	1.88
Co^{+3} - O	1.93
Co^{+4} - O	1.89
Ti^{+4} - O	1.96

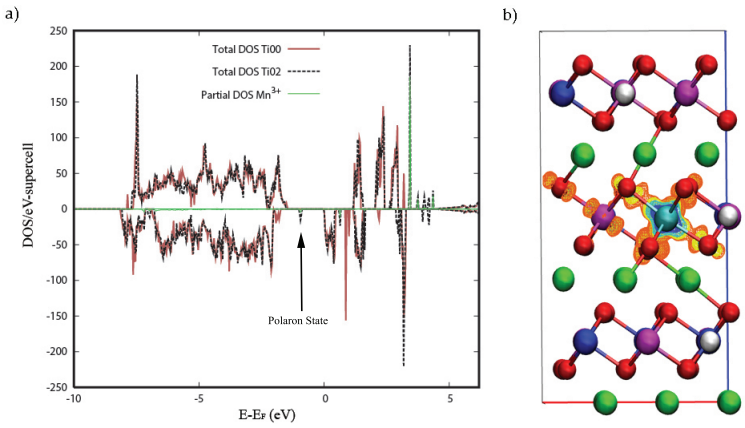

Figure 5.3: Shows the localized polaron by plotting (a) total density of states (DOS) for regular NMC (red line) and Ti substituted NMC (black line), including the projected DOS for the Mn^{+3} cation (green line). (b) The charge density difference map between regular and Ti substituted NMC. The color balls represent green for Li, red for O, blue for Co, white for Ni, purple for Mn. The color bands represent charge depletion for the blue bands and charge accumulation for yellow and orange bands.

voltages (>4.3V). At high states of charge, there may be accelerated electrolyte decomposition but there is also evidence of phase transformation from the layered NMC structure to a rock salt oxide at the surface of particles [164]. This surface reconstruction requires that oxygen and lithium be lost, and although the loss of active material is small during initial cycles, the buildup of this secondary phase increases impedance that results in an exaggerated practical capacity loss. Figure 5.5 compares the free energy change at room temperature for the formation of the rocksalt structure from the NMC (see Eq. (5.1) in the Methods section below) at different lithium concentrations for the regular and Ti substituted NMC. The calculated results indicate that Ti helps stabilize the NMC structure by increasing the energy of formation of the rock salt structure and more strongly binding oxygen. This result agrees with previous reports that Ti has higher O binding energy compared to the other

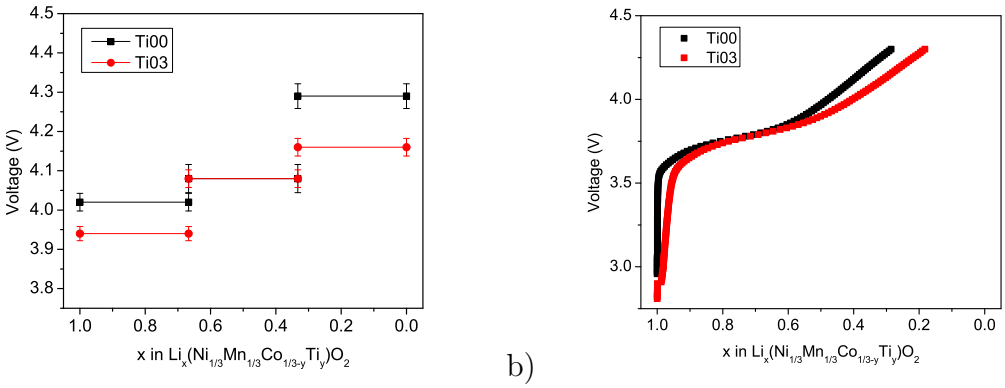

Figure 5.4: a) Calculated intercalation voltage at 0 K and b) experimental quasi-equilibrium voltage obtained by integrating data from a stepped potential experiment. The error bars in panel a) denotes the standard error in the mean value

metals in NMC, and offsets oxygen depletion to higher states of charge [172, 173].

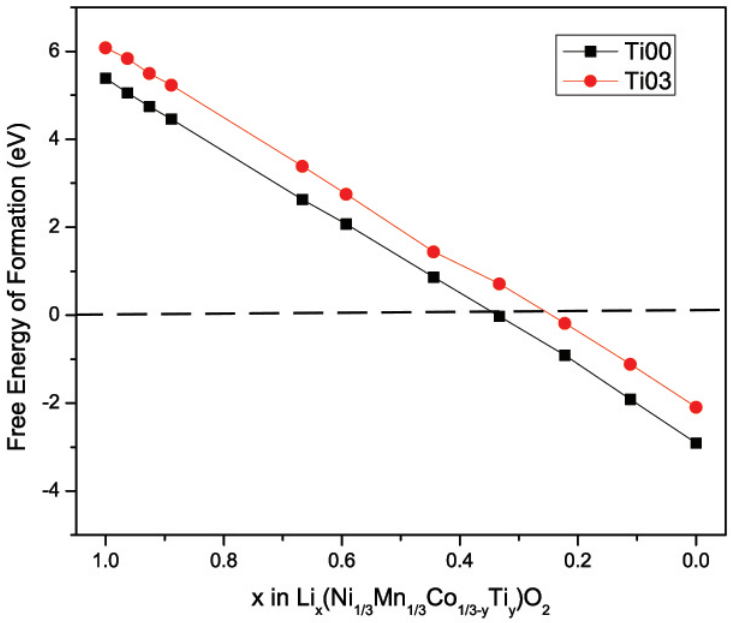

Figure 5.5: Calculated free energy of formation at room temperature for the rocksalt structure from NMC structures with different lithium concentrations. The black line (Ti00) corresponds to regular NMC, and the red line (Ti03) corresponds to Ti-substituted NMC.

5.5 Conclusion

The calculations performed not only help identify the role Ti has on the performance of NMC cathodes, but suggests important selection criteria for substituting cations in order to tune the properties of layered cathode materials. To decrease the lithium intercalation voltage: (i) Substituting cations should have larger ionic radii in order to decrease the lithium interstitial volume. (ii) In case the substitutional cation is electrochemically inactive aliovalent substitutions that result in the formation on an electron polaron will also decrease changes to the lithium interstitial volume during delithiation. The main reason for reducing the lithium interstitial voltage is so more lithium can be accessed for a given experimental overpotential. Alternatively, increasing the lithium interstitial volume by using smaller cations such as Al^{3+}, will increase the intercalation voltage; use of such substitutional cations thus requires the development of novel electrolytes that will not oxidize at high voltages. (iii) Substituting cations should also have stronger oxygen binding in order to improve phase stability during cycling. By suppressing oxygen loss and the formation of high impedance phases, discharge fading can be mitigated, prolonging not only battery life but also energy density.

5.6 Acknowledgement

This work was supported by the Assistant Secretary for Energy Efficiency and Renewable Energy, Office of Vehicle Technologies of the U.S. Department of Energy under Contract No. DE-AC02-05CH11231 under the Batteries for Advanced Transportation Technologies (BATT) Program . This work made use of computational resources provided by the National Energy Research Supercomputer Center (NERSC), which is supported by the Office of Science of the US Department of Energy under Contract DE-AC03-76SF00098. This work also used the Extreme Science and Engineering Discovery Environment (XSEDE), which is supported by National Science Foundation grant number ACI-1053575. I.M.M acknowledges the support of the NSF graduate research fellowship program, and Dr. Kristin Persson for useful discussions and feedback.

Chapter 6

Experimental and Computational Investigation of Lepidocrocite Anodes for Sodium-Ion Batteries

6.1 Foreword

The work presented in this chapter is published by I. M. Markus, S. Engelke, M. Shirpour, M. Asta, M. Doeff in Chemistry of Materials (web) 2016. The authors of this manuscript have granted permission for inclusion in this dissertation.

6.2 Abstract

In this work, we investigated several titanates with lepidocrocite-type structures (general formula $A_xTi_{1-y}M_yO_4$ with A=Na and M=Li or Mg), having potential utility as anode materials for sodium-ion batteries. First principles calculations were used to determine key battery metrics, including potential profiles, structural changes during sodiation, and sodium diffusion energy barriers for several compositions, and compared to experimental results. Site limitations were found to be critical determinants of the gravimetric capacities, which are also affected both by the stacking arrangement of the corrugated layers and the identity of M (Li or Mg). To explain the experimentally observed lattice parameter changes observed as a function of state-of-charge, it was necessary to assume participation of water/solvent during the sodium intercalation process. Sodium diffusion barriers were also found to vary as a function of state-of-charge and diffusion direction, with a spread of 0.06-1.3 eV at low sodium contents, narrowing to 0.3-0.5 eV at higher sodium contents. Based on these results, strategies for selecting and improving the performance of these electrode materials are suggested.

6.3 Introduction

The development of next generation systems for grid-scale energy storage projects remains one of the biggest challenges for both the modernization of the electrical grid and the integration of renewable energy sources such as solar and wind power. One main obstacle for the commercialization of such a technology is the strict cost requirement, with long term goals having to meet the benchmark set by DOE of less than \$250/kWh [19, 174, 175]. The current set of commercial battery technologies, led by high power lithium-ion batteries (LIBs), are not well suited for many of the grid storage applications, such as load leveling. This makes it an imperative to develop a broader portfolio of battery chemistries that can address the needs and scale of each application at an acceptable cost. One of the most attractive options are sodium-ion batteries (NIBs), which in addition to featuring cheap and abundant raw material inputs, offer several synergistic benefits. Among these are the ability to replace the strategic metal Cu with Al as a current collector on the negative electrode side, and the fact that sodium salt solutions are generally more conductive than the lithium analogs, [176] which has important implications for the design of cells. Another advantage of NIBs arises due to the similarity between the manufacturing and processing techniques used for LIBs, requiring less engineering development for large-scale production of such batteries compared to other types of "'Beyond Lithium-Ion"' batteries under consideration.

Currently, among the biggest drawbacks of NIBs is the lack of a suitable negative electrode [177]. While graphite can intercalate lithium and be used as the negative electrode in LIBs, it does not intercalate sodium to a significant degree. Hard carbons may be used as anodes in sodium systems [178], but have low densities and are electroactive close to the sodium plating potential, posing safety concerns. Other candidate anode materials include Sn and Sb alloys, which exhibit rapid capacity losses with prolonged cycling due to large volume expansions during sodiation [179]. An alternative set of materials includes intercalation oxides, with layered titanates offering a rich compositional and structural range of materials that can intercalate sodium [180, 181, 182, 183, 184, 185]. In this work we examine several titanates having lepidocrocite-type structures employing electrochemical testing and first-principles density-functional theory (DFT) calculations. The calculations are used to determine kinetic and thermodynamic limitations of these materials for application as anodes in NIBs. The lepidocrocite titanates are isomorphs of the mineral γ- FeOOH, and have the general formula $A_xTi_{2-y}M_yO4$ where A=K, Rb, Cs; and M = Li, Mg, Co, Fe, Ni, Cu, etc; with additional compounds possible by ion exchanging the A cation with lighter elements such as Na[186, 187, 188, 189, 190, 191]. The structures form as stepped layered materials with a step size of one, with the corrugated layers either arranged in phase with one another or out of phase, corresponding to a shift of half a unit cell in the a direction. Structures with the space group $Cmcm$ (C-type) and $Pmmm$ (P-type), which are relevant to this discussion are shown in Figure 6.1. Although there are several other symmetries possible for lepidocrocite titanates, depending on factors such as the site occupancies in the interlayer spaces, they are not considered here. Previous experimental work on the $A_{0.8}Ti_{1.73}Li_{0.27}O_4$ (A=K, Na) system indicated that both C-type and P-type structures can be produced, depending upon

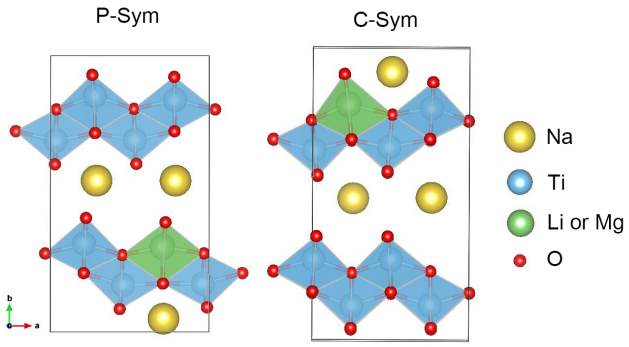

Figure 6.1: Sodium titanium lepidocrocite structure with P-type and C-type symmetry. The blue and green shaded polygons represent edge sharing octahedra for Ti and Li, respectively. The yellow spheres represents some of the possible sodium atoms in the pristine structure.

the identity of A and the thermal treatment, with the highest stable cycling capacities of 150 mAh/g observed for the P-type sodiated version in unoptimized sodium half cells[184, 192]. Cell performance for these systems was highly dependent on details of the electrode and materials fabrication, such as the type of binder used and post-processing steps such as carbon coating.

In the current work we employ first-principles DFT calculations with the aim of decoupling cell-engineering effects from fundamental materials properties. The first-principles calculations performed were for the materials having idealized stoichiometries of $Na_{0.75}Ti_{1.75}Li_{0.25}O_4$ for C-type and P-type phases, close to that of experimentally achieved samples; and for $Na_{1.0}Ti_{1.5}Mg_{0.5}O_4$ and $Na_{0.75}Ti_{1.625}Mg_{0.375}O_4$ having P-type symmetry, which also can be synthesized in the laboratory. Additionally, $Na_{0.75}Ti_{1.75}Mg_{0.25}O_4$ was investigated in order to enable a direct comparison of Li and Mg containing compounds with otherwise identical compositions, even though the latter has not been synthesized experimentally.

The stoichiometries listed above were selected based on proximity to the ones achieved experimentally considering computational resource limitations to avoid the need for prohibitively large supercells. Simulations specifically modeled structural changes during sodiation to understand their unusually low intercalation potentials, taking into consideration the presence of interstitial water. We also present computational and experimental results for the previously mentioned Mg-containing structures in order to explore the potential applicability of other compositions with lepidocrocite structures in sodium ion batteries. The results from the latter materials compounds represent, to the best of our knowledge, the first measurements related to the performance of these materials for battery applications. The results thus provide a more comprehensive understanding of the limitations of lepidocrocite-type compounds for NIBs without complications from cell engineering effects. From these results we present design recommendations for future candidate materials for applications in NIBs.

6.4 Methods

DFT Simulations

First-principles calculations were performed using the Vienna *ab initio* simulation package (VASP), employing the Generalized Gradient Approximation (GGA) due to Perdew, Burke, and Ernzerhof (PBE). [193] The simulations were carried out using the projector augmented wave (PAW) method [194, 195], as implemented in the VASP code [194, 196]. Specifically we made use of the PBE PAW potentials Na with one valence electron ($3s^1$), O with 6 valence electrons ($2s^2 2p^4$), Ti with 4 valence electrons ($3d^3 4s^1$), Li with one valence electron ($2s^1$), and Mg with two valence electrons ($3s^2$). DFT calculations made use of supercells composed of four unit cells with a plane wave energy cutoff of 500 eV, and a Γ centered k-point grid of 3x2x4. In these calculations the energy was converged to 10^{-6} eV in the self-consistent charge-density solutions, and the Hellman-Feynman forces on the ions were converged to 10 meV/Å in the structural relaxations. Calculations were spin polarized to account for the local moment of Ti^{+3} ions that form when sodium is intercalated. Additionally, the calculations employed corrections for van der Waals interactions, as well as Hubbard-U corrections for the Ti cation *d* electrons. These corrections were included after finding that they were needed to stabilize the C type symmetry at higher sodium contents, consistent with experimental findings. The van der Waals correction employed was the so-called DFT-D2 method due to Grimme as implemented in VASP. [197] Hubbard-U corrections were included employing the method of Dudarev *et al.* [44], with a value of U-J=4.0 eV for Ti *d* electrons, based on literature values reported for other layered titanates. [198] Calculations of electrochemical potentials were performed utilizing standard methods described in the literature [199, 179]. To calculate the diffusion energy barriers the climbing-image nudge elastic band (CI-NEB) method was used. [200, 201, 202, 81, 203] In the CI-NEB calculations, initial and final configurations were selected from sampling sodium positions at different interstitial sites in the structure. The minimum energy paths were calculated from linear interpolation of initial and final position using at least 5 images.

Material Synthesis

The anode materials $Na_{0.7}Ti_{1.65}Mg_{0.40}O_4$, $Na_{0.9}Ti_{1.55}Mg_{0.45}O_4$ and $Na_{0.8}Ti_{1.73}Li_{0.27}O_4$ were synthesized using the solid state method by Shirpour *et al.* [184]. $K_{0.7}Ti_{1.65}Mg_{0.35}O_4$, $K_{0.9}Ti_{1.55}Mg_{0.45}O_4$ and $K_{0.8}Ti_{1.73}Li_{0.27}O_4$ were prepared via the solid state reaction of MgO (purity min. 95.0%, Alfa Aesar), K_2CO_3 (purity 99.0%, Sigma-Aldrich), TiO_2 (anatase, purity 99.7%,<25 nm, Sigma-Aldrich), and Li_2CO_3 (purity 99+%, Aldrich). First, stoichiometric mixtures of the precursors were mixed in a mortar for 5 min. The mixtures were calcined in an alumina crucible at 1000^o C for 21 h in a Thermo Scientific Lindberg Blue M oven. The synthesized powder was first milled in a mortar for five minutes and the obtained phases were confirmed through X-ray powder diffraction (XRD) spectra on a Bruker X-ray Diffractometer (XRD, D2-Phaser). The materials were ranked based on crystallinity, as seen

by sharp peaks for the lower angles, and the most suitable materials were milled in a planetary mill with 10 zirconia balls, each 0.5 cm diameter, at 300 rpm for 2 hours in acetone. The jar was opened after milling, the balls were removed, and the acetone was evaporated in air. The powder was collected and ground in a mortar. A 4.0 M NaCl solution was prepared and the products were each ion exchanged by stirring the powders in the solution in 200 ml flasks at 80^o C for 8 days. The resulting materials were washed with plain water to remove the salt, air dried, then dried in an oven at 50^o C and dried in a vacuum oven overnight.

Electrochemical Testing

The electrochemical properties of the compounds were evaluated in two-electrode 2032 coin cells containing metallic sodium foils as negative electrodes (half-cells). For this, bulk dry sodium (Sigma Aldrich) was extruded into thin foils and cut to size to make sodium anodes for these cells. For the positive electrodes, active material and acetylene black were first mixed together for 2 hours at 300 rpm in a planetary mill. Composite working electrodes were prepared by making a slurry containing 70 wt% of the active material, 20−25 wt% acetylene black (Denka, 50% compressed), and 5−10 wt% polyvinylidene difluoride (PVDF) (99.5+%, Aldrich) binder in N-methyl-2-pyrrolidinone (NMP). The slurry was cast onto carbon coated aluminum foil (Exopack Advanced Coatings). The electrodes were dried first in air and then under vacuum at 120^o C for 12 hours before being cut to size and weighed in a helium filled glovebox. The typical loading and thickness were 5 mg/cm^2 and 60 μm, respectively. The electrolyte used was a solution of 1 M $NaPF_6$ (Sigma Aldrich) in ethylene carbonate/ dimethyl carbonate (EC:DMC; 3:7 mol, from Novolyte Technologies) made in house, and one or two Celgard 3401 separators were used in the coin cells. Galvanostatic cycling experiments at room temperature were carried out with a Bio-logic VMP3 potentiostat/galvanostat.

6.5 Results and Discussion

Prior to performing DFT calculations, the possible specific capacities for different lepidocrocite structures were calculated based solely on compositional and structural considerations. Figure 6.2 shows the relationship between composition and theoretical specific capacity for the $A_xTi_{1-y}M_yO_4$ system where M = Li^+ or Mg^{2+} and A is Li^+, Na^+ or K^+. Two scenarios are presented, one in which capacity is limited by the number of reducible Ti ions, and the other where the limitation is the number of sites available for ion insertion. (Note that not every composition shown on this graph can be synthesized; the intent is primarily to show how composition affects capacity). The site-limited case is relevant to insertion of sodium ions into the structure, because of their relatively large size. Higher capacities might be expected in the case of lithium intercalation, where A = Li^+, because of the smaller size of these ions, although it is still unlikely that the upper limit determined by the amount of reducible titanium can be achieved. From this graph, it is obvious that it is generally desirable to maximize titanium content (minimize y) and, to a lesser extent,

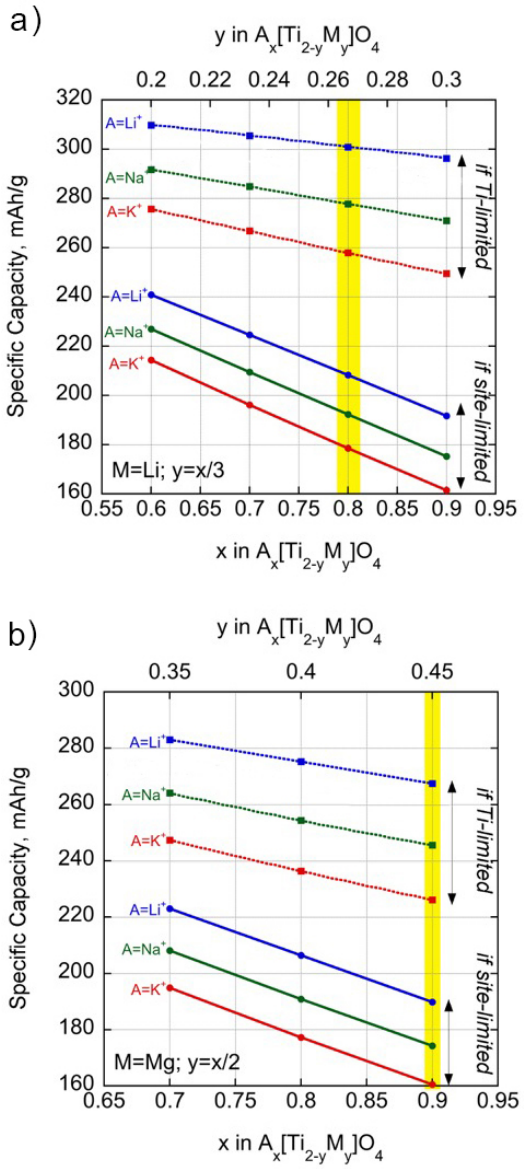

Figure 6.2: Theoretical calculation of gravimetric capacity for a) lithium and b) magnesium containing lepidocrocite structures with different initial stoichiometries considering situations limited by the number of Ti ions or by the number of available sites for sodium intercalation. The highlighted regions corresponds to experimentally achieved stoichiometries.

choose lighter cations for A, no matter what the limitation. Similar considerations apply for other compositions (e.g., when M = Mg^{2+} and y=x/2). In practice, choices of materials are limited by the solid-solution behavior of the systems.

First-principles calculations were thus employed to provide an understanding of different experimental observations reported in the literature for distinct lepidocrocite-like com-

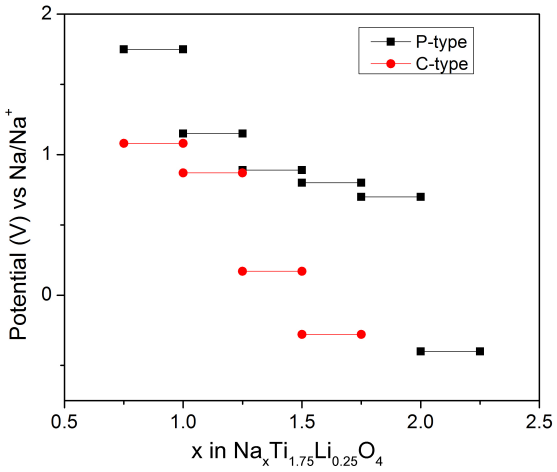

Figure 6.3: Calculated intercalation potential for P-type (black lines) and C-type (red lines) $Na_{0.75}Ti_{1.75}Li_{0.25}O_4$.

pounds. Experimental results for $A_{0.8}Ti_{1.73}Li_{0.27}O_4$ (A=K, Na) electrodes have shown that the P-type materials generally deliver higher practical capacities than C-type, regardless of whether A = Na^+ or K^+ [184, 192]. In order to understand the underlying reasons for the capacity difference we performed structural optimizations and total-energy calculations for $Na_{0.75}Ti_{1.75}Li_{0.25}O_4$ having both P-type and C-type arrangements, and calculated the potential profiles for both types of structures. As shown in Fig. 6.3, the P-type symmetry is calculated to have a higher intercalation potential and capacity than the C-type structure, with an additional 0.25-0.50 mols of Na per formula unit, or approximately 40-80 mAh/g, expected for the P-type structure. These results confirm that neither P-type or C-type can reach the maximum specific capacity based on reduction of all the Ti. However, the results also indicate that only the P-type structure can approach the theoretical values for site limitations shown in Figure 6.2a, because the C-type structure becomes less stable at higher sodium contents due to higher electrostatic repulsions between intercalated sodium ions.

Further analysis of the calculated results indicate a deviation from the experimental lattice parameters obtained during sodiation, as well as the predicted specific capacities. For an anhydrous P-type structure our calculations underestimate volume expansion by approximately 9% and overestimate the capacity by 37% (192 mAh/g vs 140 mAh/g). This discrepancy can be attributed to the model structure used in these calculations, which ignored complications from a cooperative solvent co-insertion mechanism observed by Shirpour *et al.* [184] Evidence from ex-situ X-ray diffraction experiments performed on P-type $Na_{0.8}Ti_{1.73}Li_{0.27}O_4$ indicated that neutral species (water or solvent) were de-inserted concomitant with sodium intercalation during discharge, with the reverse process occurring during charge. For the portion of the electrode that was anhydrous, there was an expansion along the *b* lattice parameter during sodiation, with additional expansion occurring during the desodiation. The fully sodiated products of both the hydrated and anhydrous portion of the electrodes were

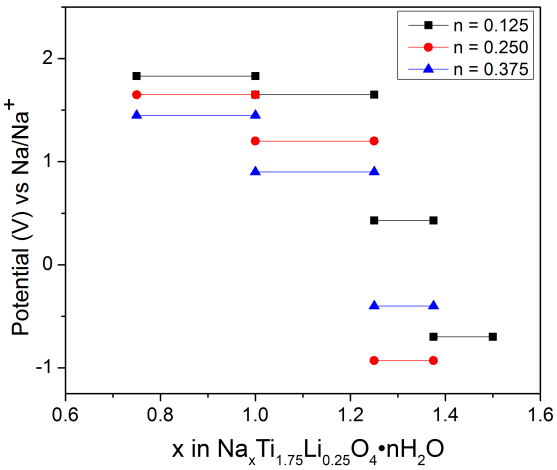

Figure 6.4: Calculated intercalation potential for P-type $Na_{0.75}Ti_{1.75}Li_{0.25}O_4$n H_2O , where n=0.125-0.375.

identical.

To investigate the impact of interstitial water on capacity and structural changes we further refined our calculations by modeling the P-type structure including interstitial water according to $Na_{0.75}Ti_{1.75}Li_{0.25}O_4 \bullet nH_2O$ with n ranging from 0.125-1.25 mols. The results shown in Figure 6.4, indicate that the predicted capacity of the material decreases with increasing solvent content, as there are fewer electrostatically stable sites for sodium insertion. However, this is only true if the neutral species are not displaced by sodium during discharge. The cooperative displacement mechanism is unlikely to be completely efficient, presenting one possibility for the discrepancies found between the experimental and computational results for the capacity, because theoretically this material should be able to accommodate more sodium intercalation than is observed in the actual half-cell experiments.

Further evidence that the material is susceptible to a cooperative solvent uptake is obtained by analyzing the changes to the lattice parameters during sodiation. Figure 6.5a, shows the changes to the *b* lattice parameter during sodiation for P-type lepidocrocite titanates with water content ranging from n = 0 to 0.375 mols per formula unit. As can be seen the b lattice parameter contracts during sodium insertion, following similar behavior to the experimental results for the solvated samples. For comparison, the *b* lattice parameter is also plotted in Fig. 6.5b for the same P-type lepidocrocite given a fixed sodium concentration with increasing water content from n = 0 to 1.25 mols per formula unit. The results shows a steady increase in the lattice parameter upon desodiation similar to that found experimentally for the dehydrated sample. These results support the conclusion that sodium ions and solvent molecules interchange during cycling. In the previous work by Shirpour *et al.* [184] interlayer charge density was established as an important parameter for predicting such behavior, and given that the results obtained herein are consistent, future material selection and testing should consider this susceptibility to solvent uptake as a possible reason

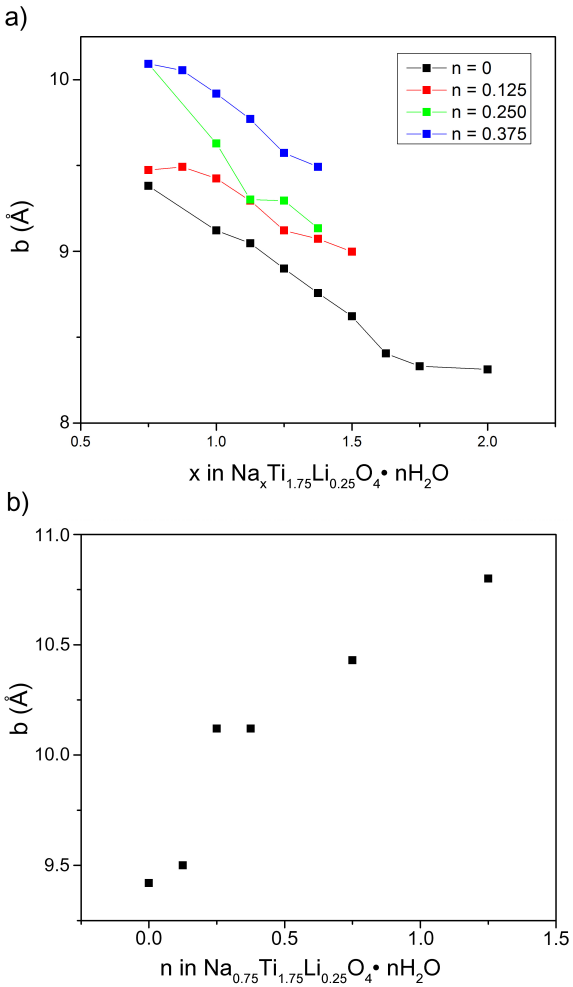

Figure 6.5: Shows the computationally derived change in the b lattice parameters with increasing sodium concentration for the P-type lepidocrocite with water content ranging from 0-0.375. b) shows the change in the b lattice parameter for $Na_{0.75}Ti_{1.75}Li_{0.25}O_4 \bullet nH_2O$ with water content increasing from n= 0 to n= 1.5.

for materials failing to deliver their theoretical capacities.

In order to further understand the sodium intercalation mechanism in lepidocrocite-type titanates, DFT calculations and experiments were performed with Mg containing structures. Calculations were performed on the compounds $Na_{0.75}Ti_{1.625}Mg_{0.375}O_4$, $Na_{1.0}Ti_{1.50}Mg_{0.50}O_4$, and a hypothetical composition of $Na_{0.75}Ti_{1.75}Mg_{0.25}O_4$ with P-type structures. The latter material was selected to be able to directly compare results with the Li containing analog discussed above, although it cannot be prepared directly by solid-state synthesis methods. [188] Results for the intercalation potential of each structure are shown in Fig. 6.6, with the $Na_{0.75}Ti_{1.625}Mg_{0.375}O_4$ stoichiometry predicted to have the highest capacity of the three

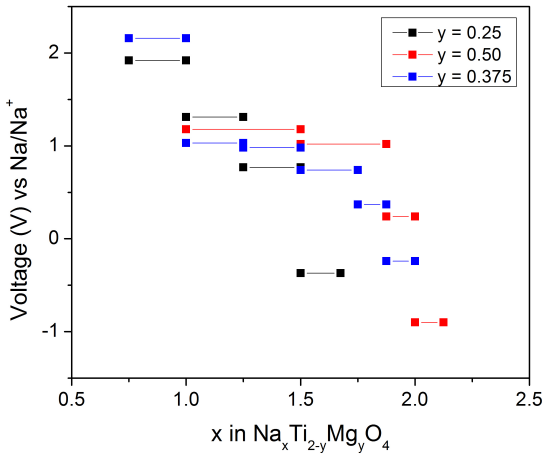

Figure 6.6: Calculated intercalation potential for P-type compounds $Na_{0.75}Ti_{1.75}Mg_{0.25}O_4$ (black lines), $Na_{0.75}Ti_{1.625}Mg_{0.375}O_4$ (blue lines) and $Na_{1.0}Ti_{1.5}Mg_{0.5}O_4$ (red lines).

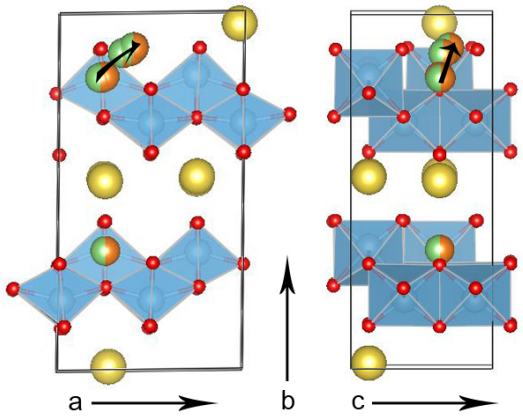

Figure 6.7: Lithium or magnesium diffusion minimum energy path for diffusion from Ti site to sodium site.

compositions examined. All of the Mg-containing structures have lower predicted capacities than those determined for the P-type Li containing compound. By calculating the structural changes for both lithium and magnesium containing compounds with the same stoichiometry, we found that at higher sodium contents, the lithium is predicted to drop from octahedral positions in the metal oxide layer into adjacent tetrahedral positions. An analogous process is not predicted to occur for the magnesium containing compound (i.e., Mg is predicted to be less mobile). Employing nudge elastic band calculations we found that lithium has a 0.29 eV energy barrier to jump from the titanium 4c site to a vacant sodium 8a site in the C-type lepidocrocite (figure 6.7), while in the P-type structure lithium had an energy barrier of 0.42 eV and magnesium had an energy barrier of 0.71 eV. Because the lithium

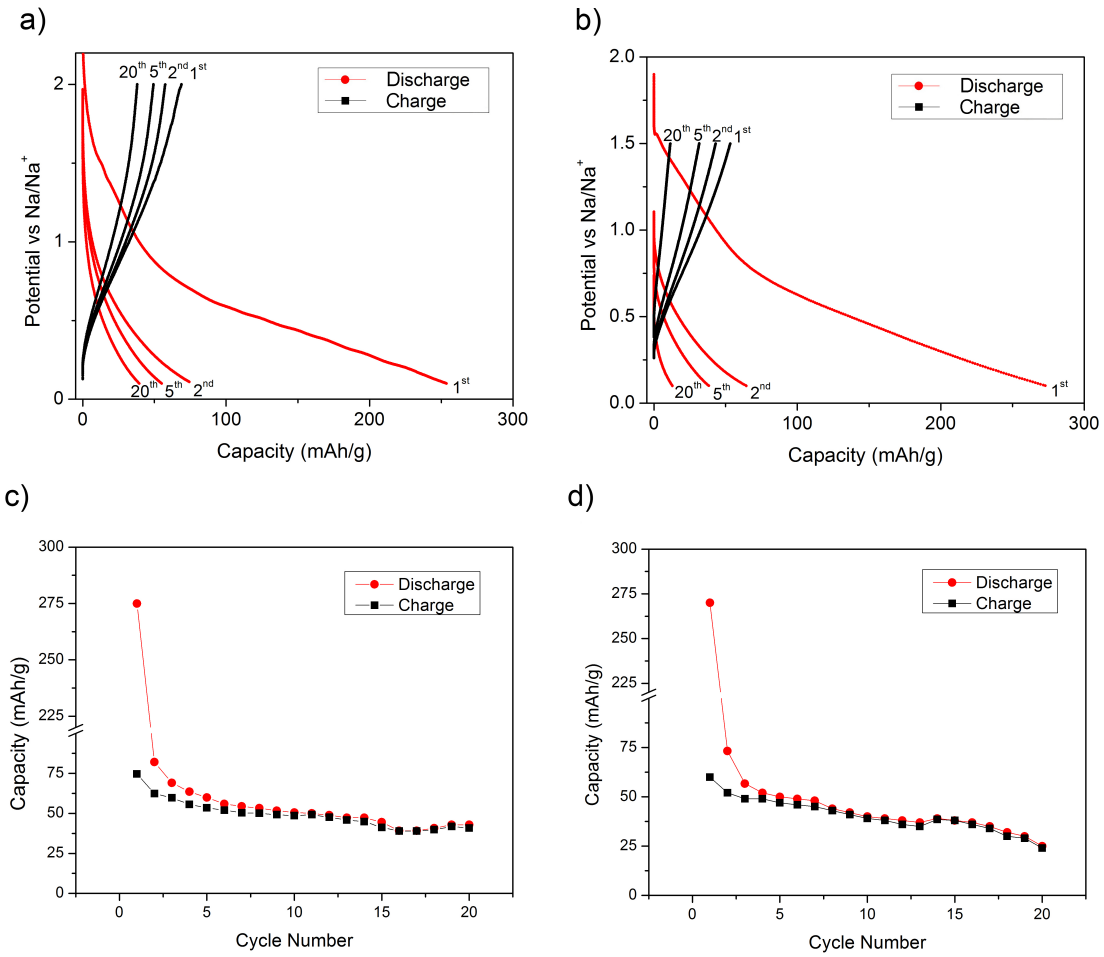

Figure 6.8: a,b) Show select discharge and charge capacity curves for (a) $Na_{0.7}Ti_{1.45}Mg_{0.35}O_4$ and (b) $Na_{0.9}Ti_{1.55}Mg_{0.45}O_4$. Parts c,d) show the discharge and charge capacity for (c) $Na_{0.7}Ti_{1.45}Mg_{0.35}O_4$ and (d) $Na_{0.9}Ti_{1.55}Mg_{0.45}O_4$ for 20 cycles. The cells were cycled in Na half cells between 2.5 and 0.1 V at 0.06 to 0.08 mA cm^{-2} (20 mAg^{-1})

ions have energy barriers comparable to those calculated for intercalating sodium, it is likely they can diffuse out of their sites in the transition metal layer during either the ion exchange process or the sodiation process that occurs upon cycling. From a practical perspective, the differences in energy barriers suggest that the greater lithium mobility can facilitate higher sodium insertion by enabling Li to leave its initial site in the host structure during discharge, thus reducing internal stress and electrostatic interactions between sodium.

The lower capacity predicted for magnesium substituted materials was verified experimentally by synthesizing two different compositions, $Na_{0.9}Ti_{1.55}Mg_{0.45}O_4$ and $Na_{0.7}Ti_{1.65}Mg_{0.35}O_4$, and testing them in a Na half cell. The XRD patterns for the two compositions are shown in Fig. 6.9; the results are consistent with nearly phase-pure lepidocrocite structures, with

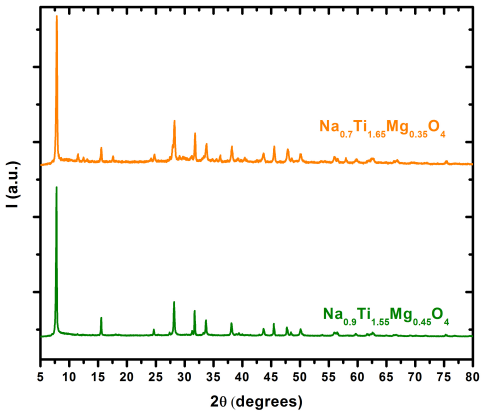

Figure 6.9: XRD pattern for $Na_{0.9}Ti_{1.55}Mg_{0.45}O_4$ and $Na_{0.7}Ti_{1.65}Mg_{0.35}O_4$

small traces of impurities arising from the ion-exchange process. Fig. 6.8 shows electrochemical cycling data for both compositions. With the exception of the first cycle discharge capacity, both tested compositions achieved lower capacities than those previously reported by Shirpour *et al.* [184] for the Li containing lepidocrocite titanate. Due to the low potentials at which these compounds discharge, side reactions due to irreversible reduction of electrolyte and formation of a solid electrolyte interface (SEI) contribute capacity to the first discharge. The second discharge is therefore a more accurate reflection of the true capacities of these materials. Given that the material synthesis, cell fabrication, and testing were comparable for the two types of materials, this verifies the information presented in Figure 6.6, that the Mg-containing titanates will have lower capacities than the Li-containing one. This is significant particularly for the $Na_{0.7}Ti_{1.65}Mg_{0.35}O_4$ composition, because the titanium content is nearly the same as that of $Na_{0.8}Ti_{1.73}Li_{0.27}O_4$ and there should be fewer site limitations due to the lower sodium content in the pristine material.

Lastly, we examined the energy barriers for sodium diffusion in the P-type and C-type structures containing lithium and the P-type structure containing Mg with the stoichiometry $Na_{0.75}Ti_{1.75}Mg_{0.25}O_4$. Energy barriers were calculated parallel to the corrugation along the a lattice direction and perpendicular to the corrugations along the c direction for the different configurations available at each sodium concentration. Fig. 6.10b shows that the P-type and C-type structures exhibit slightly different behaviors that translate to different cycling properties. The calculated values for different sodium concentrations in the P-type structure reveal a wide spread at lower concentrations that narrows with increasing sodium content. The results suggest that there is a strong correlation for sodium diffusion with electrostatic repulsion from other sodium cations, since the larger energy barriers are generated when there are non-diffusing sodium cations nearby. This implies that the P-type materials have strong kinetic dependences on the state-of-charge, regardless of the identity of the substituent (Li

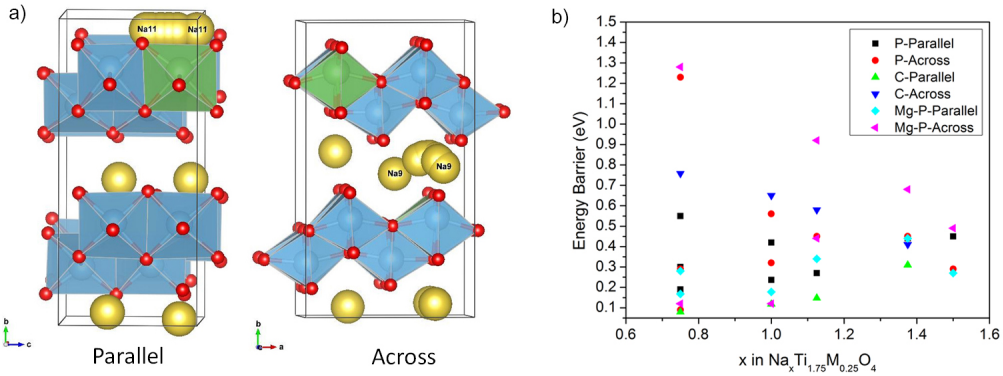

Figure 6.10: a) Shows the two types of minimum energy paths consider for sodium diffusion, parallel refers to sodium movement along corrugation in the c direction, and across refers to sodium diffusion perpendicular to corrugation along the a direction. b) Shows the energy barriers for sodium diffusion at different sodium concentration for the the P-type and C-type lithium substituted phases, and the P-type magnesium substituted phase.

or Mg). Furthermore, analysis of the spread of energy barriers for each phase reveals possible dependence on the charge/discharge rates. For the P-type material, the availability of more interstitial sites with different local electrostatic environments results in a broader spread of diffusion paths for either across or parallel jump types. Because the low energy barrier paths are only accessible when the sodium ions are spread out more homogeneously, fast current rates can result in the formation of local concentration gradients that force sodium to diffuse across higher energy paths. Evidence supporting this hypothesis is provided in Figure 6.11, which shows electrochemical cycling of Na half cells with the material $Na_{0.8}Ti_{1.73}Li0.27O_4$ employing different current rates. This material was synthesized and tested previously by Shirpour *et al.* [184]. The data indicates that cells cycled with currents rates of 0.2 mA/cm^2 (67.5 mA/g) deliver less than half the capacity than cells with 0.04 mA/cm^2 (13.5 mA/g). The slower current rate allows the material to deliver initial higher capacities that permit a higher number cycles before delivering equal discharge capacities.

In these structures as the sodium content increases and the material becomes more electrostatically homogenous, there is less variance in the energy barriers with the direction, with an average value of 0.4 eV predicted for these materials when standard electrode slurries are used to fabricate cells. However, the lowest energy barriers were available for parallel diffusion when there were no other sodium ions nearby suggesting that the material would exhibit anisotropic conduction similar to 1D diffusion materials. This is predicted to be the case for the C-type structure, which as can be seen in Fig. 6.10b does not have the spread in energy barriers that the P-type material does. Because this material has fewer symmetrically distinct sites for Na intercalation, its diffusion paths are more clearly defined with noticeable anisotropic behavior. The bright green and dark blue triangles indicate diffusion barriers that are parallel or across the corrugation, respectively. As can be seen the barriers follow

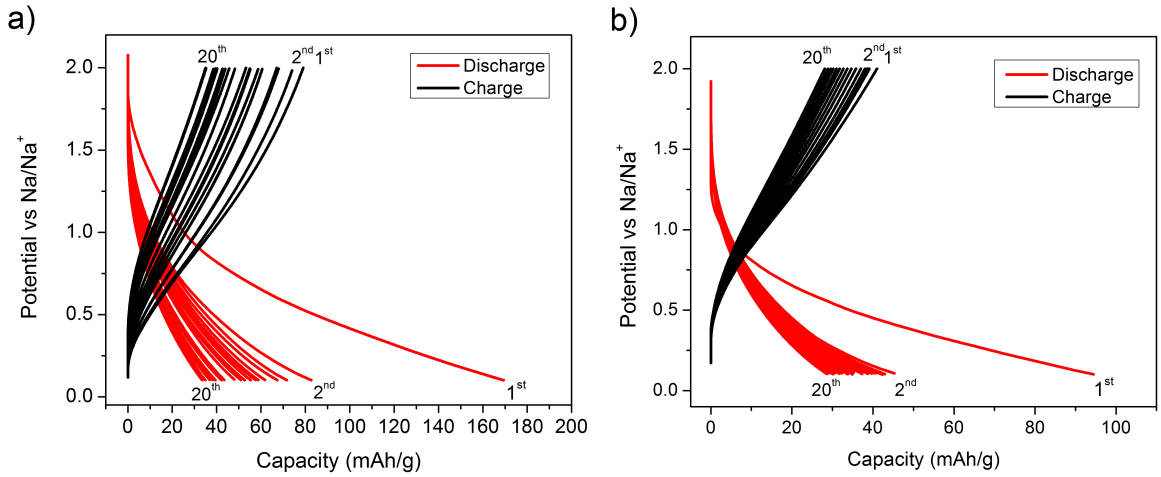

Figure 6.11: Specific capacity for $Na_{0.8}Ti_{1.73}Li_{0.27}O_4$ Na half cells with currents rates of (a) 0.04 mA/cm^2 and (b) 0.2 mA/cm^2 .

almost linear behavior with the sodium content, suggesting state-of-charge is also important for this phase. However, from these results it appears that fast 1-dimensional diffusion is possible parallel to the corrugations, with energy barriers ranging from 0.06 to 0.3 eV. This suggest that this phase could have superior rate capability to the P-type structures. Evidence for this finding has been reported by Chen et. al [192], who found that in the C-type material $K_{0.8}Ti_{1.73}Li_{0.27}O_4$ that has been ball milled and carbon coated, the capacity decreases from 110 mAh/g to 60 mAh/g when increasing the current from 20 mA/g to 200 mA/g, with full capacity recovery when current is decreased back to 20 mA/g. Superior performance is also reported in work by Katogi et al. [204], which shows that the C-centered lepidocrocite $Na_{0.9}Ti_{1.7}Li_{0.3}O_4$ has excellent rate capability, with over 80% capacity retention when increasing the current from C/17.5 to 10C.

The combined computational and experimental results indicate that future work on lepidocrocite type materials need to consider application requirements. Although Li substituted P-type structures are predicted to have higher capacities, it is the C-type materials that are expected to have good rate capabilities. Taking advantage of potentially fast 1-dimensional diffusion requires that particle size be optimized in order to limit kinetic effects because any blockage of diffusion channels could severely impact performance or rate capability for these materials. Furthermore, given that site limitations create an upper boundary for the amount of sodium that can be intercalated, different strategies such as aliovalent ion substitution or interlayer spacing engineering, should be consider to increase the practical capacity of these materials.

6.6 Conclusions

Using first-principles calculations coupled with experimental measurements, we have explored several properties of the lepidocrocite-structured titanates as a function of composition and stacking arrangement. Intercalation potential calculations revealed that the capacities of these materials are limited by site limitations and electrostatic considerations rather than the number of redox active centers. Based on structural considerations, the highest practical capacity should be achieved for the P-type $Na_{0.75}Ti_{1.75}Li_{0.25}O_4$ material, corresponding to insertion of $\sim$1.25 mols of sodium per formula unit. When effects from interstitial water are included, it appears that practical capacity is decreased due to solvent uptake. This reduces site availability for sodium intercalation in the experimental setup. A positive effect previously observed and corroborated by structural relaxation calculations was that this solvent-exchange mechanism is likely cooperative, reducing overall volume changes during cycling as lattice contraction along the b direction is ameliorated by concomitant solvent insertion.

A comparison between materials containing Li and Mg in the transition metal layers indicates that the former should have superior capacity because of the mobility of lithium ions, which can move out of the transition metal sites into sodium sites and relax strain. Calculations of the energy barriers for sodium diffusion indicate that the P-type structures can be rate-limited due to strong electrostatic interactions between intercalated sodium ions. The calculated energy barriers ranged from 0.1 eV to 1.3 eV before sodium intercalation and narrowed to 0.3 eV to 0.5 eV after 0.75 mols/f.u. of sodium had been intercalated. However, lower energy barriers (0.06 to 0.3 eV) were predicted for the C-type structure, with possible fast diffusion along channels parallel to the corrugations that would result in rate capability superior to that of the P-type structure. The combined findings suggest that these materials can benefit from smaller particle sizes that can facilitate diffusion along fast channels that can reduce large concentration gradients and make fully accessible fast 1D pathways.

6.7 Acknowledgment

This work was supported by the Assistant Secretary for Energy Efficiency and Renewable Energy, Office of Vehicle Technologies of the U.S. Department of Energy under contract no. DE-AC02-05CH11231. This work made use of computational resources provided by the Extreme Science and Engineering Discovery Environment (XSEDE), which is supported by National Science Foundation under grant number ACI-1053575. I.M.M acknowledges the support of the NSF graduate research fellowship program. S.E. would like to thank Dr. Kristin Persson for financial and research support.

Chapter 7

Investigation of Electrolyte Concentration Effects on the Performance of Lithium-Oxygen Batteries

7.1 Foreword

The work presented in this chapter was published by I. M. Markus, G. Jones, J. Garcia, in the Journal of Physical Chemistry C, vol. 120, issue 11, pages 5949-5957 (2016), and is reproduced here with the permission of co-authors and publishers (American Chemical Society).

7.2 Abstract

A combined experimental and computational study has been performed in order to elucidate the effect of electrolyte salt concentration on the performance of Li-O_2 batteries. Four electrolyte solutions with varying lithium triflimide (LiTFSI) content in 1,2-dimethoxyethane (DME) were studied to identify principal failure mechanisms in Li-O_2 batteries for dilute and concentrated electrolytes (0.1 M to saturation) in cells cycled with high overpotentials and/or deep discharge. Quantitative ^{19}F NMR was employed to determine that in 0.1 M electrolyte solutions, salt decomposition can contribute to limitations in cell recycling arising from low ionic conductivity due to a decrease in available soluble Li^+ over multiple cycles. In contrast, increased salt decomposition in high-concentration electrolytes can result in cathode passivation by insoluble Li salts that impact capacity by hindering Li_2O_2 production and further inhibiting electronic conductivity. By employing first principles calculations we modeled different pathways for the decomposition of the TFSI anion, and found that it was particularly susceptible to decomposition in its neutral state, for example if H^+ is present and

bound to the TFSI anion. The cumulative results suggest that employing low-concentration electrolytes with more stable lithium salts are ideal for better cell performance.

7.3 Introduction

The lithium-oxygen chemistry remains one of the most promising next generation battery systems for electric vehicles. With the advent of lithium-ion batteries (LIBs) several electric vehicles have been commercialized, however, as LIBs approach their theoretical limits for energy density, new technologies are required to both reduce the cost and improve the range of these automobiles. One of the most crucial challenges is the design of new stable electrolyte compositions, that can withstand both anode and cathode chemistries. Part of the significance of furthering research into electrolyte stability, is the benefit on being applicable to both current LIB technologies as well as beyond lithium-ion battery chemistries that employ lithium. Although the high theoretical capacity of Li-O_2 batteries might not be achievable given the passivating properties of the discharge product, Li_2O_2, theoretical Li-O_2 batteries are projected to have energy densities in the range of 500-900 Wh/Kg , which is twice the maximum values achievable for LIBs. [205] The potential of this chemistry to exceed what is possible with current technologies warrants further work to understand shortcomings of currently available materials. This is required to not just further optimize their performance but provide pathways for future material discovery and development that can serve to commercialize this technology. Among the problems faced by Li-O_2 batteries are poor rate capabilities, high charging over-potentials, [206, 207] electrolyte and electrode decomposition, [208, 209] and safety hazards resulting from dendrite formation. [33] Many of these challenges arise from material limitations that result in sluggish kinetics that in turn create overpotentials that open the possibility for parasitic reactions that reduce overall cell efficiency. [205, 32]

Among the best-performing electrolyte combinations is the solvent 1,2-dimethoxyethane (DME) with 1.0 M LiTFSI ($LiN(CF_3SO_2)_2$), which without the addition of additives or catalyst has a first discharge electron per oxygen molecule (e^-/O_2) ratio of 2.01, and first cycle oxygen reduction to oxygen evolution ratio (OER/ORR) of 0.81.[31, 32] For this electrolyte one of the recently identified contributors for cell inefficiency is the solvent decomposition through a Dakin oxidation mechanism. This pathway depends on a Li-ion-facilitated abstraction of H^+ from a DME molecule in the rate determining step (RDS) to initiate its breakdown into lithium formate and lithium acetate.[209, 210] This implies that the kinetics of decomposition is reliant on Li-ion concentration and thus, it has been postulated that reducing the Li^+ concentration in the electrolyte should minimize DME decomposition chemistry (as long as the ion concentration remains sufficient for battery operation). However, studies of salt concentration in electrolytes in other battery chemistries have demonstrated that high salt concentration can help reduce the reactivity between the electrolyte and electrodes during cell operations, including improved stability with lithium metal and graphite. [211, 212, 213, 214, 215] From molecular dynamics simulations it is suggested that changes to the

solvation shell around cations in the electrolyte can help reduce their overall reactivity, thus stabilizing the electrolyte. Recent studies have also shown that for the Li-O_2 chemistry this solvation shell is critical for battery performance [216], with proper anion selection aiding solvent stability.[217, 218, 219]

In this work we investigate if the ultra concentration effects observed in other chemistries can be applied to Li-O_2 batteries. We have performed a systematic study examining four concentrations of the electrolyte mixture DME + LiTFSI ranging from 0.1 M to saturation ($\sim$2.6 M) in an effort to not just optimize battery performance in the context of the previously mentioned challenges, but also to better understand fundamental differences that exist between Li-O_2 batteries and other lithium-based chemistries. By employing previously demonstrated spectroscopy and analysis tools we highlight the mechanism by which salt concentrations impact battery performance, identifying two separate modes of failure for dilute and saturated electrolytes. Furthermore, in an effort to understand how salt decomposition occurs we utilize first principles calculations to examine two reaction pathways for the LiTFSI decomposition for the production of compounds detected through ^{19}F NMR analysis. The results from our investigation shed further evidence for the need of new strategies toward stabilizing the electrochemistry of Li-O_2 batteries, with strong support that common salts and solvents used in other lithium based batteries are not compatible with the strong oxidizing presence of Li_2O_2.

7.4 Methodology

Cell Components

AvCarb® P50 was utilized as the cathode for all cells by punching out 12mm disks and rinsing each disk 3 times with DME to wash away any loose carbon. To improve electronic conductivity stainless steel (SS) mesh was also punched out to act as a current collector for the cathode. The SS mesh was cleaned with acetone and DME to remove any organic compounds that might have remained from manufacturing. The 0.1 M, 1.0 M, and 2.0 M electrolytes were prepared by dissolving stochiometric amount of lithium bis(trifluoromethane sulfonyl)imide (LiTFSI) in 1,2 dimethoxyethane (DME). The saturated electrolyte was prepared by adding excess LiTFSI to DME and stirring overnight, followed by decantation and filtration of the liquid part of the mixture. The concentration was then determined by taking 1.0 mL of the electrolyte solution and evaporating off the solvent and massing the dried material.

Electrochemical Measurement

All electrochemical measurements were carried out at room temperature on an in-house designed differential electrochemical mass spectrometry (DEMS) system described in detail previously. [220, 221] A VMP3 BioLogic multi-channel potentiostat was used for all electro-

chemical characterization. Hermetic electrochemical cells, based loosely on a Swagelok®-type battery cell, are designed to seal by compressing o-rings against a quartz-tube that houses all cell contents. Cells were assembled in an argon glove box with <0.1 ppm water and oxygen content. 11-mm diameter lithium discs were punched from an as-received 250 μm thick lithium foil (Lectro® Max100 from FMC) and used as anodes for all the cells in this study, with Celgard® 2500 utilized as the separator. All cells employed 65.0 μL of the respective electrolyte solution. A 1.0 mm in height stainless steel ring is used to incorporate a headspace above the cathode. Capillaries soldered into the cathode side of the cell allow gases to be swept through the cell. For the full cycle experiments the discharge step was performed under constant volume, measuring the pressure decay. Discharge experiments that were performed until cells experienced sudden voltage drop were performed under the constant pressure of approximately 1140 torr. For the later two sets of experiments at least 2 measurements were performed for each electrolyte concentration. Electrochemical impedance spectroscopy of the cells was evaluated using an AC impedance analyzer over a frequency range of 10^6 Hz to 10^1 Hz for interface investigation of the electrodes in cells before and after each charge and discharge cycle.

Scanning Electron Microscopy

The cathodes from cycled or discharged cells were removed from cell body inside an argon glove box (<0.1 ppm H_2O and O_2) and placed in a glass vial. The cathodes were rinsed three times with DME to wash off the electrolyte salt and the residual solvent was evaporated. The dried cathodes were mounted on an SEM sample holder and taken to the SEM sample loading chamber (connected to the SEM) in a sealed glass container. The sample holder is then transferred to the sample loading chamber and the latter is then pumped out before transferring the sample holder for imaging in the SEM. The time from opening the container to the commencement of loading chamber pump down is <5 seconds. Exposure to high vacuum can result in the evaporation of decomposition products including any organic peroxides. The measurements were performed on an FEI Helios Nanolab 400s system. EDX analysis and mapping was performed using a Bruker Xflash 5030 SDD detector at 5.0 kV and 0.69 nA beam current.

NMR Analysis

Cathodes were removed from cell body inside an argon glove box (<0.1 ppm H_2O and O_2) and placed in a glass vial that was hermetically sealed with a septa cap. The samples was quenched by injection of 1.0 mL of D_2O at room temperature into the vial under Ar and then transferred to NMR tubes for ^1H and ^{19}F NMR analysis. To have a standard internal reference, 2.0 μL of benzene or hexafluorobenzene were added.

Computational Methodology

All calculations were performed with the GAMESS-US [222] computational chemistry package. Geometry optimizations were performed with the dispersion-corrected B3LYP-D3 density functional method [50, 51, 52] with the 6-311+G(2d,p) basis set [48, 47, 49]. All reactions were performed with the IEF-PCM method in DCM solvent (ϵ=8.93)[223] as a representative of DME (ϵ=7.2). Only vibrational free energy corrections to the electronic energy at the experimental temperature (298 K) were used in accordance with recommendations for molecules optimized in an implicit solvent [224]. Normal modes of all structures were examined to verify that their ground states possess no imaginary frequencies and that transition structures possess only one imaginary frequency corresponding to bond formation or bond breaking.

7.5 Results and discussion

Experimental Results

Battery performance for the different electrolyte concentrations was studied employing differential electrochemical mass spectrometry (DEMS) analysis for a single discharge and recharge cycle at different current rates. Table 7.1 presents the total electron consumption for the oxygen reduction reaction (ORR) and the oxygen evolution reaction (OER), as well as the OER/ORR ratio for each reaction according to the ideal overall reaction 2 Li + O_2 $\rightarrow$ Li_2O_2. From the OER/ORR values we see that across the table the most efficient cells (bolded) were the lower concentration electrolytes. The 2.0 M and saturated electrolytes deteriorated with increasing current to the point that cycling at 1000 μA was not possible due to almost immediate passivation of the cathode surface.

Table 7.1: DEMS Result for Oxygen Reduction & Oxygen Evolution Reactions for Different Electrolyte Concentrations and Current Rates

Concentration (mol/L)	200 μA			500 μA			1000 μA		
	OER/ORR	$(e^-/O_2)_{dis}$	$(e^-/O_2)_{chg}$	OER/ORR	$(e^-/O_2)_{dis}$	$(e^-/O_2)_{chg}$	OER/ORR	$(e^-/O_2)_{dis}$	$(e^-/O_2)_{chg}$
0.1	0.69 ±0.05	1.93 ±0.07	2.84 ±0.25	**0.72 ±0.02**	2.06 ±0.03	2.91 ±0.12	**0.65 ±0.04**	2.06 ±0.01	3.16 ±0.15
1.0	**0.74 ±0.02**	2.01 ±0.02	2.71 ±0.05	0.66 ±0.01	2.00 ±0.02	2.99 ±0.02	0.64 ±0.02	2.04 ±0.01	3.21 ±0.09
2.0	0.65 ±0.03	2.01 ±0.02	3.10 ±0.13	0.58 ± 0.05	2.19 ± 0.12	3.80 ± 0.52	NA	NA	NA
2.6 (Saturated)	0.65 ± 0.02	2.02 ± 0.02	3.05 ± 0.05	0.49 ± 0.07	2.34 ± 0.15	4.13 ± 1.62	NA	NA	NA

Decoupling the discharge and recharge data shows that different effects appear to be taking place during each step of the cell cycle with additional variations seen for the different concentrations. For the lowest current rate across the different electrolytes concentrations the first discharge exhibited similar performance with the e^-/O_2 being close to the ideal value of 2.00. However, upon recharge the high concentration electrolytes had e^-/O_2 greater than $\sim$ 3.00, that was further exacerbated upon increasing the charging current to 500 μA, indicating significant parasitic chemistries. For the latter measurements, examining the gas

evolution data along with the cycling behavior revealed several differences across the different concentrations.

Isotopic labeling experiments coupled with DEMS have shown that H_2 gas originates from solvent decomposition [209] with changes to this metric being indicative of solvent stability. Figure 7.1a shows the charge curves with a current rate of 500 μA for each concentration and figures 7.1b and 7.1c show the H_2 and O_2 gas evolution data from DEMS analysis, respectively. The key difference found was that the slope of the recharge curves changes according to the electrolyte concentration, which change the overall overpotential during the recharge step. As can be seen in Fig. 7.1a the saturated solution produces the steepest slope and the 0.1 M has the most gradual rise and is the last to reach the plateau above 4.5V. This suggest that the saturated solution is more susceptible to parasitic side reactions, which limits its capacity during both discharge and recharge phases, and results in the high H_2 gas evolution even before all of the 0.33 mAh equivalent Li_2O_2 produced during discharge is consumed. Examination of Fig 7.1c, further indicates that higher concentration electrolytes are less stable since they have lower oxygen evolution than the lower concentration electrolytes, which is in line with the ORR/OER results in Table 7.1. Overall these finding are in line with the expected Dakin oxidation mechanism for DME decomposition, since the amount of decomposition is expected to be proportional to the concentration of Li^+ in the electrolyte solution. [209, 210] The additional variations observed over 4.5 V are believed to be mainly due to differences in the electrolyte and carbon decomposition at this high potential, however, since practical Li-O_2 batteries should operate at lower potentials we did not pursue this further. Although outside of the purview of this work, the electrolyte concentration effects in the presence of catalysts will be an important topic to further investigate given that catalyst both reduce overpotentials [225, 226, 35] but also accelerated electrolyte decomposition rates. [227, 210, 228]

As shown in Figures 7.2a-d, all of the electrolyte solutions experienced an increase in the overpotential with increasing current rate. However, variation in the differences between the cells was indicative of different cell failure mechanisms. For the most dilute electrolyte mixture we observed the most notable increases in the overpotential plateu with increasing current. However, this plateau had the slowest onset, which is critical since voltages beyond 3.5 V accelerate electrolyte decomposition. Impedance analysis performed on the 0.1 M cell prior to discharge and Li_2O_2 production suggests that Li-ion conductivity is low compared to cells with higher electrolyte salt concentrations. Furthermore, successive iterations of TFSI anion decomposition over multiple cycles reduces soluble Li^+ and produces insoluble Li-salt species on the cathode surface so that even though, and interestingly, the OER/ORR ratio is optimal compared to the other concentrations at high current rates, we do not expect batteries with low concentration electrolytes to have extended lifetimes over multiple cycles. For the 2.0 M and the saturated solution we observed overpotentials comparable to those observed for the 1.0 M concentration, but with much steeper increase during the initial recharge phase. This observation coupled with the fact that at current rates beyond 500 μA, the high concentration electrolytes could not deliver comparable discharge capacities, is indicative of susceptibility to surface passivation occurring during discharge. These results

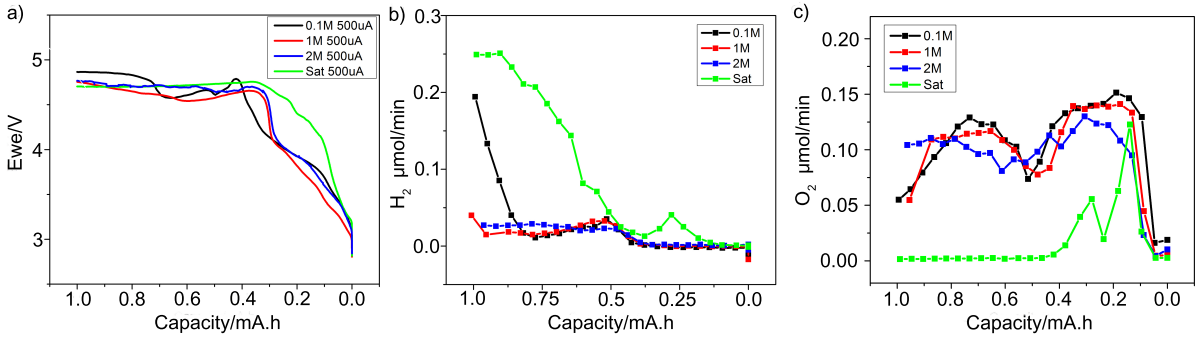

Figure 7.1: (a) First cycle charging curves different cell employing different electrolyte concentrations. (b) Hydrogen gas evolution during the first recharge for cell with different electrolyte concentrations. (c) Oxygen gas evolution during the first recharge for cell with different electrolyte concentrations. Cells were cycled at a rate of 500 μA with total capacity of 1.0 mAh for both discharge and charge, with the exception of the saturated electrolyte which had discharge capacity of 0.33 mAh.

also highlight that using high concentration electrolytes does not provide the same level of stability as it does in the Li-ion or Li-metal chemistries [211, 212, 213, 214, 215], with the most important difference being the presence of Li_2O_2 that can interact with either solvent or anion components of Li salt.

To determine whether sudden death was due to electrolyte salt decomposition and precipitation we performed cell discharges at different current rates under constant pressure until cells completely passivated and exhibited a sharp voltage drop (cut off at 1.5 V). Figure 7.3 shows the results from this set of experiments indicating that the 2.0 M and saturated electrolyte solution had lower potential discharge capacities at currents above 500 μA compared to the 1.0 M and 0.1 M electrolyte solutions. Furthermore, the 0.1 M solution had an interesting trend of increasing its capacity with increasing current. We believe this is directly related to the fact that the electrolyte decomposition pathway has been shown to have a primary kinetic isotope effect for hydrogen production, [209] which implies that the low Li^+ concentration and high currents kinetically limit parasitic DME decomposition while allowing the primary Li_2O_2 production pathway to proceed more quickly. To further investigate the discrepancies between electrolyte concentrations, we probed the surface morphologies and chemistry by employing NMR, SEM, and EDS analysis to investigate the presence of decomposition products from both the solvent and salt on the cathode.

As was previously established by McCloskey et al. [210], ^{1}H and ^{19}F NMR can be used to analyze and quantify the presence of decomposition products in Li-O_2 batteries. NMR results from several variants of the experimental conditions are presented in Appendix C in Figures C1-C6, including including constant volume and constant pressure experiments at different current rates for the varying electrolyte concentrations. In agreement with the Dakin oxidation mechanism of the DME solvent, higher Li^+ content associated with higher concentration

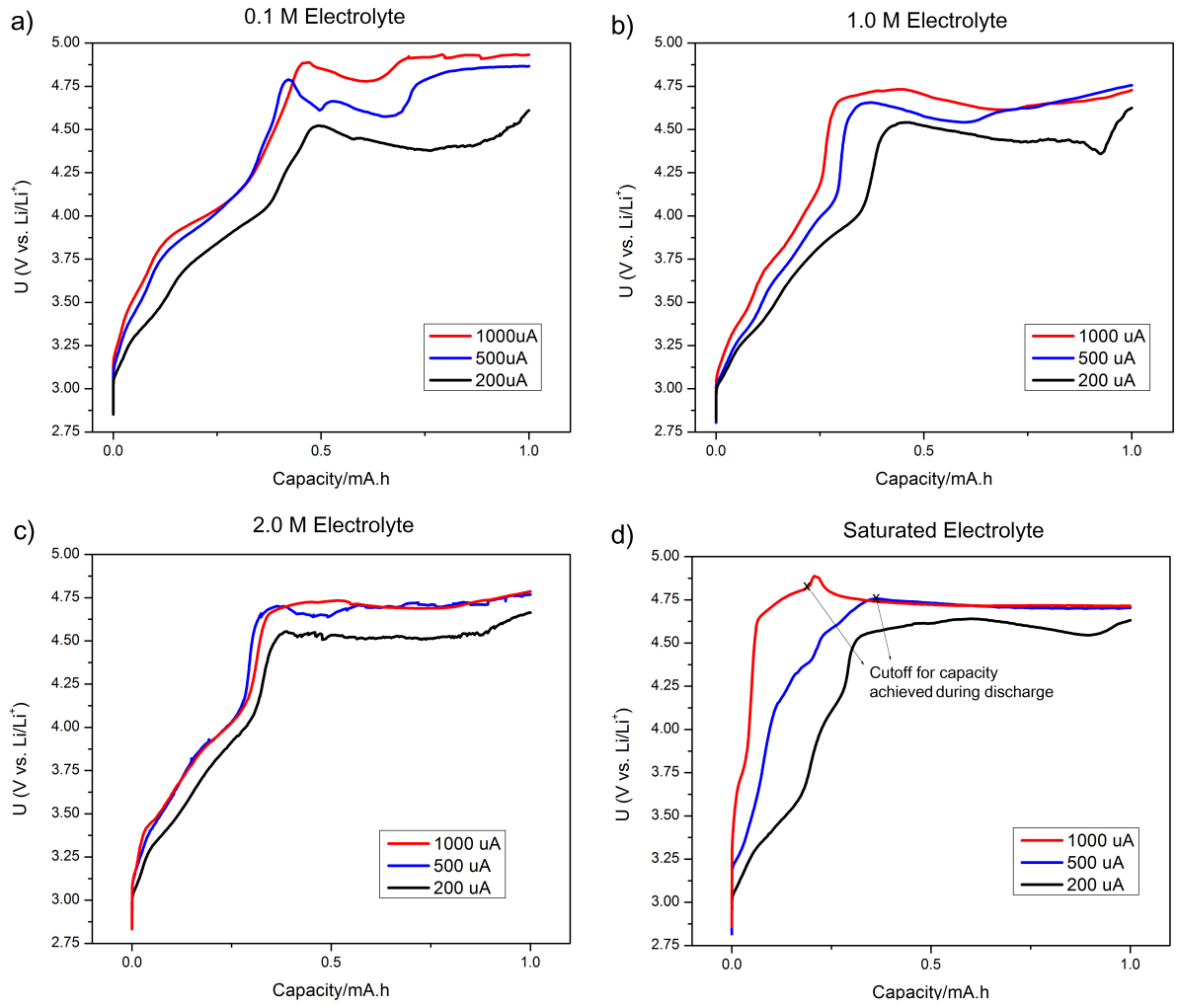

Figure 7.2: Recharge curves (a) 0.1 (b) 1.0 M (c) 2.0 M and (d) saturated electrolyte concentrations at current rates of 200 μA, 500 μA and 1000 μA. The last figure corresponding to cells utilizing saturated electrolyte were recharged for 1.0 mAh; instances when lower discharge capacity was achieved are indicated.

electrolytes resulted in increased DME decomposition, even when cells were only partially discharged. Furthermore, the higher concentration electrolytes also exhibited increased fluorine decomposition products, which indicates that Li-TFSI is susceptible to breakdown in the Li-O_2 chemistry. Figure 7.4 shows the ^{19}F NMR spectra of samples collected from cells discharged at a current rate of 200 μA until cell death with hexafluorobenzene added as an internal standard. The data shows not only that the high concentration electrolytes have significant TFSI decomposition, but that the 0.1 M solution has approximately ~ 0.2 μmol of salt decomposed during the first discharge to U = 1.5V. This amount of salt decompo-

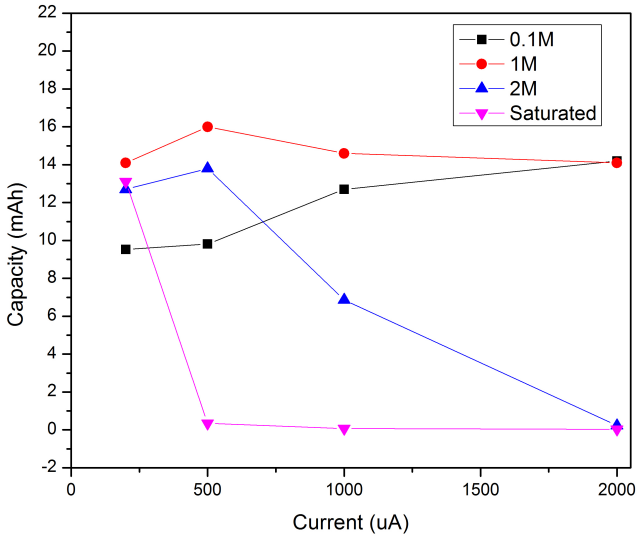

Figure 7.3: First discharge capacity obtained for cells with different electrolyte concentration that were discharged at different current rates until sudden cell death (U_{min} = 1.5 V). Cells containing saturated and 2.0 M electrolyte (magenta and blue curves) exhibited rapid passivation at high current rates, while cells with 0.1 M and 1.0 M electrolytes (black and red curves) had capacities less susceptible to current effects.

sition products accounts for 8-10% of the total Li^+ concentration, suggesting that normal battery recharge and discharge processes will eventually lead to issues for battery operation, possibly including mass transport limitations. Additionally, McCloskey et al. [221, 206] previously showed that the current becomes dependent on Li^+ concentration as electrolyte concentration decreases below 0.1 M. This provides a potential explanation for why cells assembled with 0.1 M electrolyte exhibited lower capacity than cells prepared with 1.0 M electrolyte solution (9.8 mAh vs 14.0 mAh at 200 μA current rate till voltage drop of 1.5 V, respectively).

In order to also understand the potential failure mechanism of the high-concentration electrolyte cells, we performed both SEM and EDS analysis of the cathodes after one cycle to examine changes to the surface. Figure 7.5 shows an elemental map from EDS analysis from a sample that utilized the saturated electrolyte and was discharged at a current rate of 2.0 mA with a total discharge capacity of 0.1 mAh to a voltage cutoff of 1.5V vs Li. EDS analysis shows homogenous surface coverage of F, N and S containing insoluble particles, which are believed to be responsible for the passivation of the cathode resulting in the sudden voltage drop. The accompanying table displays the relative presence of the different elements contained in the cathode for samples with varying concentration and current rates. As expected the samples with high concentration electrolyte quickly passivated, with a relative low oxygen content near the surface but pronounced presence of F, S and N. It is worth reiterating that prior to taking SEM images and doing EDS analysis the

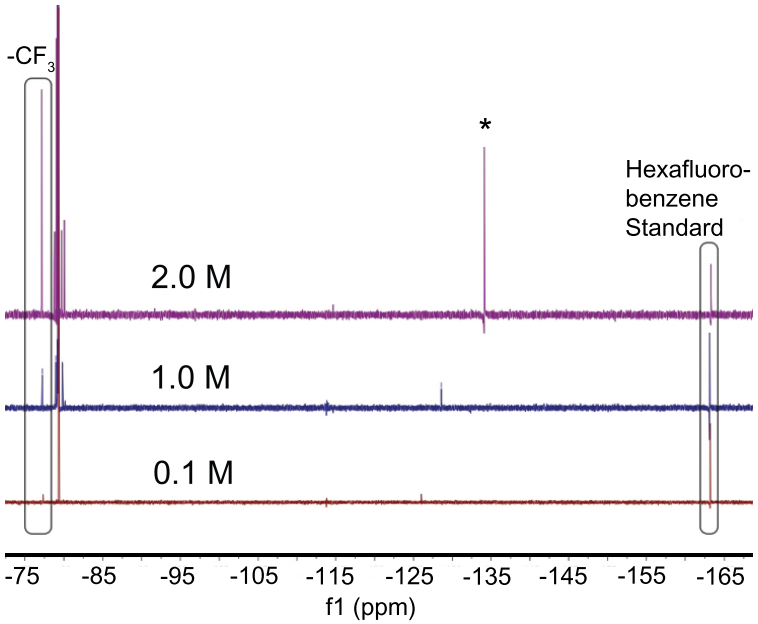

Concentration	Discharge Capacity (mAh)	Total Lithium Decomposition Products (μmol)
0.1	14.2	0.18
1.0	14.2	0.29
2.0	13.8	10.65

Figure 7.4: ^{19}F NMR spectra of samples collected from cells with different electrolyte concentrations that were discharged until sudden cell death (U_{min} = 1.5 V). Each sample contains a hexafluorobenzene standard to quantify fluorine containing decomposition products. The asterisk corresponds to an uncharacteristic decomposition product that appears in the sample from the 2.0 M containing cells. Although proper identification falls outside of the scope of this work, potential compounds may contain the functional groups CF_2Li or -CF_2H. The accompanying table contains the quantified concentration of lithium fluoride compounds along with the achieved discharged capacity.

samples were washed multiple times with DME to remove any leftover soluble salts, and that the P50 cathode did not contain any fluorine-containing binder. The results from the table again confirm that the high-concentration electrolytes suffer from increased salt decomposition with the sample discharged at low currents having higher F signal for the high concentration electrolyte. Because EDS is a surface-sensitive technique the reduced oxygen signal obtained for the higher concentration electrolytes is suggestive of surface passivation occurring that blocks further Li_2O_2 formation by limiting electronic conduction in the solid. This finding is in line with the theoretical predictions made by Lau et al. [229] that postulate that formation and accumulation of side products is comparable to a further increase in the current density resulting in the significant decrease in capacity. Further evidence that the higher electrolyte concentrations are failing due to surface passivation by side products is seen by analysis of the impedance spectra of pristine and discharged cells shown in Figures

7.6. Impedance spectra on pristine cells shown in Fig 7.6a and 7.6b reveal that the lowest electrolyte concentration had the highest impedance, which indicates that cells with electrolyte salts at this concentration suffer from diminished ionic conductivity when compared to the higher-concentration cells. Cells discharged until passivation at a current rate of 2.0 mA indicated that only the 0.1 M and 1.0 M cells experienced an increase in impedance after discharge (Fig 7.6c and 7.6d). The increase is due to the formation of Li_2O_2, which is only formed in appreciable amounts at these concentrations (see figure 7.3). For cells using 2.0 M and saturated electrolytes, capacity was modest and there was no observed increase in resistance at the same current rate, which suggests that the surface is not passivated by insulating Li_2O_2, but rather that parasitic products act to increase the required kinetic overpotential for Li_2O_2 formation. Combining the NMR and EDS results suggest that the higher concentration electrolytes have worse performance due mainly to the higher net decomposition of the electrolyte producing more side products that can cover a larger area of the cathode surface, thus further interfering with the critical surface chemistry of the Li-O_2 battery.

7.6 Computational Results

The decomposition of TFSI by Li_2O_2 was investigated with DFT calculations with the dispersion-corrected B3LYP-D3 method. Two mechanistic possibilities, shown in Figure 7.7, were examined for the formation of products detected by ^{19}F NMR. We postulated that Li_2O_2 decomposes charge-neutral TFSI after initial calculations showed spontaneous decomposition under these conditions. The presence of neutral TFSI is experimentally expected under conditions where trace water is found or when H^+ is formed during Li_2O_2-facilitated DME decomposition. A molecular model of Li_2O_2 was used throughout this study rather than a bulk model or the Li_2O_2 surface. Both pathways are derived from the initial coordination of Li_2O_2 to TFSI to form INT1, a compound that is 10 kcal/mol more stable than the reactants. Pathway A involves cleavage of the N-S bond in TFSI facilitated by the nucleophilic attack of Li_2O_2 proceeding from INT1. This process is spontaneous - the transition state for the transformation of TS1-CF3 into INT1 is about 0 kcal/mol. N-S bond cleavage results in the exergonic formation of INT2-NS, a complex comprising lithium trimethylsulfonamide and $LiOSO_3CF_3$, which is $\sim$ 46 kcal/mol more stable than the reactants. The completely separated lithium trimethylsulfonamide and $LiOSO_3CF_3$ species formed by N-S bond cleavage is also exergonic by -28.0 kcal/mol. Pathway B involves initial formation of LiO_2CF_3 from simultaneous elimination of a CF_3 group from TFSI and trapping by Li_2O_2. The transition state for this process, TS1-CF_3, lies 16 kcal/mol above INT1 and directly results in the formation of INT2-CF_3, a complex comprising LiO_2CF_3 bound to SO_2 and $LiNHSO_2CF_3$. The formation of INT2-CF_3 is exergonic by 84 kcal/mol with respect to Li_2O_2 and TFSI. The expectation is that LiO_2CF_3, if formed, becomes converted into $LiCF_3$ and 3 O_2. Overall, these results suggest that pathway A is the dominant mechanism for TFSI decomposition; the barrier for TFSI decomposition via pathway B is larger

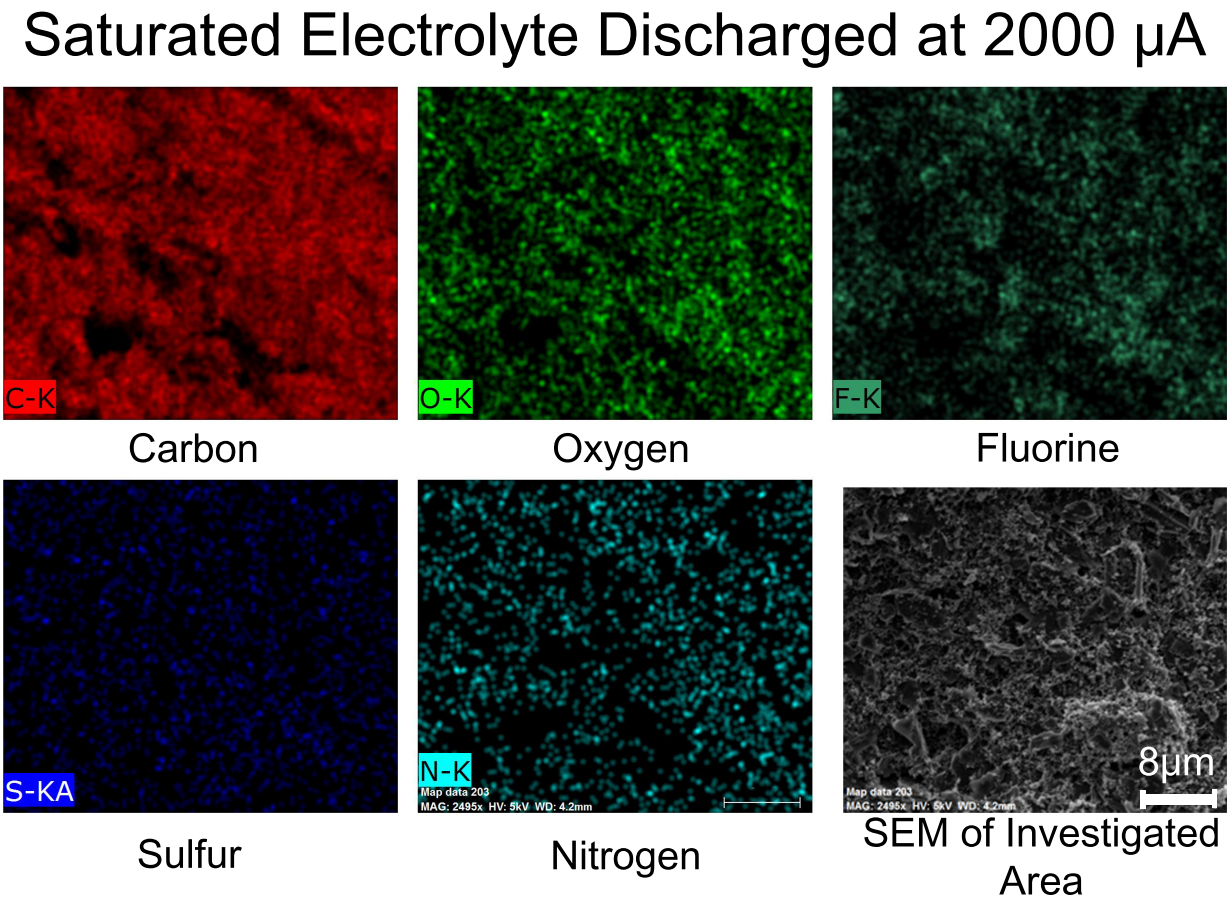

Concentration (mol/L)	Current Rate (μA)	Discharge Capacity (mAh)	C concentration (%)	O concentration (%)	N concentration (%)	F concentration (%)	S concentration (%)
0.1	200	8.1	32.73	60.12	3.11	2.61	1.43
2.0	200	12.7	36.44	53.94	3.69	3.32	2.60
Saturated	200	12.1	33.22	47.37	4.53	9.00	5.88
2.0	2000	0.06	83.64	8.44	2.78	3.85	1.29
Saturated	2000	0.1	83.61	7.72	2.80	4.37	1.50

Figure 7.5: EDS analysis of a P50 cathode extracted from a cell with saturated electrolyte discharged at 2.0 mA, with a total capacity of 0.1 mAh. The accompanying table includes the elemental concentration for this sample (5th entry), as well as for other cathodes extracted from cells with different electrolyte concentration and varying current rates.

than that of pathway A involving spontaneous decomposition of TFSI by Li_2O_2. $LiCF_3$ could be formed from further decomposition of the spontaneously formed lithium trimethylsulfonamide and $LiOSO_3CF_3$. Combining these results with prior findings that DME can decompose via a Dakin oxidation mechanism, suggest that high concentration electrolytes will first accelerate DME decomposition due to higher Li^+ concentration, which in turn will increase the concentration of protons (H^+) available to bind to the TFSI anion, leading to its decomposition.

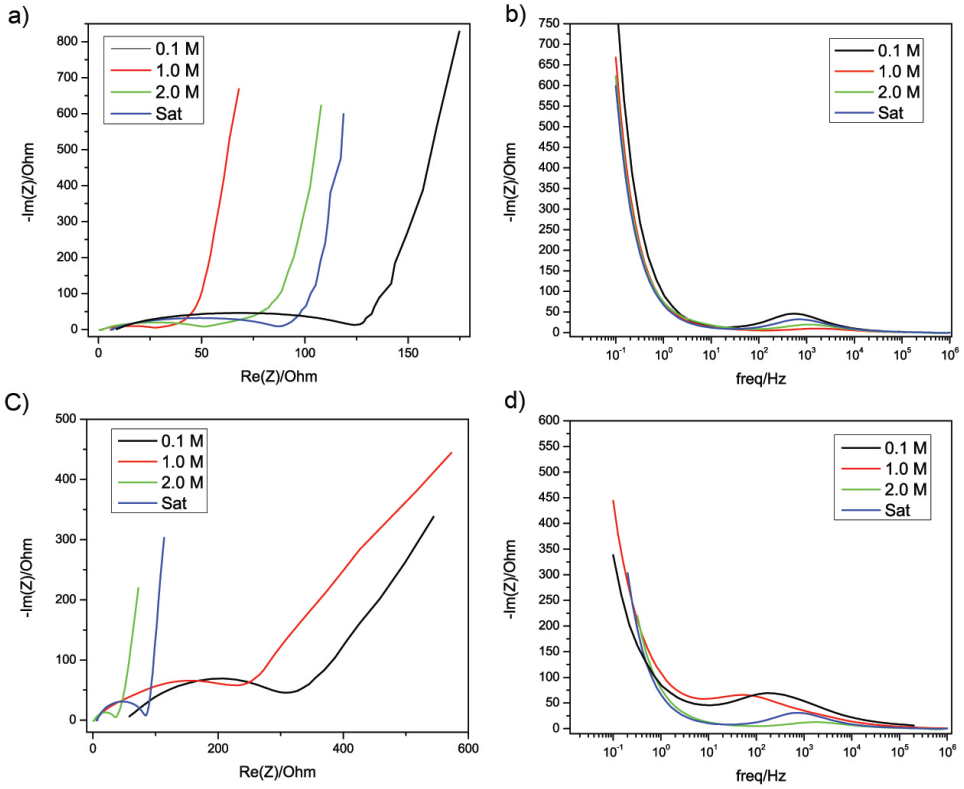

Figure 7.6: a) and b) shows the impedance spectra for cell with different electrolyte concentration prior to discharge. c) and d) Shows the impedance spectra from the same cells after discharge to Umin = 1.5 V with a current rate of 2 mA.

7.7 Conclusion

By examining the performance of Li-O_2 batteries with varying concentrations of the electrolyte DME + LiTFSI, we have identified two potential different failure mechanisms for this cell chemistry based on the decomposition of the anion in the electrolyte salt. Cells assembled with dilute electrolytes were shown to have higher impedance before cycling resulting from low Li^+ concentration, which was further aggravated after deep discharge experiments. ^{19}F NMR analysis showed that in all cases, the TFSI anion is consumed through parasitic processes during cell operation, which acts to decrease the concentration of soluble Li^+ in the electrolyte. For the high concentration electrolytes we have shown that when using high overpotentials during charging, there is a steady increase in the amount of decomposition products coming from both solvent and salt of the electrolyte, and attribute the sharp rise in potential to cell inefficiency and rapid electrolyte decomposition, as exemplified by high levels of H_2 production and low O_2 production at the onset charge. SEM and EDS analysis

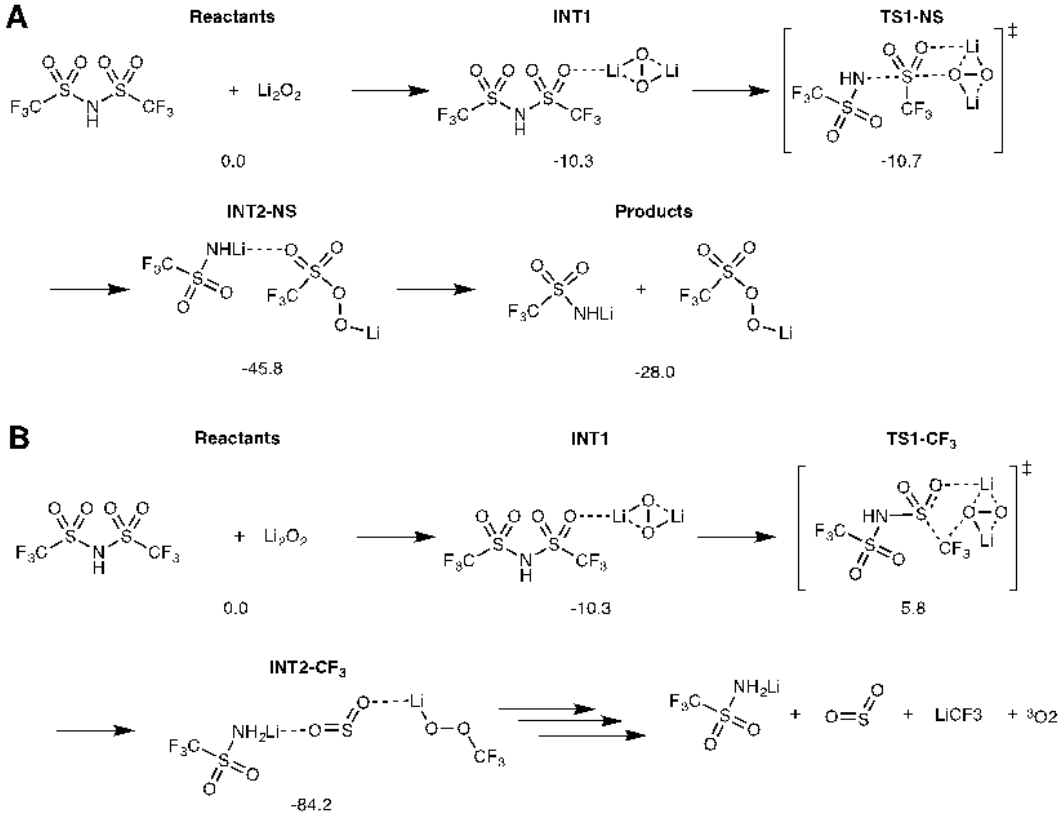

Figure 7.7: Computed structures and free energies (in kcal/mol) for the decomposition of TFSI by Li_2O_2. Pathway A. Possible mechanism for N-S bond cleavage. Pathway B. Possible mechanism for $LiCF_3$ formation.

shows that these decomposition products can coat the cathode surface leading to premature passivation that resulted in sudden death. The passivation layer generally has elemental concentration of F above 4%, consistent with insoluble species containing -CF_3 groups as well as LiF, as identified by ^{19}F NMR. Out of the electrolytes studied, DEMS measurements for a single discharge and recharge suggested that lower electrolyte concentrations provided superior performance in terms of oxygen reduction, oxygen evolution and overall efficiency in Li-O_2 batteries. This finding is contrary to results found in Li-ion batteries where ultra concentrated electrolytes provide additional stability to the cells. This difference was investigated by utilizing first principle calculations, with results showing that the TFSI anion can become unstable under the oxidizing presence of Li_2O_2, particularly if it becomes neutral by combining with a proton. These results highlight the need for more stable lithium electrolyte salts that are stable to the oxidizing effects of Li_2O_2.

7.8 Acknowledgement

I.M.M. would like to acknowledge the Leading to Africa program sponsored by IBM for providing financial resources to conduct a summer research internship. In addition, I.M.M. would like to thank Dr. Don Bethune for help with DEMS, Ms. Leslie Thompson for SEM/EDS analysis, Dr. Jed Pitera for helpful scientific discussions and Simona Dalmasso for assistance with cell assembly and testing.

Chapter 8

Conclusions and Future Work

8.1 Summary of Results

This dissertation presents several experimental and computational results that explore material behavior in applications related to energy storage and conversion. The results from each section provide a guideline for future material design and implementation.

Chapter 3 explores the proton transport properties of $DyPO_4$ employing DFT calculations. The results indicate that due to the crystal structure this material is expected to have highly anisotropic conduction, with fast diffusion possible only along 1D pathways. The results indicate that dopant effects intended to aid proton incorporation can also result in binding that increase energy barriers for diffusion.

Chapter 4 reports on the observed surface reconstruction of $Li(Ni_xMn_xCo_{1-2x-y}Ti_y)O_2$. Utilizing STEM and XAS, direct evidence of a phase transformation from the layered $R\bar{3}m$ structure to $Fm\bar{3}m$ rock salt phase was observed. The results indicate that this phase transformation can occur upon contact with electrolyte solution, and that it becomes a significant source of inefficiency during high voltage cycling of Li-ion batteries using this cathode material. This finding is confirmed via DFT calculations that indicate that the phase transformation becomes more energetically favorable with lithium removal. These results highlight a potential upper voltage limit for this class of material, showing that high voltage not only results in electrolyte failure but also cathode decomposition.

Chapter 5 provides results from DFT calculations that help understand the impact of Ti substitution in $Li(Ni_xMn_xCo_{1-2x-y}Ti_y)O_2$. The results show that experimentally achieved higher capacities for Ti substituted materials can be attributed to a decrease in the intercalation voltage at higher states of charge. This effect is attributed to local structural and electronic changes due to the formation of an electron polaron as a result of Ti substitution of Co. Furthermore, improved cyclability is attributed to improved stabilization of the layered structure, thus suppressing surface reconstruction into the previously reported rock salt phase.

Chapter 6 investigates the electrolyte concentration effect in the Li-O_2 battery chemistry.

For the electrolyte composed of lithium triflimide (LiTFSI) in 1,2-dimethoxyethane (DME) we report different failure mechanisms for cells employing dilute and saturated electrolytes, which arise from decomposition of the TFSI anion. Employing DEMS analysis, we show that electrolytes having concentrations between 0.1 and 1.0 M outperform higher concentration. ^{1}H and ^{19}F NMR results indicate that although cells with lower concentrations behave more efficiently, they are susceptible to failure due to mass transport limitations from a loss of soluble Li ions. NMR, SEM, and EDS analysis also show that cells with high concentration electrolytes (>2.0M) experience cathode passivation, explaining their poor performance. Lastly two possible TFSI anion decomposition pathways we explored using DFT calculation. The results indicate a high susceptibility to decomposition in the presence of molecular Li_2O_2 when the TFSI anion is charge neutral due to proton binding.

Chapter 7 reports computational and experimental results for different sodium-ion anodes based on titanates with lepidocrocite type structures. DFT calculations show that the capacity for this type of material is site limited, with a comparison of C-type and P-type phases indicating that the latter is expected to have the highest possible capacity due to lower electrostatic interactions between intercalated sodium ions. Analysis of structural changes during sodiation reveal that the presence of Li in the Ti corrugated layer helps reduce strain during sodiation allowing for higher sodium content. Comparison between computational and experimental structural changes during sodiation suggest that these types of materials are susceptible to solvent uptake, which correlates with a decrease in practical capacity. Lastly, nudge elastic band calculations reveal that sodium diffusion in these materials is a function of state-of-charge and of local electrostatic interactions.

8.2 Unpublished and Future Work

It has been the focus of this work to provide deeper understanding of the material challenges faced in fuel cells and batteries. The combined experimental and computational approach illustrates the capability of developing deeper understanding of the problems faced by each system. The knowledge gain allows for easier identification of critical issues, and from each chapter a series of design criteria has been postulated to not only test findings but help push forward the performance of available materials.

From chapter 3 one of the main findings suggested that higher symmetry crystal structures were more likely to have higher diffusion pathways for proton diffusion. This was in line with experimental results that showed superior performance of perovskites over tested rare-earth phosphates. However, from the results $DyPO_4$ is predicted to have among the lowest bulk diffusion paths for a proton conductor electrolyte. Because this path is only along one dimension, testing requires advanced manufacturing techniques such as molecular beam epitaxy or pulsed laser deposition to grow uniform oriented films. Because $DyPO_4$ has a tetragonal crystal structure compared to the monazite structure of $LaPO_4$ or $CePO_4$, this material is also useful to further understanding how proton incorporation occurs in these materials. Future DFT calculations can be performed on $DyPO_4$ to understand how the higher

symmetry crystal structure impacts the kinetic rate of hydrolysis of pyrophosphate defects, which are believed to be the main mechanism for proton incorporation into phosphates.

The results from chapter 4 provided direct evidence for surface reconstruction in a Li-ion battery cathode material. The discovery of this phase transformation showcased one of the likely shortcomings that this type of material can have during high voltage cycling. This is particularly important given the increased interest in all solid state batteries, that seek to combine both high energy density of pure Li metal with high voltage cathode materials in an effort to maximize energy density and safety. From our results it was observed that the surface reconstruction was an effect of both exposure to liquid electrolyte and high state-of-charge, and future experimental research should confirm if this phase transformation can occur in a solid state battery. The work described in this chapter also highlighted several techniques that can be used to explore surface reactions of other battery systems. Unpublished results have investigated the mechanism by which the surface reconstruction occurs. Phonon calculations indicate that the layered structure becomes unstable if oxygen is lost from the structure, but that it can be re-stabilized with additional lithium removal. This series of steps are believed to be precursor to the formation of an intermediate spinel structure that precedes the rock salt structure.

Chapter 5 was a continuation of the findings of chapter 4 and previously reported experimental work that had indicated superior performance in the NMC cathode whith 2-4% substitution of Co with Ti. The findings suggested that Ti was a good substituting cation since it was a strong oxygen binder, which helped stabilize the layered structure during delithiation. An alternative dopant for future experimental and computational testing was V, since it is expected to have a similar effect in suppressing the surface reconstruction reaction. Additional future work is expected to examine similar effects in different stoichiometric ratios in the NMC cathode, examining particularly Ni rich cathodes. Another important aspect to be studied in layered cathode materials is the effect of substituting cations near a surface. Because the calculations performed in this dissertation were only applicable to the bulk, a similar analysis is required in a slab model in order to better understand the process in the most electroactive region of the material. Because the system studied herein has at least 5 components, simulating slabs might require the use of a more simple layered structure such as $LiCoO_2$. Lastly, the results from this chapter made use of the assumption of an ordered structure in the transition metal layer, and future research should be performed to verify the findings when this layered is is modeled as having random substitutional disorder.

One of the major findings from chapter 6 was the identification of TFSI decomposition upon becoming charge neutral and being exposed to molecular Li_2O_2. Future computational work is required to explore the decomposition pathways when TFSI is exposed to a Li_2O_2 surface. Further work should also be focused on exploring the chemical stability of various other glymes in order to assess both chemical trends and asses if there is a way of stabilizing this class of anion under the redox capability of Li_2O_2. This approach should include the screening of specific additives that can reduce either solvent or salt decomposition. Lastly with the knowledge of separate failure mechanisms, it was postulated that alternative salts are required which can tolerate exposure to Li_2O_2. Although the development of such ma-

terials is outside the purview of this work, it remains a critical issue for this class of battery.

The work in chapter 7 is part of ongoing work that is examining the sodium intercalation mechanism into different titanate structures. From the findings reported there is evidence that for corrugated titanates site limitations create an upper bound for the capacity these materials can achieve. In order to circumvent this problem, ion exchange with higher valence cations is proposed as a strategy to reduce initial sodium content to create more sites for sodium intercalation. Another critical issue that needs to be explored for this class of materials is the susceptibility to phase transformation at different states-of-charge. The ability for corrugated Ti layers to shift in relation to each other, or bind together, can present both an asset or liability for the performance of these materials. Through the use of DFT calculations, the energetics for a phase transformation can be examined, with pseudo equilibrium experiments performed in tandem to assess potential kinetic limitations for such changes.

Appendix A

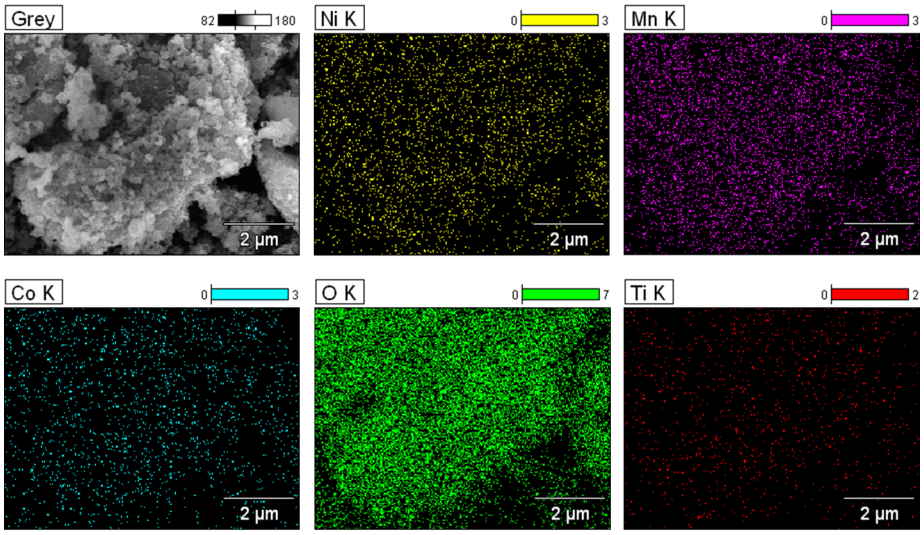

Elements	Ni	Mn	Co	Ti
Atom %	38.6%	40.2%	18.5%	2.7%

Figure A.1: SEM/EDS mapping of $LiNi_{0.4}Mn_{0.4}Co_{0.18}Ti_{0.02}O_2$. The experimental error of the mapping is $\pm 1\%$. The atomic percentages of each element are based on multiple SEM/EDS mapping results.

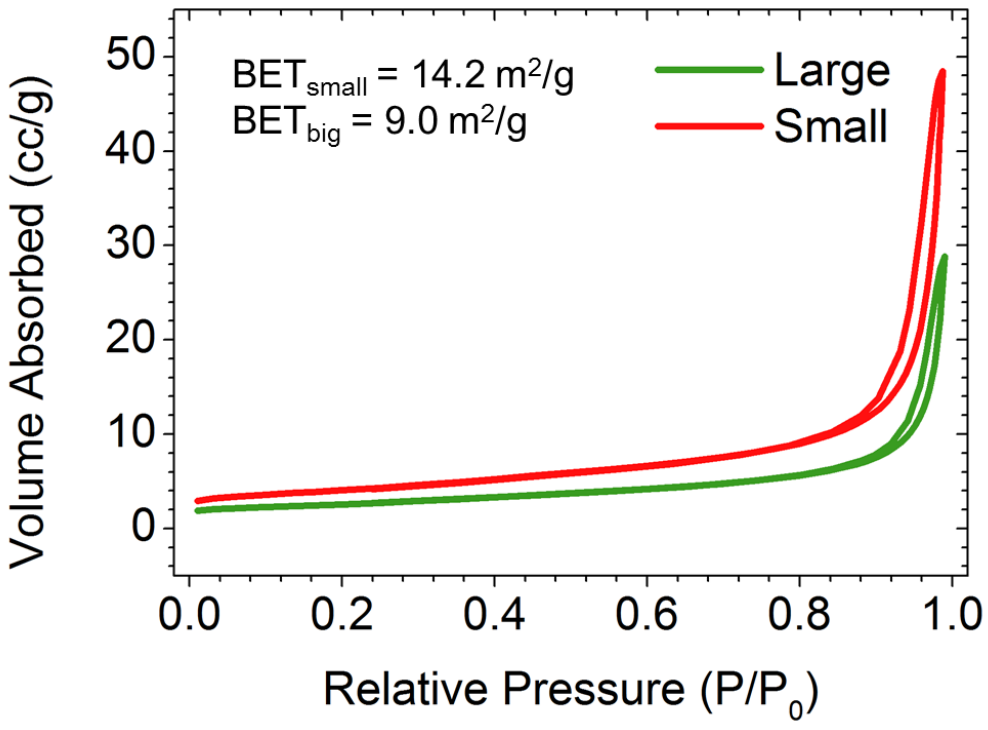

Figure A.2: N_2 adsorption and desorption isotherms of NMC materials with varied specific surface areas (i.e., particle sizes). This study was primarily performed on the material with larger particle size.

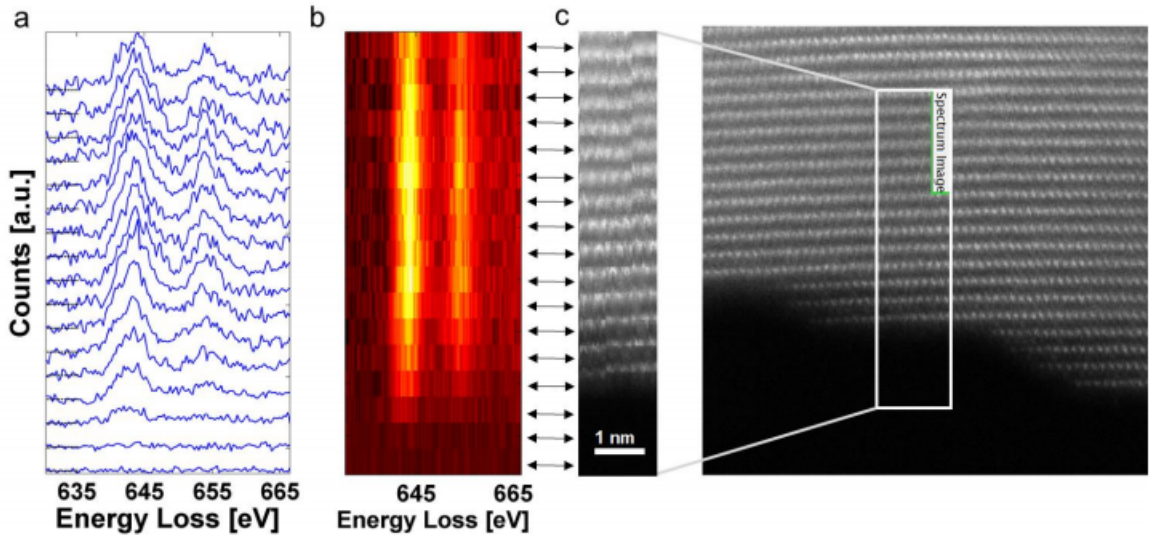

Figure A.3: EELS line scan profile for a pristine NMC particle along the <001> direction: (a) Mn L-edge EELS spectra along the scanning pathway, (b) 2D EELS map visualizing no peak shift, and (c) the simultaneously acquired subpixel mosaicked ADF-STEM image. The onset energy for Mn L-edge spectra remains constant along the scanning pathway indicating that the Mn oxidation state is constant at +4.

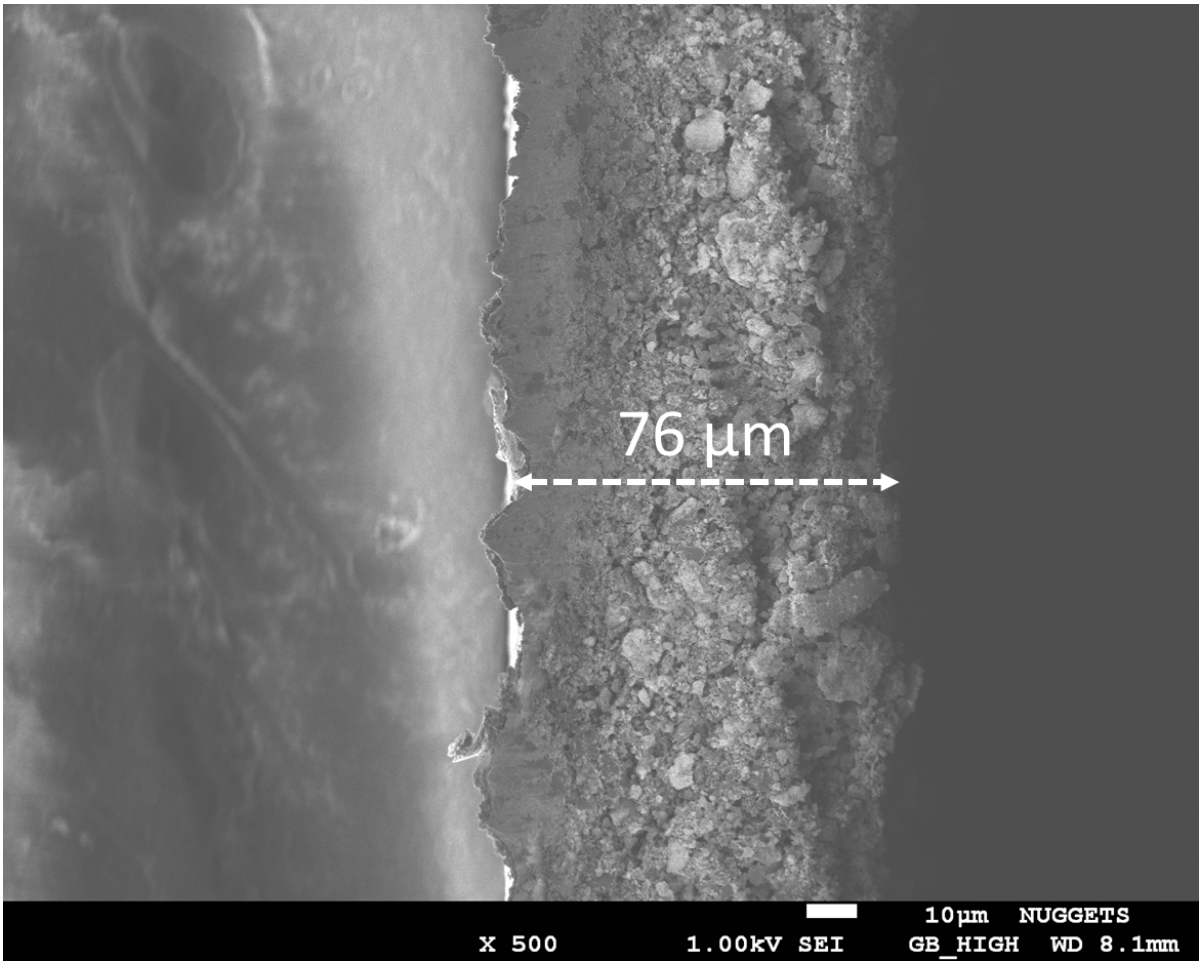

Figure A.4: Cross-section SEM image of a typical composite electrode (84 wt% active material, 8 wt% polyvinylidene fluoride, 4 wt% acetylene carbon black and 4wt% SFG-6 synthetic graphite on an aluminum current collector, visible on the left side of the image.

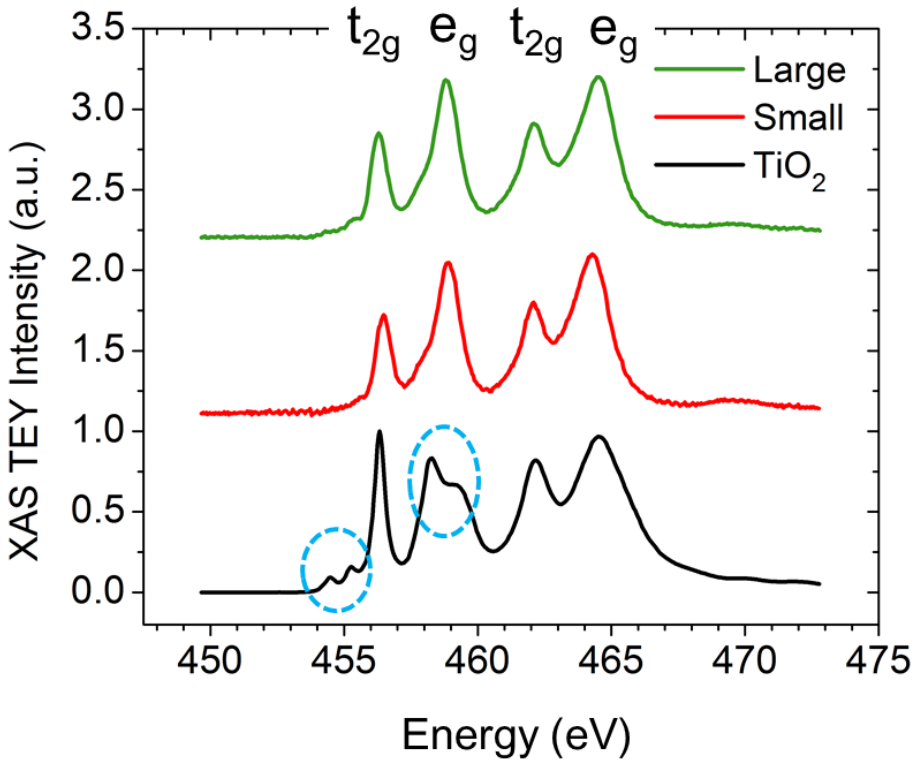

Figure A.5: Ti L-edge spectra of NMC materials and standard anatase TiO_2. The pre-edge features and splitting of e_g/L_3 are circled. The splitting of the L_3 doublet e_g (circled) is due to the tetragonal distortion in anatase TiO_2. The different shape of L_3 doublet e_g in the NMC materials suggests that Ti is incorporated in the lattice and is not phase separated to either anatase or rutile.

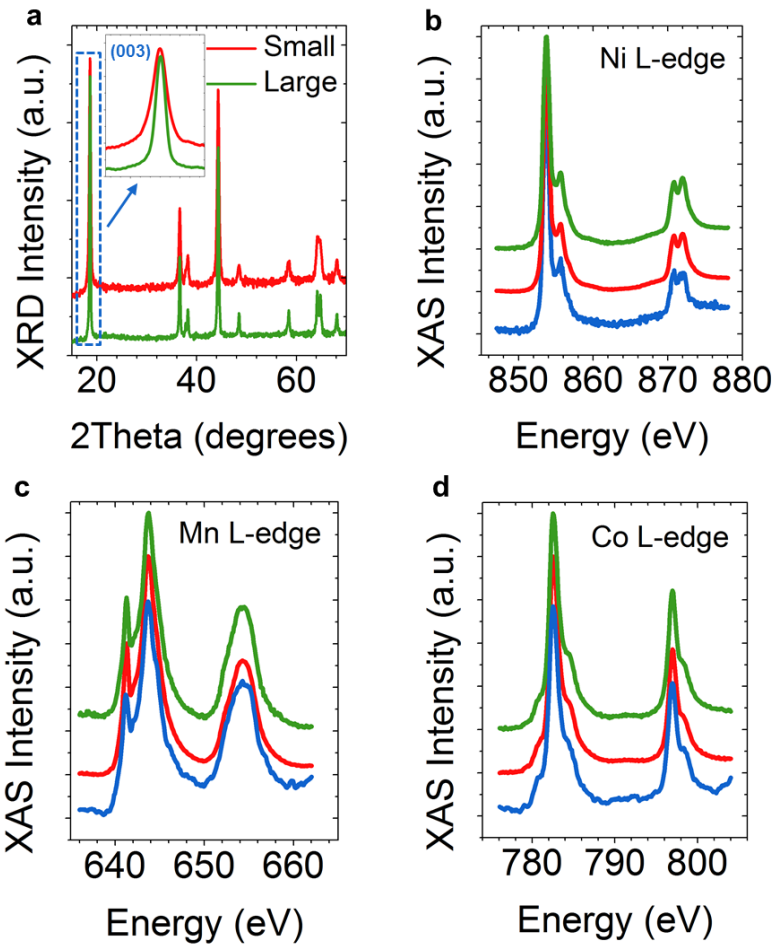

Figure A.6: (a) Comparison of XRD patterns for NMC materials with two different particle sizes. XAS spectra of the NMC material with smaller particle size (note that the one with larger particle size is presented in the main text): (b) Ni L-edge, (c) Mn L-edge and (d) Co L-edge using Auger electron yield (blue), total electron yield (red) and fluorescence yield (green) modes.

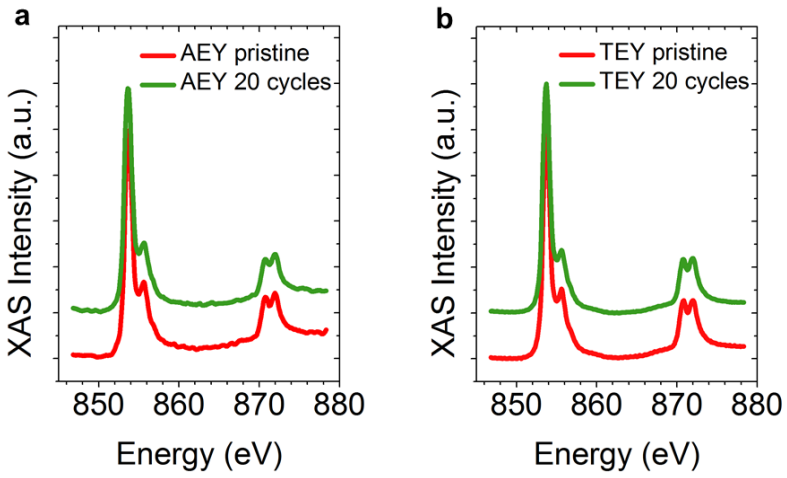

Figure A.7: XAS Ni L-edge spectra for the samples in the pristine state (red) and after 20 charge-discharge cycles in a voltage range of 2.0 V- 4.7 V vs Li/Li+ (green): (a) AEY mode and (b) TEY mode.

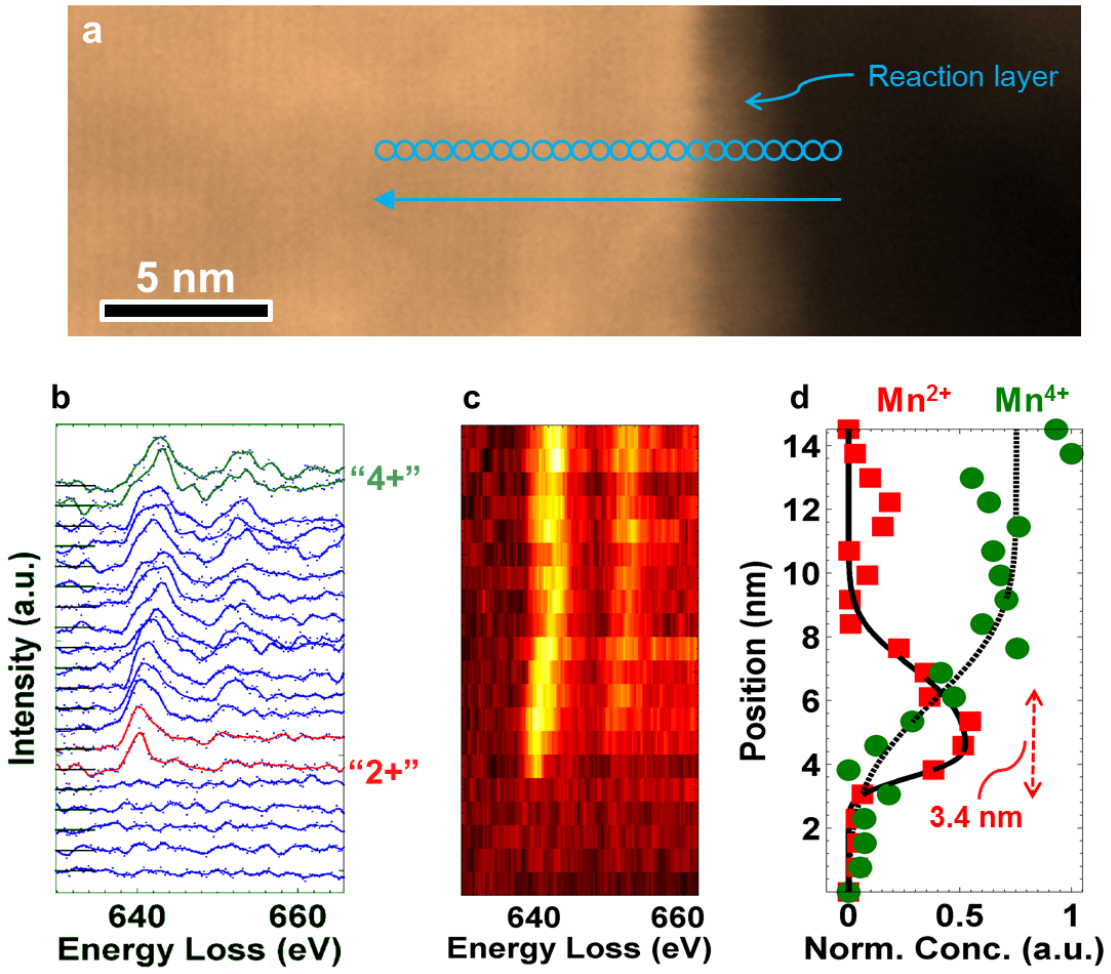

Figure A.8: EELS line scan profile for an NMC particle along <001> direction: (a) STEM image to indicate scanning pathway, where a surface reaction layer is labeled in the image. (b) Mn L-edge EELS spectra along the scanning pathway, (c) 2D EELS map to enhance the visualization of peak shift, and (d) concentration profiles for Mn^{2+} and Mn^{4+} using a linear combination method. The measurements were performed on electrodes in the discharged state after 20 cycles between a voltage range of 2.0 V- 4.7 V vs Li/Li^{+}.

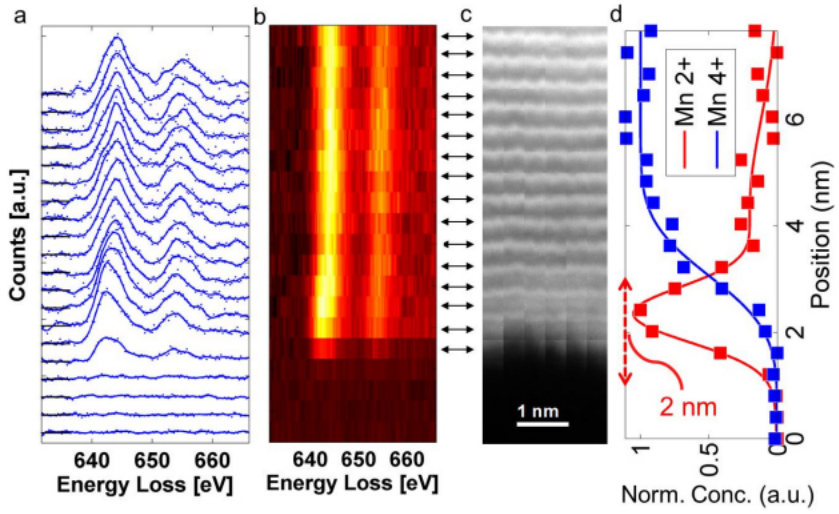

Figure A.9: NMC particles with 20 cycles. EELS line scan profile for an NMC particle along the <001> direction: (a) Mn L-edge EELS spectra along the scanning pathway, (b) 2D EELS map, (c) the simultaneously acquired subpixel mosaic ADF-STEM image, and (d) concentration profiles for Mn^{2+} and Mn^{4+} using a linear combination method. The measurements were performed on electrodes in the discharged state after 20 cycles between a voltage range of 2.0 V- 4.3 V vs Li/Li^{+} .

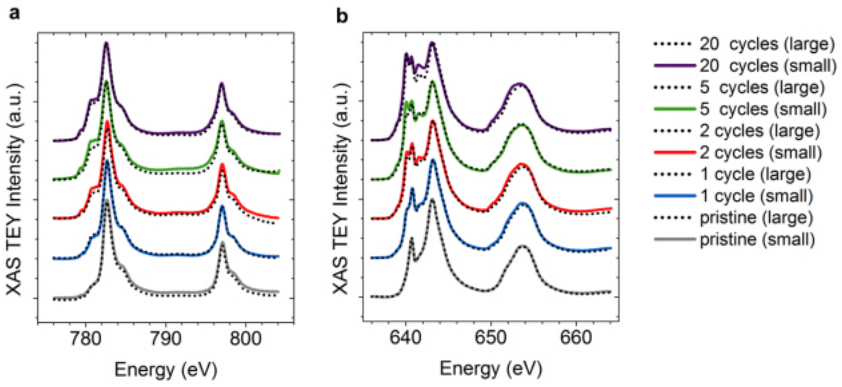

Figure A.10: Buildup of surface reduced layer dependent on particle. Comparison of XAS/TEY spectra for NMC materials with two different particle sizes after various numbers of charge-discharge cycles: (a) Co L-edge and (b) Mn Ledge.

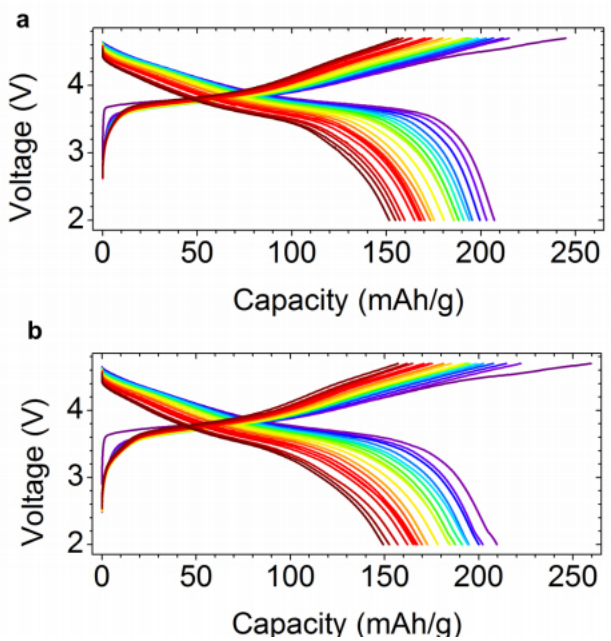

Figure A.11: Comparison of charge-discharge profiles for different particle sizes. Charge-discharge profiles of lithium cells containing (a) NMC material with large particle size. (b) NMC materials with small particle size between 2.0-4.7 V for 20 cycles at a rate of C/20. Note that (a) is also presented in Fig. 2a.

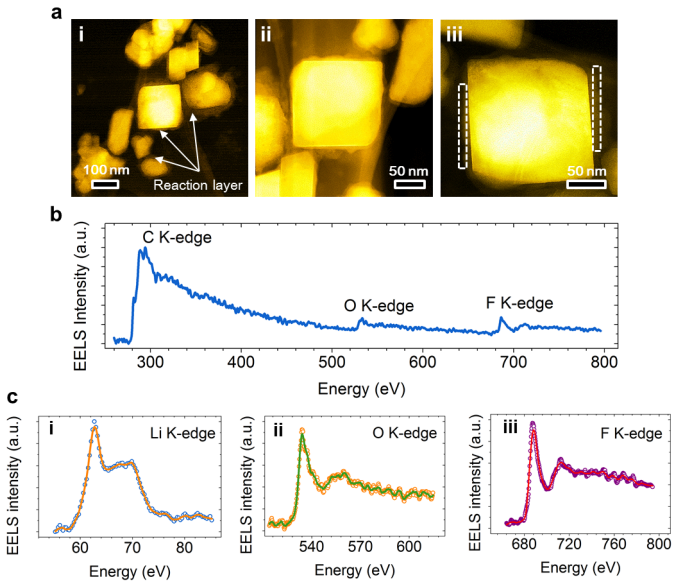

Figure A.12: Investigation of the surface reaction layer for NMC particles cycled twenty times between 2.0 V- 4.7 V vs Li/Li+ and rinsed completely with DMC. (a) STEM images of NMC particles showing the surface reaction layer indicated by arrows in the images. (b) A broad EELS spectrum from 260 eV to 800 eV, where C, O and F are the major elements detected in the range for the surface reaction layer. (c) High-resolution (i) Li K-edge, (ii) O K-edge and (iii) F K-edge spectra suggest that the dominant inorganic species of the surface reaction layer is LiF.

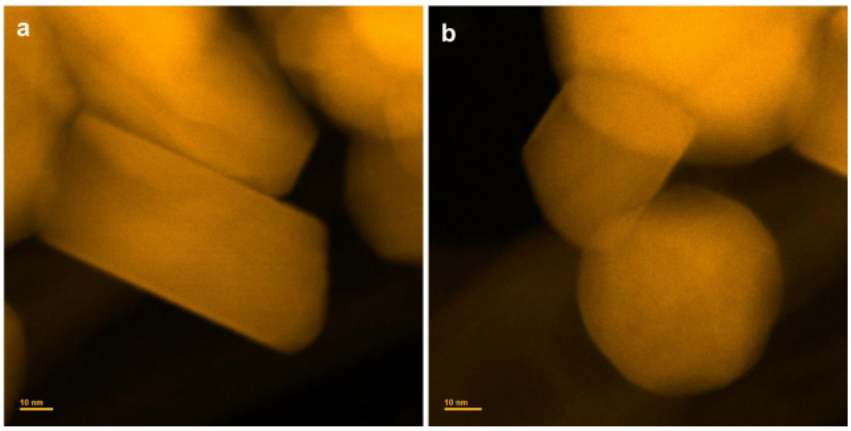

Figure A.13: Surface reaction layer after low-voltage cycling. STEM images of NMC particles cycled twenty times between 2.0 V- 4.3 V vs Li/Li^+ and rinsed completely with DMC.

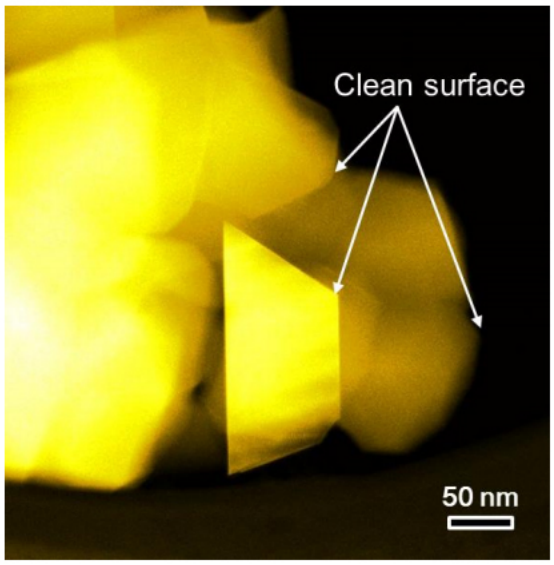

Figure A.14: NMC particles after exposure to electrolytic solution. STEM images of NMC particles after being exposed to the electrolytic solution (1 M $LiPF_6$ in EC-DMC) for 7 days and rinsed completely with DMC.

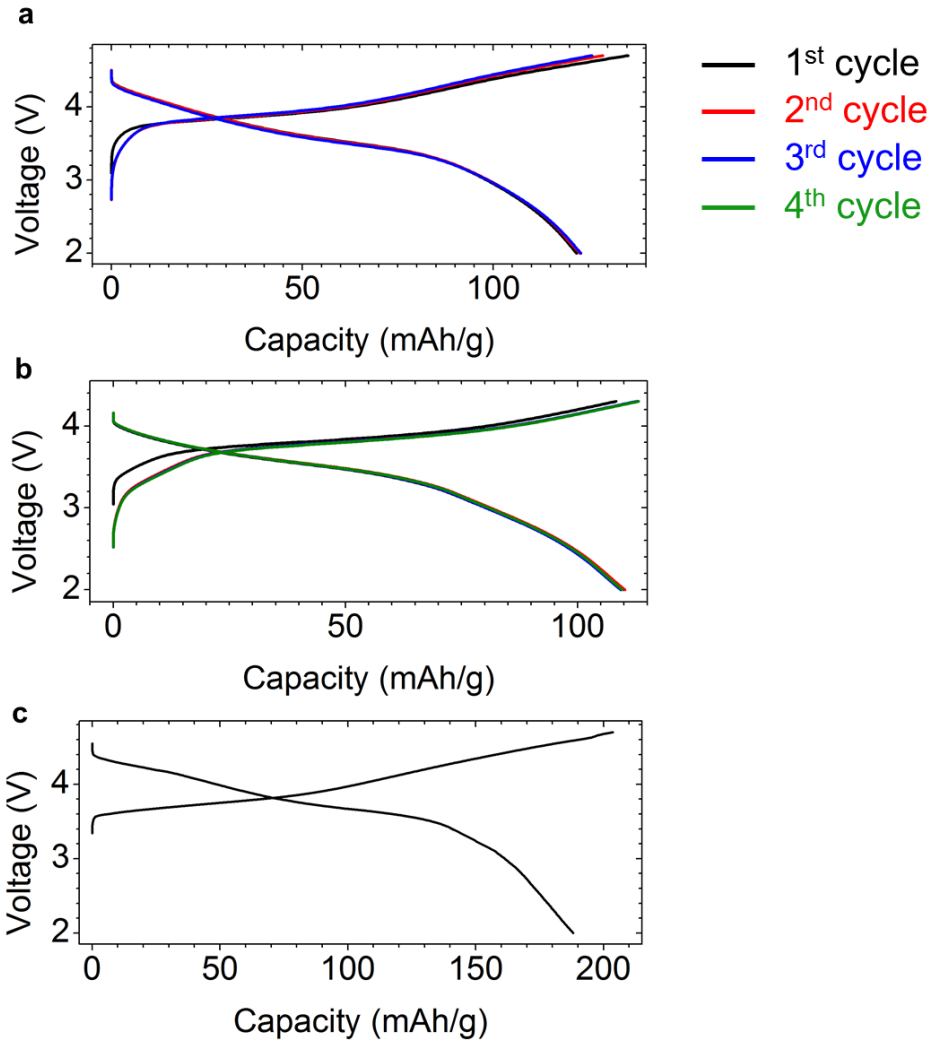

Figure A.15: (a) Charge-discharge profiles (2.0-4.7 V vs. Li/Li^+ at C/20) after 20 high-voltage cycles and after being refreshed with new electrolytic solution. (b) Charge-discharge profiles (2.0-4.3 V vs. Li/Li+ at C/20) after 20 high-voltage cycles. (c) Charge-discharge profile (2.0-4.7 V vs. Li/Li^+ at C/50) after 20 high-voltage cycles. Note that the impedance rise imposed less effect on the capacity when the electrode was cycled at the extremely slow rate, such as C/50.

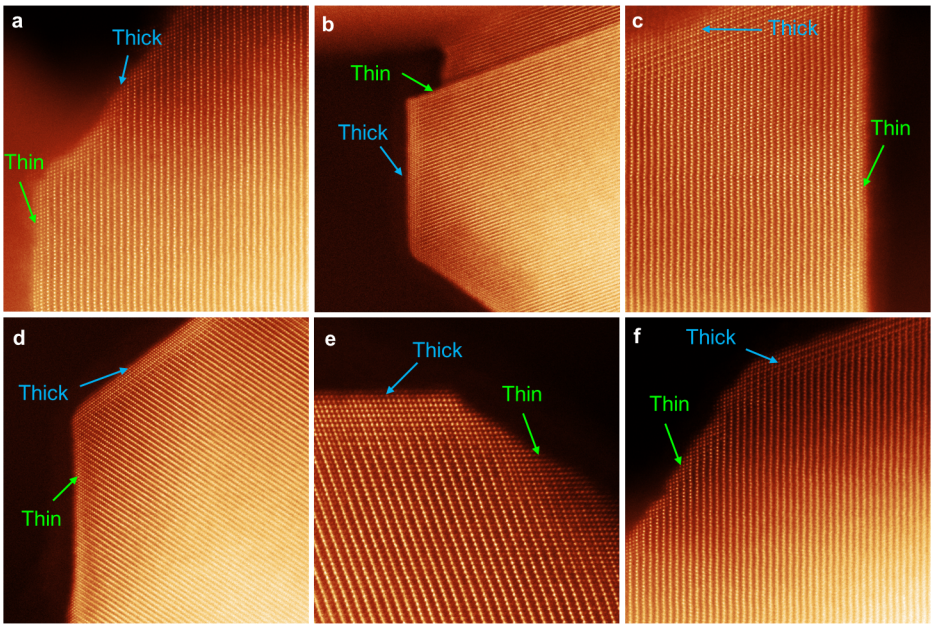

Figure A.16: Atomic resolution ADF/STEM images of NMC particles with orientation-dependent characteristics. The blue and green arrows indicate the thick and thin surface reconstruction layers, respectively. Some thin regions are completely free of reconstruction layer, for example, the thin regions in (b) and (c).

Appendix B

B.1 Determination of Hubbard U Parameter Values

In order to determine a suitable set of U values for the current DFT+U calculations we employed a semi-empirical approach involving the matching of calculated lithium intercalation voltages to experimental measurements. The measurements used in this work exhibit the order also reported in the literature of Ni^{2+}/Ni^{3+}, Ni^{3+}/Ni^{4+}, and Co^{3+}/Co^{4+} [155, 168, 230]. The initial set of U values were taken from the literature on single metal oxide Li intercalation compounds [167] and subsequently optimized by iteratively calculating the voltage profile as described in the literature [199, 231] . Figure 1 shows the lithium intercalation voltage for pure GGA and GGA using different values for the Hubbard-U parameters. As expected the pure GGA values (black line) underestimate intercalation voltages by approximately 1 volt. The red curve which made use of Hubbard-U parameter values of U=7.5 eV for Ni, 3.5 eV for Co and 3.4 eV for Mn, taken from average literature values for multiple oxidation states [167]. These values were in close agreement to experimental curves but Co was the first redox center to oxidize, contrary to computational and experimental findings previously reported[155, 168]. This was likely due to the high U value given to Ni electrons. The green curve was obtained in calculations where the U parameter for Co was increased to bind more strongly its electrons. This calculation did not give the correct oxidation order. The blue and purple lines gave the correct order of oxidation, with the latter being slightly closer to experimental results.

An exact matching of calculated and measured intercalation voltage profiles was not possible due to the high number of degrees of freedom. It should be noted that the main result, that Ti substitution decreased the intercalation voltage, was seen in all of the calculations, using the different sets of Hubbard-U parameters listed above.

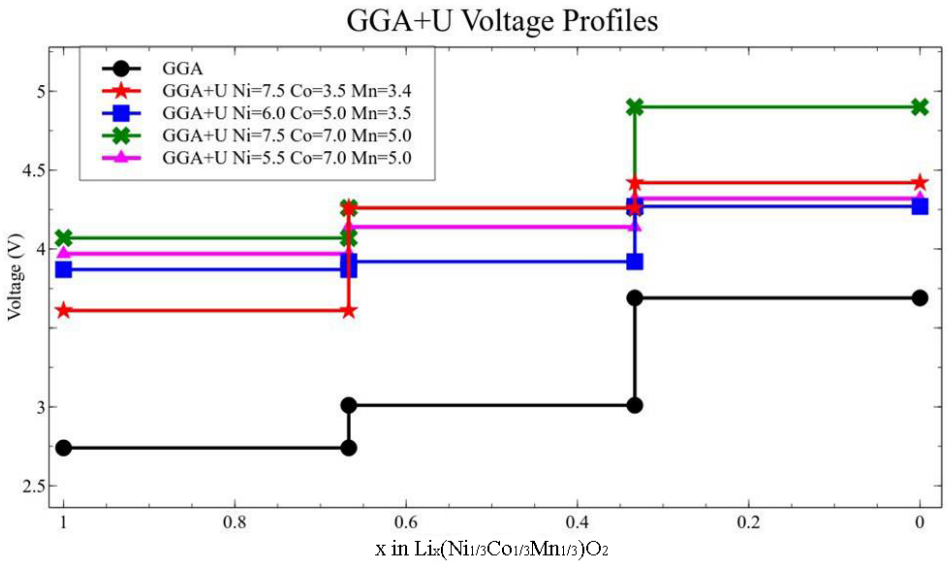

a)

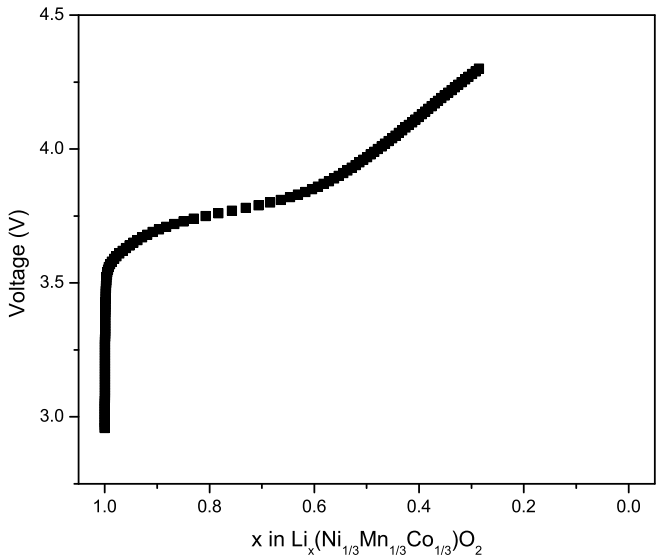

b)

Figure B.1: a) Calculate lithium intercalation voltages for GGA and GGA+U using different sets of Hubbard U values for Ni, Mn and Co. b) Experimental quasi-equilibrium voltage obtained by integrating data from a stepped potential experiment.

Appendix C

C.1 Computational Details

All calculations were performed with the GAMESS-US3 computational chemistry package. Geometry optimizations were performed with the dispersion-corrected B3LYP-D3 density functional method with the 6-311+G(2d,p) basis set. All reactions were performed with the IEF-PCM method in DCM solvent (ϵ=8.93) as a representative of DME (ϵ=7.2). Only vibrational free energy corrections to the electronic energy at the experimental temperature (298 K) were used in accordance with recommendations for molecules optimized in an implicit solvent. Normal modes of all structures were examined to verify that their ground states possess no imaginary frequencies and that transition structures possess only one imaginary frequency corresponding to bond formation or bond breaking.

C.2 Optimized Cartesian Coordinates and Energy of Reactants and Intermediates

INT-1 E [6-311+G(2d,p); Hartrees] = -1993.8333285249
Gvib [kcal/mol] = 39.144
Li 2.28599279 -1.93845092 -0.72217048
O 3.29051772 -1.68767302 -2.18705045
O 1.77865326 -1.88111656 -2.44236175
C 0.47861607 0.88735019 -1.73898409
S -0.25962430 -0.55980680 -0.70426118
O 0.77413917 -1.02880467 0.19108457
O -1.04578125 -1.39359834 -1.56230785
N -1.38534771 0.22250036 0.27444552
C -1.22897913 0.00760157 3.01353427
S -1.04761880 1.22032779 1.57945464
O 0.33074682 1.61323313 1.52794373
O -2.14295692 2.14187384 1.68597785

F -1.00909830 0.67420348 4.14085226
F -2.46155702 -0.48538287 3.01125957
F -0.34861246 -0.97344856 2.88812420
F -0.16456712 2.01040516 -1.43842569
F 1.76049776 1.01538751 -1.44661209
F 0.31871662 0.62959296 -3.02742414
H -2.33087750 0.28826016 -0.10300471
Li 2.62895058 -0.86237912 -3.60938063

INT-2 CF3
E [6-311+G(2d,p); Hartrees] = -1993.9460153419
Gvib [kcal/mol] = 35.962
Li 0.82554251 -0.78496710 -0.45479157
O 2.75920295 0.69260634 -1.38509734
O 2.33484932 -0.71011912 -1.56200429
C 2.20956846 1.40050740 -2.37439617
S -2.06972363 -1.93180725 -0.57099879
O -0.59237491 -2.03392874 -0.60457151
O -2.68968633 -2.85378828 0.37285079
N -2.24635777 0.01468606 0.49105192
C -0.99749284 -0.15423109 2.97507771
S -1.15478464 0.75101698 1.33537529
O 0.16474343 0.51522025 0.73651633
O -1.47941526 2.10962130 1.72864075
F -0.08420486 0.43607278 3.75210947
F -2.17340932 -0.15031198 3.61334936
F -0.62781581 -1.42169701 2.76411174
F 0.87153645 1.39862387 -2.38835273
F 2.64913855 2.64605566 -2.31519558
F 2.58894850 0.88310309 -3.61946567
H -3.19570505 0.25071793 0.77821817
Li 2.90744025 -1.05738110 -3.27242788

INT-2 N-S
E [6-311+G(2d,p); Hartrees] = -1993.8878898133
Gvib [kcal/mol] = 37.836
Li 0.51967617 -0.09679032 0.28999350
O 1.98885108 -0.25654871 -0.98434872
O 1.83904944 -1.46581220 -1.83049419
C 0.04575021 0.03057650 -3.21821672
S 0.28993078 -1.57070848 -2.21519907
O -0.51264800 -1.41977108 -1.02212782

O 0.15168663 -2.69278321 -3.09469974
N -0.78869187 1.26412992 1.01657912
C -1.32955917 0.00224418 3.43544670
S -0.17410495 1.09134528 2.42467102
O 0.98536514 0.18681554 2.23823404
O 0.00067334 2.25016512 3.29166048
F -0.79969647 -0.29637196 4.62955988
F -2.50068155 0.62553491 3.63753717
F -1.57202454 -1.14512123 2.78435042
F -0.89651803 -0.18586861 -4.12298152
F -0.31824432 1.01286747 -2.41047372
F 1.18806321 0.35145421 -3.83196464
H -1.49058841 1.99771547 0.96667433
Li 3.37200484 0.31702998 -1.98616603

Li2O2
E [6-311+G(2d,p); Hartrees] = -165.5996989162
Gvib [kcal/mol] = 3.348
Li 0.71814632 -1.42867265 -0.00005788
O -0.69260745 -0.34799783 0.00016270
O 0.69250737 0.34793230 -0.00002101
Li -0.71804624 1.42873819 -0.00008381

LiNHSO2CF3
E [6-311+G(2d,p); Hartrees] = -949.4178699511
Gvib [kcal/mol] = 22.345
Li 0.04902787 -0.50899981 -0.37818804
N -1.66993736 0.03316625 0.35821126
C -1.15278751 -0.22158253 3.08038472
S -0.92440943 0.77326920 1.50040764
O 0.51617305 0.55059465 1.20819953
O -1.34465071 2.10762907 1.89331626
F -0.46312990 0.31514502 4.09307281
F -2.45010114 -0.25143999 3.41531794
F -0.73263024 -1.48042526 2.89974507
H -2.66331197 0.24254956 0.30981341

LiO2SO2CF3
E [6-311+G(2d,p); Hartrees] = -1044.4425344701
Gvib [kcal/mol] = 16.084
O 2.49705981 -1.04254587 -1.16412311
O 1.56960868 -1.92614795 -1.91231404

C 0.17739521 0.34835729 -2.41617561
S 0.08088717 -1.40954766 -1.68701671

TFSI
E [6-311+G(2d,p); Hartrees] = -1828.2157391357
Gvib [kcal/mol] = 34.847
C 1.42068912 -0.57497751 -1.32170084
S 0.47426238 -1.54876628 -0.01339069
O 1.41213214 -2.45954664 0.57901012
O -0.76821157 -1.94655800 -0.60346479
N 0.19522588 -0.35819125 1.14122313
C -2.32325666 -0.31488127 2.28879310
S -1.10967171 0.69472868 1.25668536
O -0.66764120 1.77223147 2.09561660
O -1.69810650 0.87260478 -0.03621344
F -3.37794334 0.45141429 2.53795388
F -2.69265537 -1.39593415 1.61894137
F -1.73804469 -0.66716461 3.42789232
F 2.52631277 -0.07806041 -0.78034087
F 1.73287638 -1.40867447 -2.30614770
F 0.66104646 0.40813424 -1.78162106
H 0.88146391 -0.29514930 1.89304256

TS1-CF3
E [6-311+G(2d,p); Hartrees] = -1993.8056445610
Gvib [kcal/mol] = 37.903
Number of imaginary frequencies: 1 [189.63 cm^{-1}]
Li 2.06812313 -1.92222122 -0.22561639
O 2.27013022 -0.78020044 -1.74577572
O 1.31070273 -1.77970108 -1.98084499
C 1.05382796 0.97688750 -1.80993656
S -0.29042076 -0.84149857 -0.76245144
O 0.40846910 -1.39985024 0.43394615
O -1.37447237 -1.62787303 -1.36100157
N -1.36170830 0.37343945 0.09988290
C -1.02585310 -0.10177111 2.88441171
S -0.97229286 1.16343772 1.45586439
O 0.40215031 1.59285825 1.38573140
O -2.04807508 2.07965484 1.76605288
F -1.47597758 0.51578521 3.98069849
F -1.85820253 -1.09969921 2.58198155
F 0.18069848 -0.59211462 3.14169676

F 0.08768817 1.85908365 -1.53928319
F 2.18999473 1.61448346 -1.55112510
F 0.93839121 0.74357620 -3.16155705
H -2.35484519 0.19850248 -0.03489705
Li 1.85167173 -0.97277924 -3.55777718

TS1-NS
E [6-311+G(2d,p); Hartrees] = -1993.8323680408
Gvib [kcal/mol] = 38.621
Number of imaginary frequencies: 1 [37.76 cm^{-1}]
Li 2.31426418 -1.99374376 -0.64866417
O 3.08350627 -1.46048808 -2.17173849
O 1.58316228 -1.73941672 -2.29713961
C 0.52993793 0.87137612 -1.72031043
S -0.16046588 -0.63003922 -0.72894620
O 0.81542347 -1.07643406 0.24801858
O -0.99763910 -1.45121874 -1.55733984
N -1.32451725 0.16314691 0.25412933
C -1.24467691 0.01604196 2.99218465
S -1.00911573 1.18274240 1.53219346
O 0.37475151 1.56578533 1.52999397
O -2.09285680 2.12554453 1.60008721
F -1.04712175 0.71117844 4.10892136
F -2.48396932 -0.46392838 2.97543260
F -0.37581141 -0.98276105 2.92688116
F -0.16075477 1.96505534 -1.40123637
F 1.79680108 1.04297670 -1.40988444
F 0.38395045 0.66025141 -3.02288444
H -2.23519162 0.30094951 -0.18377072
Li 2.35478537 -0.92550912 -3.68771976

C.3 NMR Results

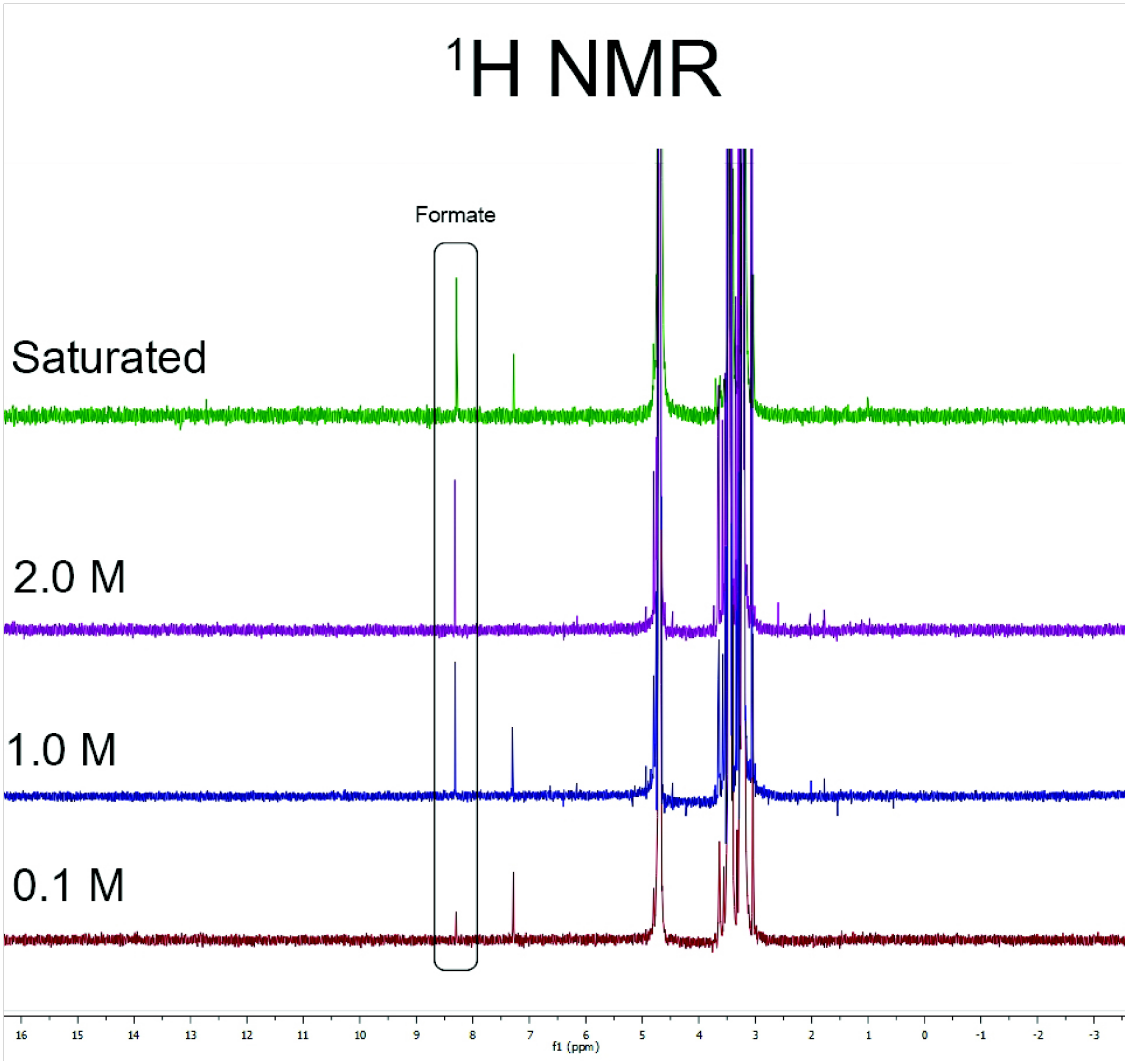
^{1}H NMR
Formate
Saturated
2.0 M
1.0 M
0.1 M
16 15 14 13 12 11 10 9 8 7 6 5 4 3 2 1 0 -1 -2 -3
f1 (ppm)

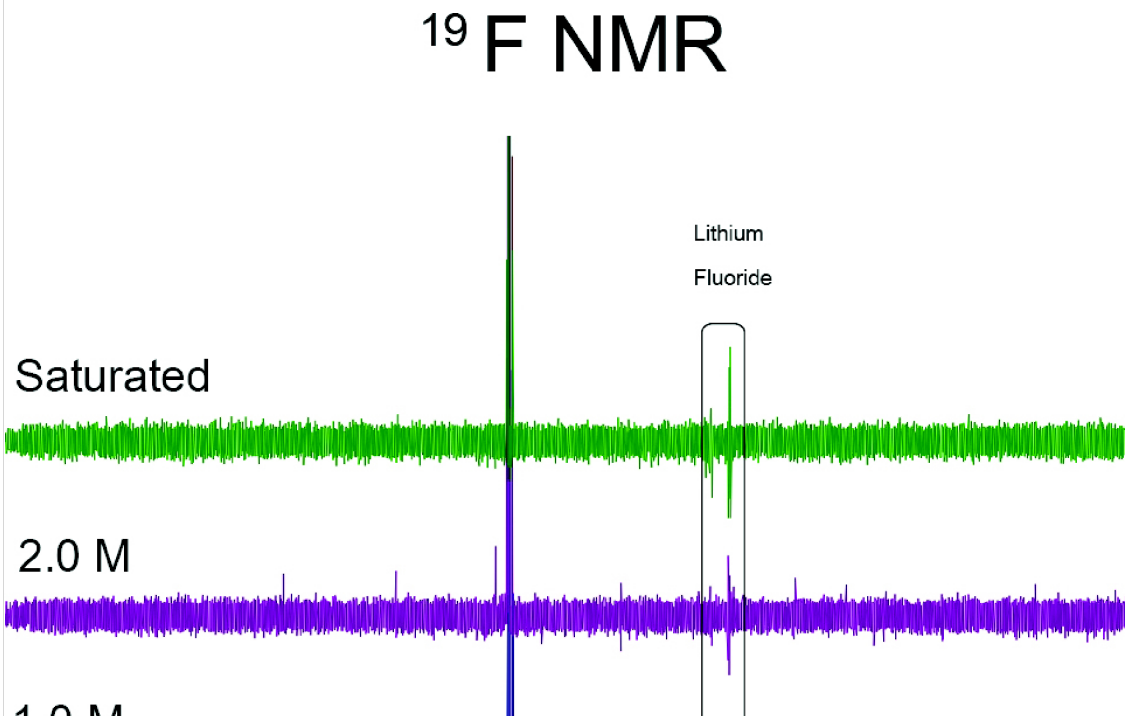
^{19}F NMR
Lithium
Fluoride
Saturated
2.0 M

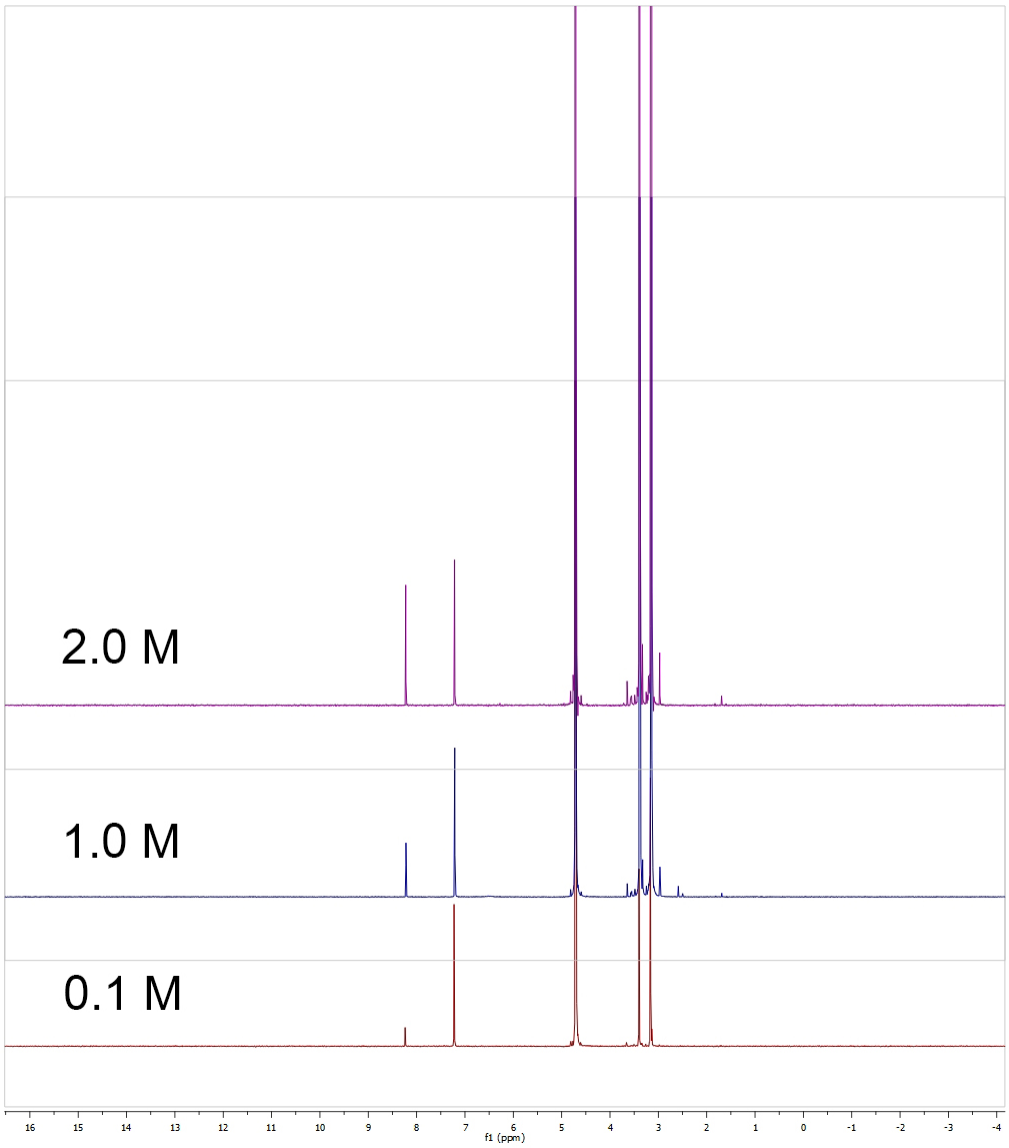

Figure C.2: ^{1}H NMR spectra from cells with different electrolyte concentrations discharged at a current rate of 200 μA. Left most peak correspond to lithium formate followed by benzene reference peak. Cells were discharged at constant pressure until sudden death with a voltage cutoff of 1.5 V.

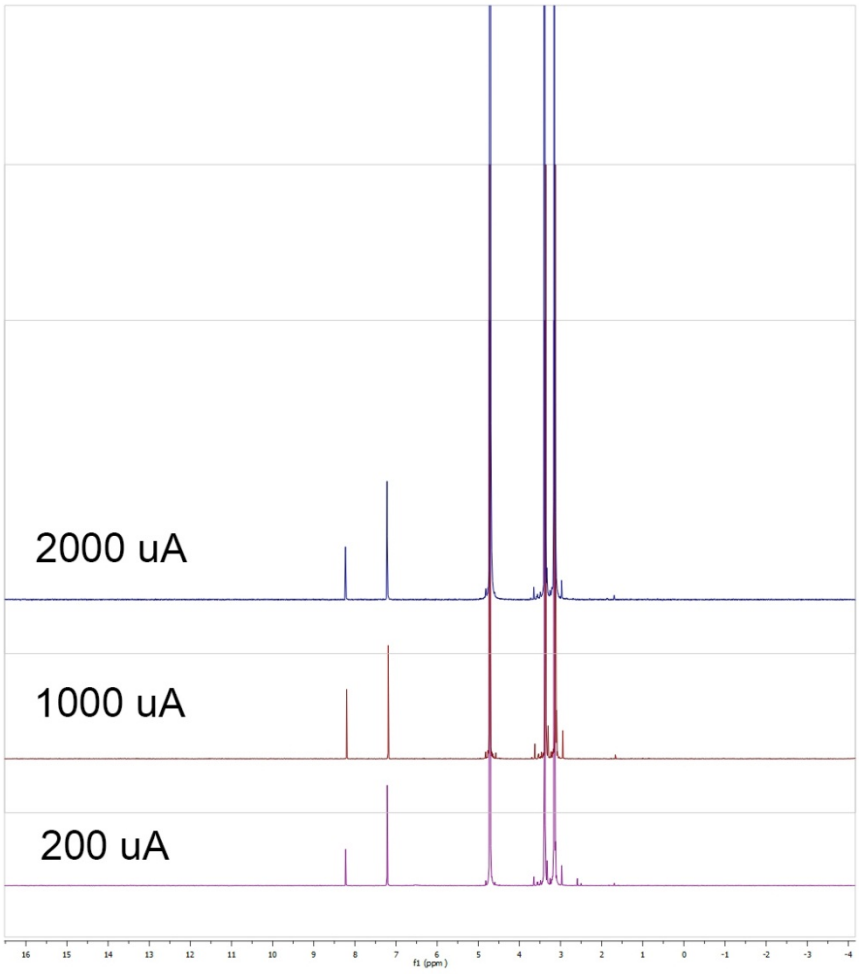

Figure C.3: ^{1}H NMR spectra from cells with an electrolyte concentration of 1.0 M discharged at different current rates. Left most peak correspond to lithium formate followed by benzene reference peak. Cells were discharged at constant pressure until sudden death with a voltage cutoff of 1.5 V.

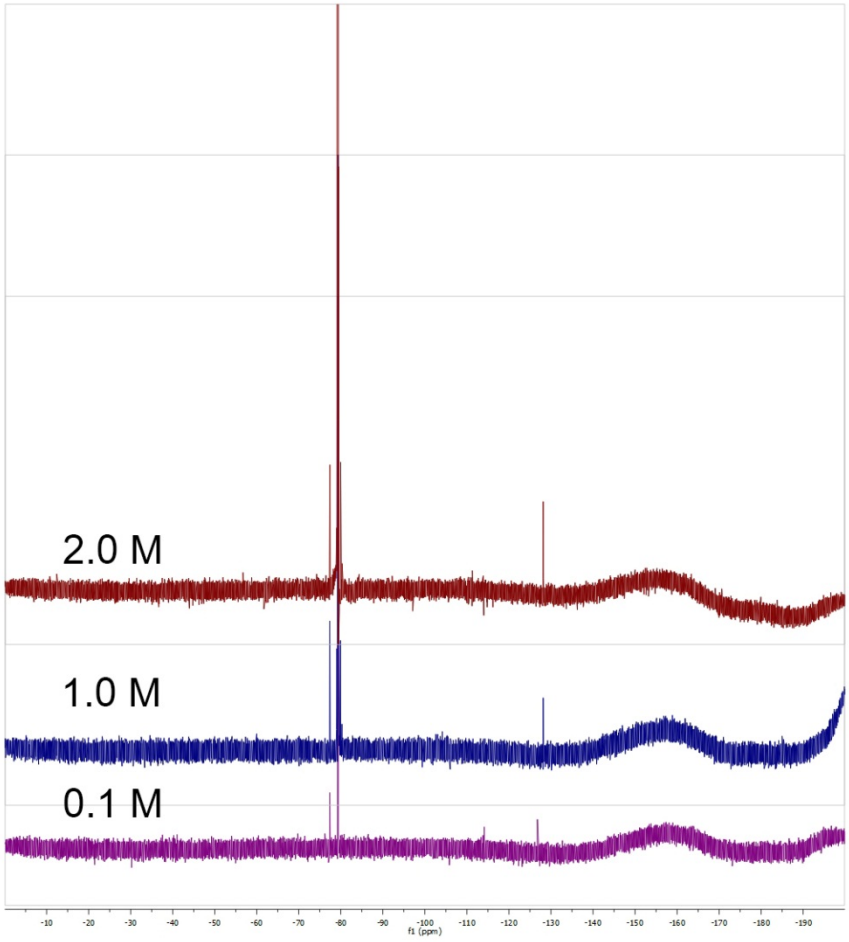

Figure C.4: ^{19}F NMR spectra from cells with different electrolyte concentration discharge at a current rate of 200 μA. The cells were discharged at constant volume up to a capacity of 1mAh .

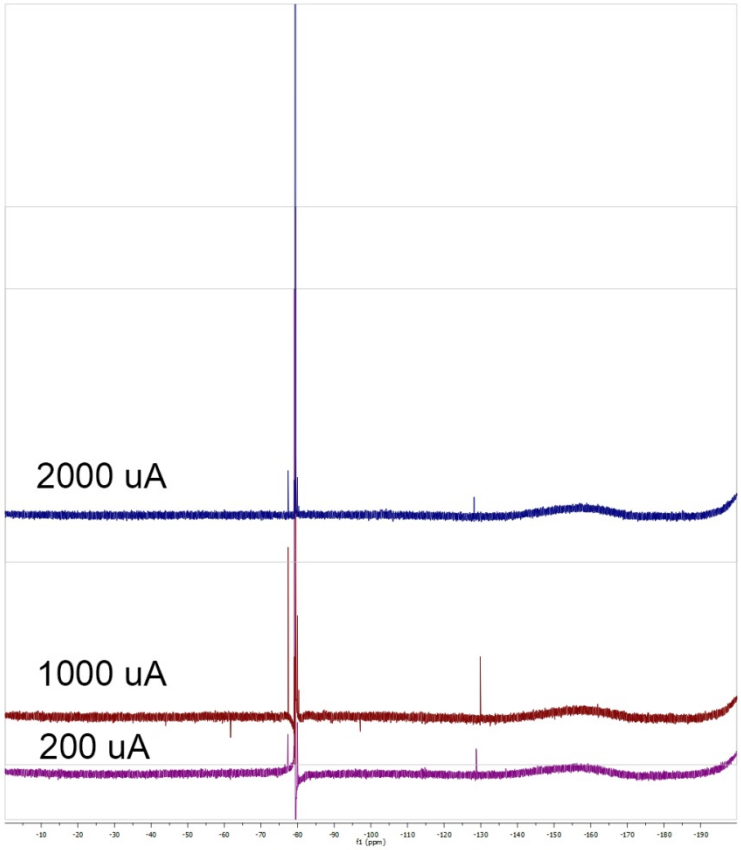

Figure C.5: ^{19}F NMR spectra from cells with an electrolyte concentration of 1.0 M discharge at different current rates. Cells were discharged at constant pressure until sudden death with a voltage cutoff of 1.5 V.

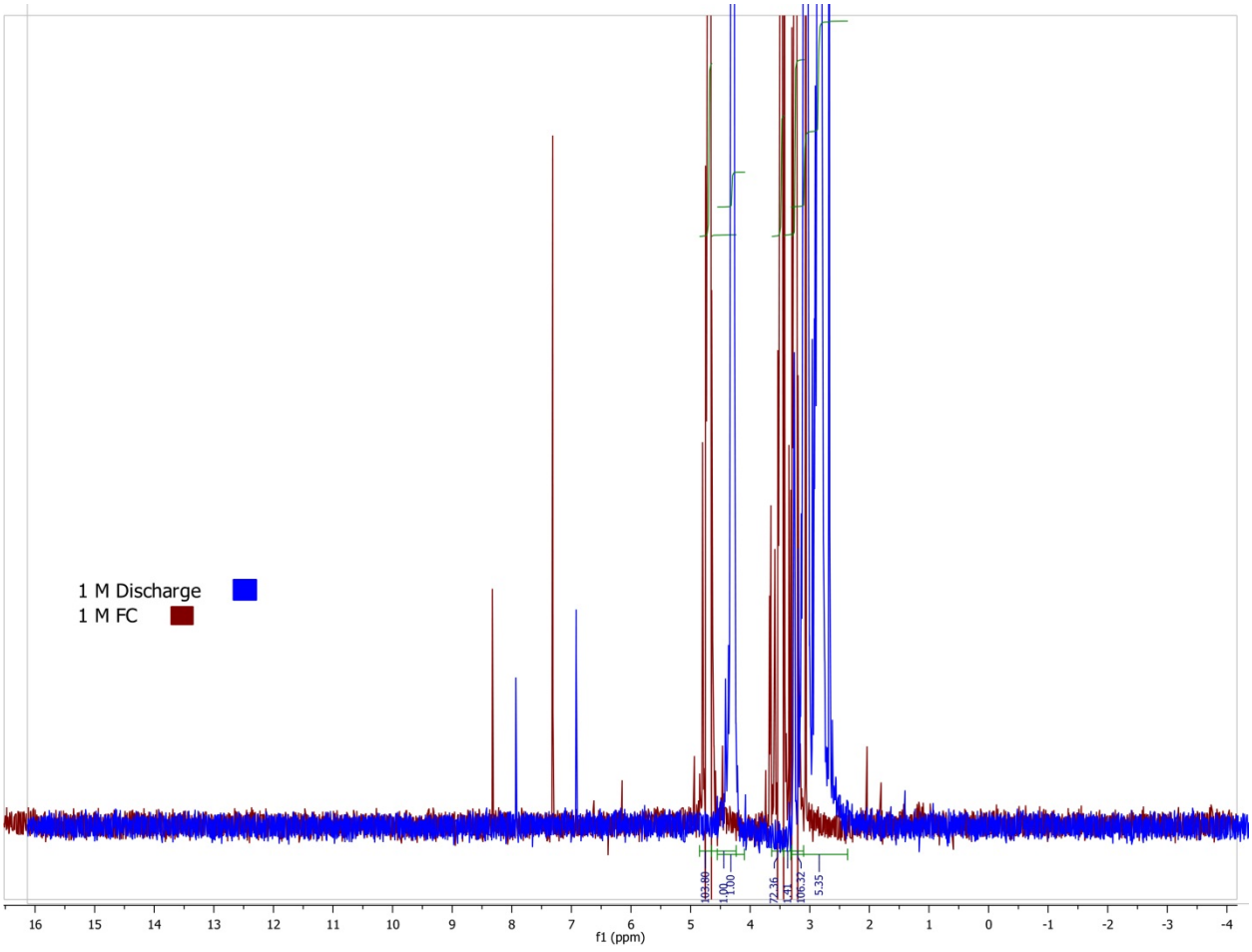

Figure C.6: ^{1}H NMR Spectra of Cells with 1.0 M electrolyte concentration that was discharged at constants volume at 500 μA for 4 hours (blue line - discharge) and cell that was discharged and recharged at 200 μA for 5 hours each (red line - FC). The discharge NMR is shifted by 0.5 ppm for easier comparison. The peaks with asterisk correspond to benzene standard, discrepancy arises from problems with mixing benzene with sample.

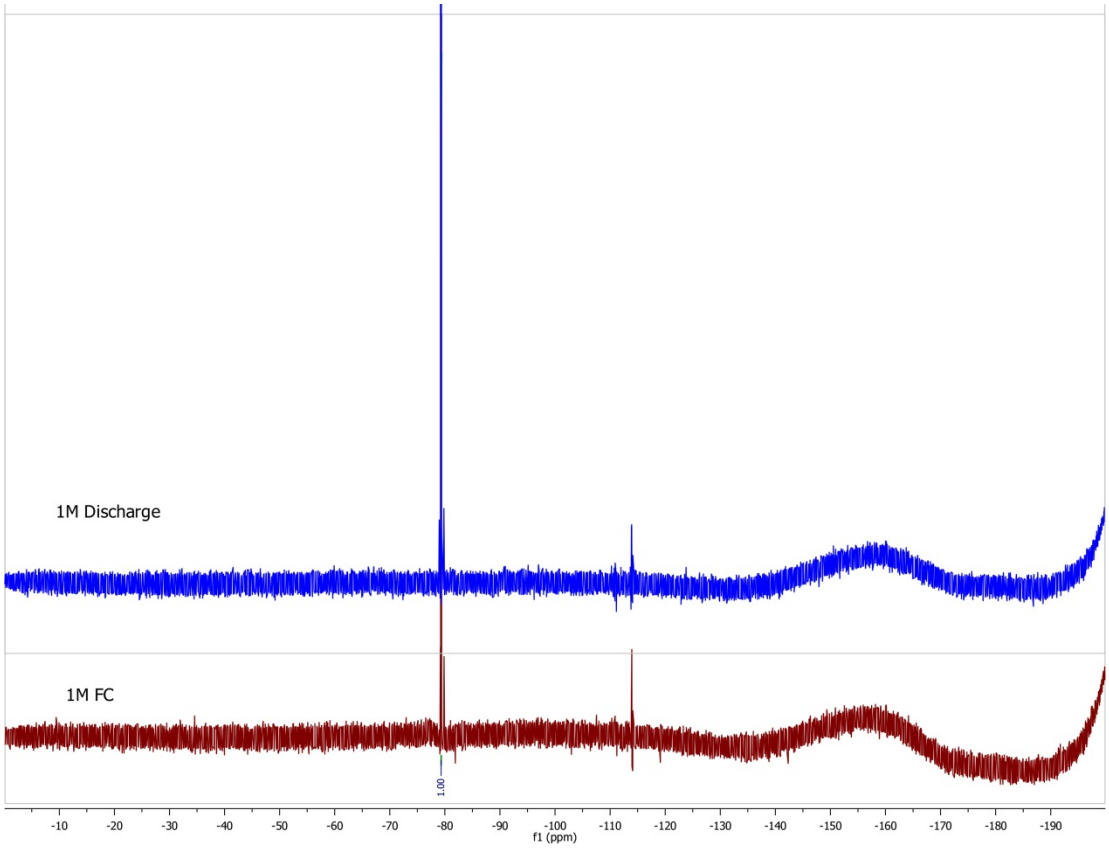

Figure C.7: ^{19}F NMR Spectra of cells with an electrolyte concentration of 1.0 M that was discharged at constants volume at 500 μA for 4 hours (blue line - Discharge) and cell that was discharged and recharged at 200 μA for 5 hours each (red line - FC).

Bibliography

[1] Intergovernmental Panel on Climate Change. *Climate Change 2007 Synthesis Report*. 2008, p. 104. ISBN: 9291691224.

[2] U.S. Department of Energy. "Grid Energy Storage". In: December (2013), p. 67.

[3] United States Department of Energy. *Annual Energy Outlook 2015*. 2015. ISBN: 0160829712.

[4] Energy Information Administration. *Annual Energy Review, 2007*. 2008. ISBN: 2025861680.

[5] S.M. Schoenung and W.V. Hassenzahl. "Long- vs . Short-Term Energy Storage Technologies Analysis A Life-Cycle Cost Study A Study for the DOE Energy Storage Systems Program". In: *Power Qual.* SAND2011-2.August (2003), p. 84.

[6] P. Hohenberg and W. Kohn. "Inhomogeneous Electron Gas". In: *Phys. Rev.* 136 (3B 1964), B864–B871.

[7] W. Kohn and L. J. Sham. "Self-Consistent Equations Including Exchange and Correlation Effects". In: *Phys. Rev.* 140 (4A 1965), A1133–A1138.

[8] M. Saiful Islam and Craig A. J. Fisher. "Lithium and sodium battery cathode materials: computational insights into voltage, diffusion and nanostructural properties". In: *Chem. Soc. Rev.* 43 (1 2014), pp. 185–204.

[9] Lorenzo Malavasi, Craig A. J. Fisher, and M. Saiful Islam. "Oxide-ion and proton conducting electrolyte materials for clean energy applications: structural and mechanistic features". In: *Chem. Soc. Rev.* 39 (11 2010), pp. 4370–4387.

[10] John Newman and Karen Thomas-Alyea. *Electrochemical Systems*. 3rd ed. John Wiley Sons, 2004. ISBN: 0471477567.

[11] R. Mark Ormerod. "Solid oxide fuel cells". In: *Chem. Soc. Rev.* 32 (1 2003), pp. 17–28.

[12] Daniel J. L. Brett et al. "Intermediate temperature solid oxide fuel cells". In: *Chem. Soc. Rev.* 37 (8 2008), pp. 1568–1578.

[13] T Norby. "The promise of protonics." In: *Nature* 410.6831 (2001), pp. 877–878. ISSN: 0028-0836.

[14] Megan E. Scofield, Haiqing Liu, and Stanislaus S. Wong. "A concise guide to sustainable PEMFCs: recent advances in improving both oxygen reduction catalysts and proton exchange membranes". In: *Chem. Soc. Rev.* 44 (16 2015), pp. 5836–5860.

[15] Emiliana Fabbri, Daniele Pergolesi, and Enrico Traversa. “Materials challenges toward proton-conducting oxide fuel cells: a critical review”. In: *Chem. Soc. Rev.* 39 (11 2010), pp. 4355–4369.

[16] Truls Norby. “Solid-state protonic conductors: principles, properties, progress and prospects”. In: *Solid State Ionics* 125.14 (1999), pp. 1 –11. ISSN: 0167-2738.

[17] M. S. WHITTINGHAM. “Electrical Energy Storage and Intercalation Chemistry”. In: *Science* 192.4244 (1976), pp. 1126–1127. ISSN: 0036-8075. eprint: http://science.sciencemag.org/content/192/4244/1126.full.pdf.

[18] K. Mizushima et al. “LixCoO2 (0¡x¡1): A new cathode material for batteries of high energy density”. In: *Solid State Ionics* 3-4.C (1981), pp. 171–174. ISSN: 01672738.

[19] M Armand and J-M Tarascon. “Building Better Batteries.” In: *Nature* 451.7179 (2008), pp. 652–657.

[20] Michael D. Slater et al. “Sodium-Ion Batteries”. In: *Advanced Functional Materials* 23.8 (2013), pp. 947–958. ISSN: 1616-3028.

[21] Brian L. Ellis, Kyu Tae Lee, and Linda F. Nazar. “Positive Electrode Materials for Li-Ion and Li-Batteries”. In: *Chemistry of Materials* 22.3 (2010), pp. 691–714.

[22] Cheol-Min Park et al. “Li-alloy based anode materials for Li secondary batteries”. In: *Chem. Soc. Rev.* 39 (8 2010), pp. 3115–3141.

[23] Elmira Memarzadeh Lotfabad et al. “High-Density Sodium and Lithium Ion Battery Anodes from Banana Peels”. In: *ACS Nano* 8.7 (2014). PMID: 24897543, pp. 7115–7129. DOI: 10.1021/nn502045y. eprint: http://dx.doi.org/10.1021/nn502045y. URL: http://dx.doi.org/10.1021/nn502045y.

[24] Jia Ding et al. “Carbon Nanosheet Frameworks Derived from Peat Moss as High Performance Sodium Ion Battery Anodes”. In: *ACS Nano* 7.12 (2013). PMID: 24191681, pp. 11004–11015. DOI: 10.1021/nn404640c. eprint: http://dx.doi.org/10.1021/nn404640c. URL: http://dx.doi.org/10.1021/nn404640c.

[25] Shinichi Komaba et al. “Electrochemical Na Insertion and Solid Electrolyte Interphase for Hard-Carbon Electrodes and Application to Na-Ion Batteries”. In: *Advanced Functional Materials* 21.20 (2011), pp. 3859–3867. ISSN: 1616-3028. DOI: 10.1002/adfm.201100854. URL: http://dx.doi.org/10.1002/adfm.201100854.

[26] Sung-Wook Kim et al. “Electrode Materials for Rechargeable Sodium-Ion Batteries: Potential Alternatives to Current Lithium-Ion Batteries”. In: *Advanced Energy Materials* 2.7 (2012), pp. 710–721. ISSN: 1614-6840.

[27] Nian Liu et al. “A Yolk-Shell Design for Stabilized and Scalable Li-Ion Battery Alloy Anodes”. In: *Nano Letters* 12.6 (2012). PMID: 22551164, pp. 3315–3321. DOI: 10.1021/nl3014814. eprint: http://dx.doi.org/10.1021/nl3014814. URL: http://dx.doi.org/10.1021/nl3014814.

[28] Youngjin Kim et al. "High-Capacity Anode Materials for Sodium-Ion Batteries". In: *Chemistry A European Journal* 20.38 (2014), pp. 11980–11992. ISSN: 1521-3765. DOI: 10.1002/chem.201402511. URL: http://dx.doi.org/10.1002/chem.201402511.

[29] Charles de las Casas and Wenzhi Li. "A review of application of carbon nanotubes for lithium ion battery anode material". In: *Journal of Power Sources* 208 (2012), pp. 74 –85. ISSN: 0378-7753.

[30] Bote Zhao et al. "A comprehensive review of Li4Ti5O12-based electrodes for lithium-ion batteries: The latest advancements and future perspectives". In: *Materials Science and Engineering: R: Reports* 98 (2015), pp. 1 –71. ISSN: 0927-796X.

[31] Bryan D. McCloskey et al. "Mechanistic insights for the development of Li-O_2 battery materials: addressing Li_2O_2 conductivity limitations and electrolyte and cathode instabilities". In: *Chem. Commun.* 51 (2015), pp. 12701–12715. ISSN: 1359-7345.

[32] Alan C. Luntz and Bryan D. McCloskey. "Nonaqueous Li air batteries: A status report". In: *Chemical Reviews* 114.23 (2014). PMID: 25376975, pp. 11721–11750.

[33] Jun Lu and Khalil Amine. "Recent research progress on non-aqueous lithium-air batteries from Argonne National Laboratory". In: *Energies* 6.11 (2013), pp. 6016–6044. ISSN: 19961073.

[34] Peter G Bruce et al. "Li-O2 and Li-S batteries with high energy storage". In: *Nat Mater* 11.1 (Jan. 2012), pp. 19–29. ISSN: 1476-1122. URL: http://dx.doi.org/10.1038/nmat3191.

[35] Yuyan Shao et al. "Making Li-air batteries rechargeable: Material challenges". In: *Adv. Funct. Mater.* 23.8 (2013), pp. 987–1004. ISSN: 1616301X.

[36] Erwin Schrödinger. "An undulatory theory of the mechanics of atoms and molecules". In: *Physical Review* 28.6 (1926), p. 1049.

[37] Max Born and Robert Oppenheimer. "Zur quantentheorie der molekeln". In: *Annalen der Physik* 389.20 (1927), pp. 457–484.

[38] Walter Kohn and Lu Jeu Sham. "Self-consistent equations including exchange and correlation effects". In: *Physical Review* 140.4A (1965), A1133.

[39] SH Vosko, Ll Wilk, and M Nusair. "Accurate spin-dependent electron liquid correlation energies for local spin density calculations: a critical analysis". In: *Canadian Journal of physics* 58.8 (1980), pp. 1200–1211.

[40] J. P. Perdew and Alex Zunger. "Self-interaction correction to density-functional approximations for many-electron systems". In: *Phys. Rev. B* 23 (10 1981), pp. 5048–5079.

[41] John P Perdew and Yue Wang. "Accurate and simple analytic representation of the electron-gas correlation energy". In: *Physical Review B* 45.23 (1992), p. 13244.

[42] John P Perdew and Wang Yue. "Accurate and simple density functional for the electronic exchange energy: Generalized gradient approximation". In: *Physical review B* 33.12 (1986), p. 8800.

[43] John P Perdew, Kieron Burke, and Matthias Ernzerhof. "Generalized gradient approximation made simple". In: *Physical review letters* 77.18 (1996), p. 3865.

[44] S. L. Dudarev et al. "Electron-energy-loss spectra and the structural stability of nickel oxide: An LSDA+U study". In: *Phys. Rev. B* 57 (3 1998), pp. 1505–1509.

[45] V. Fock. "Näherungsmethode zur Lösung des quantenmechanischen Mehrkörperproblems". In: *Zeitschrift für Physik* 61.1 (), pp. 126–148. ISSN: 0044-3328.

[46] J. C. Slater. "A Simplification of the Hartree-Fock Method". In: *Phys. Rev.* 81 (3 1951), pp. 385–390.

[47] W. J. Hehre, R. Ditchfield, and J. a. Pople. "Selfconsistent molecular orbital methods. XII. Further extensions of Gaussian-type basis sets for use in molecular orbital studies of organic molecules". In: *J. Chem. Phys.* 56.5 (1972), pp. 2257–2261. ISSN: 00219606.

[48] P. C. Hariharan and J. a. Pople. "The influence of polarization functions on molecular orbital hydrogenation energies". In: *Theor. Chim. Acta* 28.3 (1973), pp. 213–222. ISSN: 00405744.

[49] Timothy Clark et al. "Efficient diffuse function-augmented basis sets for anion calculations. III. The 3-21+G basis set for first-row elements, Li-F". In: *J. Comput. Chem.* 4.3 (1983), pp. 294–301. ISSN: 1096-987X.

[50] K Kim and K D Jordan. "Comparison of density functional and Mp2 calculations on the water monomer and dimer". In: *J. Phys. Chem.* 98.40 (1994), pp. 10089–10094. ISSN: 0022-3654.

[51] P Stephens et al. "Ab-initio calculation of vibrational absorption and circular-dichroism spectra using density functional force fields". In: *J. Phys. Chem.* 98.45 (1994), pp. 11623–11627. ISSN: 00223654.

[52] Stefan Grimme et al. "A Consistent and Accurate ab initio Parametrization of Density Functional Dispersion Correction (DFT-D) for the 94 Elements H-Pu". In: *The Journal of Chemical Physics* 132.15, 154104 (2010), pp. –.

[53] Graeme Henkelman, Gísli Jóhannesson, and Hannes Jónsson. "Theoretical methods in condensed phase chemistry". In: *Theor. Methods Condens. Phase Chem. - Prog. Theor. Chem. Phys. - Vol. 5* 5 (2002), pp. 269–302.

[54] George H. Vineyard. "Frequency factors and isotope effects in solid state rate processes". In: *J. Phys. Chem. Solids* 3.1-2 (1957), pp. 121–127. ISSN: 00223697.

[55] Hannes Jónsson, Greg Mills, and Karsten W. Jacobsen. "Nudged elastic band method for finding minimum energy paths of transitions". In: *Class. Quantum Dyn. Condens. Phase Simulations* (1998), pp. 385–404.

[56] Richard E. Gillilan and Kent R. Wilson. “Shadowing, rare events, and rubber bands. A variational Verlet algorithm for molecular dynamics”. In: *The Journal of Chemical Physics* 97.3 (1992).

[57] Graeme Henkelman and Hannes Jnsson. “Improved tangent estimate in the nudged elastic band method for finding minimum energy paths and saddle points”. In: *The Journal of Chemical Physics* 113.22 (2000).

[58] A. Weber. In: *Encyclopedia of Electrochemical Power Sources*. Ed. by Jurgen Garche. Amsterdam: Elsevier, 2009, pp. 120 –134.

[59] T. Norby and N. Christiansen. In: *Solid State Ionics* 77 (1995), pp. 240–243.

[60] K. Amezawa et al. In: *J. Electrochem. Soc.* 145 (1998), pp. 3313–3319.

[61] O. Paschos et al. In: *J. Phys. Condensed Mat.* 23.234140 (2011).

[62] K. D. Kreuer. In: *Annu. Rev. Mat. Res.* 33 (2003), pp. 333–359.

[63] D. Brett et al. In: *Chem. Soc. Rev.* 37.1568 (2008).

[64] E. Kendrick et al. “Cooperative Mechanisms of Fast ion Conduction in Gallium based Oxides with Tetrahedral Moieties”. In: *Nat. Mater* 6.11 (2007), pp. 871–875.

[65] Truls Norby. “Solid-State Protonic Conductors: Principles, Properties, Progress and Prospects”. In: *Solid State Ionics* 125.14 (1999), pp. 1 –11.

[66] A. Atkinson et al. *Advanced Anodes for High-temperature Fuel Cells*. 2004.

[67] H. Iwahara. In: *Solid State Ionic Devices* 102 (2001).

[68] J.-S. Zhou and J. B. Goodenough. “Universal Octahedral-Site Distortion in Orthorhombic Perovskite Oxides”. In: *Phys. Rev. Lett.* 94 (6 2005), p. 065501.

[69] Truls Norby Reidar Haugsrud. *Proton Conduction in Rare-earth Ortho-Niobates and Ortho-Tantalates*. 2006.

[70] R. Yu and L. C. De Jonghe. In: *Phys. Chemistry C* 11 (2007), pp. 11003–11007.

[71] N. Adelstein et al. In: *Phys. Rev. B* 83.205104 (2011).

[72] Naoto Kitamura et al. “Electrical Conduction Properties of Sr-Doped LaPO4 and CePO4 under Oxidizing and Reducing Conditions”. In: *J. Electrochem. Soc* 152.4 (2005), pp. 658 –663.

[73] Isaac M. Markus et al. “Ab Initio Calculation of the Energy Landscape for Protons in DyPO4”. In: *ECS Transactions* 45.1 (20), pp. 111–115.

[74] R. D. Shannon. “Revised Effective Ionic Radii and Systematic Studies of Interatomic Distances in Halides and Chalcogenides”. In: *Acta Crystallographica Section A* 32.5 (1976), pp. 751–767.

[75] W.O. Milligan et al. In: *Inorg. Chem Acta.* 70.133 (1983).

[76] K. Toyoura et al. In: *J. Phys. Chem C* 116 (2012), pp. 19117–191124.

[77] Hannah L. Ray, Nana Zhao, and Lutgard C. De Jonghe. "Hole Percolation and Proton Conduction in Monazite Solid Solutions". In: *Electrochimica Acta* 78.0 (2012), pp. 294 –301.

[78] Daniel Sheppard et al. "A Generalized Solid-State Nudged Elastic Band Method". In: *The Journal of Chemical Physics* 136.7, 074103 (2012).

[79] Daniel Sheppard, Rye Terrell, and Graeme Henkelman. "Optimization Methods for Finding Minimum Energy Paths". In: *The Journal of Chemical Physics* 128.13, 134106 (2008).

[80] Daniel Sheppard and Graeme Henkelman. "Paths to Which the Nudged Elastic Band Converges". In: *Journal of Computational Chemistry* 32.8 (2011), pp. 1769–1771.

[81] Graeme Henkelman, Blas P. Uberuaga, and Hannes Jónsson. "A Climbing Image Nudged Elastic Band Method for Finding Saddle Points and Minimum Energy Paths". In: *The Journal of Chemical Physics* 113.22 (2000), pp. 9901–9904.

[82] M. S. Islam. "Ionic Transport in ABO Perovskite Oxides: A Computer Modelling Tour". In: *J. Mater. Chem.* 10 (4 2000), pp. 1027–1038.

[83] Francesco Giannici et al. "Dopants and Defects: Local Structure and Dynamics in Barium Cerates and Zirconates". In: *Solid State Ionics* 181.34 (2010), pp. 122 –125.

[84] P E Blöchl. "Projector augmented-wave method". In: *Phys. Rev. B* 50 (1994), pp. 17953–17979.

[85] G Kresse and D Joubert. "From Ultrasoft pseudopotentials to the projector augmented-wave method". In: *Phys. Rev. B* 59 (1999), pp. 1758–1775.

[86] G Kresse and J Furthmüller. "Efficient iterative schemes for ab initio total-energy calculations using a plane-wave basis set". In: *Phys. Rev. B* 54 (1996), pp. 11169–11186.

[87] G. Kresse and J. Furthmüller. "Efficiency of ab-initio Total Energy Calculations for Metals and Semiconductors Using a Plane-Wave Basis Set". In: *Computational Materials Science* 6.1 (1996), pp. 15 –50.

[88] John P. Perdew, Kieron Burke, and Matthias Ernzerhof. "Generalized Gradient Approximation Made Simple". In: *Phys. Rev. Lett.* 78 (7 1997), pp. 1396–1396.

[89] Hendrik J. Monkhorst and James D. Pack. "Special Points for Brillouin-zone Integrations". In: *Phys. Rev. B* 13 (12 1976), pp. 5188–5192.

[90] P. Sundell, M. Bjrketun, and G. Wahnstrm. In: *Phys. Rev. B* 76.094301 (2007).

[91] Q. Zhang et al. In: *Phys. Rev. Letters* 101.215902 (2008).

[92] A. Isaacson. In: *J. of Chemical Phys.* 117.13 (2002).

[93] A. Einstein. "Elementare Theorie der Brownschen Bewegung". In: *Zeitschrift fur Elektrochemie und angewandte physikalische Chemie* 14.17 (1908), pp. 235–239. ISSN: 0005-9021.

[94] M. von Smoluchowski. "Zur kinetischen Theorie der Brownschen Molekularbewegung und der Suspensionen". In: *Annalen der Physik* 326.14 (1906), pp. 756–780. ISSN: 1521-3889.

[95] M. A. Islam. "EinsteinSmoluchowski Diffusion Equation: A Discussion". In: *Physica Scripta* 70.2-3 (2004), p. 120.

[96] H. Schwarz and Z. Anorg. In: *Allg. Chem* 323.44 (1963).

[97] Jonathan M. Solomon et al. "First Principles Study of Pyrophosphate Defects and Dopant-defect Interactions in Stronium-doped Lanthanum Orthophosphate". In: *J. Mater. Chem. A* 2 (4 2014), pp. 1047–1053.

[98] Nicole Adelstein et al. "First-principles Studies of Proton-Ba Interactions in Doped LaPO4". In: *J. Mater. Chem.* 22 (9 2012), pp. 3758–3763.

[99] Taku Onishi and Trygve Helgaker. "A Theoretical Study on Proton Conduction Mechanism in BaZrO3 Perovskite". English. In: *Advances in Quantum Methods and Applications in Chemistry, Physics, and Biology*. Vol. 27. Progress in Theoretical Chemistry and Physics. Springer International Publishing, 2013, pp. 233–248. ISBN: 978-3-319-01528-6.

[100] A T Bell. "The impact of nanoscience on heterogeneous catalysis". In: *Science (80-.).* 299 (2003), pp. 1688–1691.

[101] M S Chen and D W Goodman. "The structure of catalytically active gold on titania". In: *Science (80-.).* 306 (2004), pp. 252–255.

[102] C A Cadigan. "Nanoscale (111) faceted rock-salt metal oxides in catalysis". In: *Catal. Sci. Technol.* 3 (2013), pp. 900–911.

[103] H Zheng et al. "Correlation between dissolution behavior and electrochemical cycling performance for LiNi1/3Co1/3Mn1/3O2-based cells". In: *J. Power Sources* 207 (2012), pp. 134–140.

[104] A Boulineau et al. "First evidence of manganese-nickel segregation and densification upon cycling in Li-Rich layered oxides for lithium batteries". In: *Nano Lett.* 13 (2013), pp. 3857–3863.

[105] Y Toda. "Activation and splitting of carbon dioxide on the surface of an inorganic electride material". In: *Nat. Commun.* 4 (2013), p. 2378.

[106] X Chen et al. "Increasing solar absorption for photocatalysis with black hydrogenated titanium dioxide nanocrystals". In: *Science (80-.).* 331 (2011), pp. 746–750.

[107] M M Doeff et al. "Effect of surface carbon structure on the electrochemical performance of LiFePO4". In: *Electrochem. Solid-State Lett.* 6 (2003), A207–A209.

[108] V R Stamenkovic et al. "Effect of surface composition on electronic structure, stability, and electrocatalytic properties of Pt-transition metal alloys: Pt-skin versus Pt-skeleton surfaces". In: *J. Am. Chem. Soc.* 128 (2006), pp. 8813–8819.

[109] X Lu. "New insight into the atomic structure of electrochemically delithiated O3-Li(1-x)CoO2 (0x0.5) nanoparticles". In: *Nano Lett.* 12 (2012), pp. 6192–6197.

[110] S.-K. Jung. "Understanding the degradation mechanisms of LiNi0.5Co0.2Mn0.3O2 cathode material in lithium ion batteries". In: *Adv. Energy Mater.* 4 (2014), p. 1300787.

[111] K Leung. "Using atomic layer deposition to hinder solvent decomposition in lithium ion batteries: first-principles modeling and experimental studies". In: *J. Am. Chem. Soc.* 133 (2011), pp. 14741–14754.

[112] X Zhang. "Structural and electrochemical study of Al2O3 and TiO2 coated Li1.2Ni0.13Mn0.54Co0.13 cathode material using ALD". In: *Adv. Energy Mater.* 3 (2013), pp. 1299–1307.

[113] K.-W. Nam. "Combining in situ synchrotron x-ray diffraction and absorption techniques with transmission electron microscopy to study the origin of thermal instability in overcharged cathode materials for lithium-ion batteries". In: *Adv. Funct. Mater.* 23 (2013), pp. 1047–1063.

[114] C R Fell. "Correlation between oxygen vacancy, microstrain, and cation distribution in lithium-excess layered oxides during the first electrochemical cycle". In: *Chem. Mater.* 25 (2013), pp. 1621–1629.

[115] M M Thackeray. "Li2MnO3-stabilized LiMO2 (M=Mn, Ni, Co) electrodes for lithium-ion batteries". In: *J. Mater. Chem.* 17 (2007), pp. 3112–3125.

[116] B Xu et al. "Identifying surface structural changes in layered Li-excess nickel manganese oxides in high voltage lithium ion batteries: a joint experimental and theoretical study". In: *Energy Environ. Sci.* 4 (2011), pp. 2223–2233.

[117] K C Kam et al. "Electrochemical and physical properties of Ti-substituted layered nickel manganese cobalt oxide (NMC) cathode materials". In: *J. Electrochem. Soc.* 159 (2012), A1383–A1392.

[118] K C Kam and M M Doeff. "Aliovalent titanium substitution in layered mixed Li NiMnCo oxides for lithium battery applications". In: *J. Mater. Chem.* 21 (2011), pp. 9991–9993.

[119] H Yu and H Zhou. "High-energy cathode materials (Li2MnO3LiMO2) for lithium-ion batteries". In: *J. Phys. Chem. Lett.* 4 (2013), pp. 1268–1280.

[120] D Mohanty. "Structural transformation of a lithium-rich Li1.2Co0.1Mn0.55Ni0.15O2 cathode during high voltage cycling resolved by in situ X-ray diffraction". In: *J. Power Sources* 229 (2013), pp. 239–248.

[121] M M Thackeray, C Wolverton, and E D Isaacs. "Electrical energy storage for transportationapproaching the limits of, and going beyond, lithium-ion batteries". In: *Energy Environ. Sci.* 5 (2012), pp. 7854–7863.

[122] A R Armstrong. "Demonstrating oxygen loss and associated structural reorganization in the lithium battery cathode Li[Ni0.2Li0.2Mn0.6]O2". In: *J. Am. Chem. Soc.* 128 (2006), pp. 8694–8698.

[123] M Jiang et al. “Electrochemical and structural study of the layered, Li-Excess lithium-ion battery electrode material Li[Li1/9Ni1/3Mn5/9]O2”. In: *Chem. Mater.* 21 (2009), pp. 2733–2745.

[124] M Gu. “Formation of the spinel phase in the layered composite cathode used in Li-ion batteries”. In: *ACS Nano* 7 (2013), pp. 760–767.

[125] N Tran. “Mechanisms associated with the plateau observed at high voltage for the overlithiated Li1.12(Ni0.425Mn0.425Co0.15)0.88O2 system”. In: *Chem. Mater.* 20 (2008), pp. 4815–4825.

[126] R Wang. “Atomic structure of Li2MnO3 after partial delithiation and re-lithiation”. In: *Adv. Energy Mater.* 3 (2013), pp. 1358–1367.

[127] W C Chueh. “Intercalation pathway in many-particle LiFePO4 electrode revealed by nanoscale state-of-charge mapping”. In: *Nano Lett.* 13 (2013), pp. 866–872.

[128] S J Harris and P Lu. “Effects of inhomogeneitiesnanoscale to mesoscaleon the durability of Li-Ion batteries”. In: *J. Phys. Chem. C* 117 (2013), pp. 6481–6492.

[129] M Kerlau et al. “Studies of local degradation phenomena in composite cathodes for lithium-ion batteries”. In: *Electrochim. Acta* 52 (2007), pp. 5422–5429.

[130] G Kresse and J Furthmüller. “Efficiency of ab initio total energy calculations for metals and semiconductors using a plane-wave basis set”. In: *Comp. Mater. Sci.* 6 (1996), pp. 15–50.

[131] G Kresse and J Hafner. “Ab initio molecular dynamics for liquid metals”. In: *Phys. Rev. B* 47 (1993), pp. 558–561.

[132] J P Perdew, K Burke, and M Ernzerhof. “Generalized gradient approximation made simple”. In: *Phys. Rev. Lett.* 77 (1996), pp. 3865–3868.

[133] S L Dudarev et al. “Electron-energy-loss spectra and the structural stability of nickel oxide: an LSDA+U study”. In: *Phys. Rev. B* 57 (1998), pp. 1505–1509.

[134] Y S Meng and M Dompablo. “First principles computational materials design for energy storage materials in lithium ion batteries”. In: *Energy Environ. Sci.* 2 (2009), pp. 589–609.

[135] F Zhou et al. “First-principles prediction of redox potentials in transition-metal compounds withLDA+U”. In: *Phys. Rev. B* 70 (2004), p. 235121.

[136] F Lin. “Origin of electrochromism in high-performing nanocomposite nickel oxide”. In: *ACS Appl. Mater. Interfaces* 5 (2013), pp. 3643–3649.

[137] F Lin. “Hole doping in Al-containing nickel oxide materials to improve electrochromic performance”. In: *ACS Appl. Mater. Interfaces* 5 (2013), pp. 301–309.

[138] J Graetz et al. “White lines and d-band occupancy for the 3d transition-metal oxides and lithiumtransition-metal oxides”. In: *Phys. Rev. B* 69 (2004), p. 235103.

[139] M Van Veenendaal and G Sawatzky. "Doping dependence of Ni 2p X-ray-absorption spectra of MxNi1-xO (M=Li,Na)". In: *Phys. Rev. B* 50 (1994), pp. 11326–11331.

[140] B Gilbert. "Multiple scattering calculations of bonding and X-ray absorption spectroscopy of manganese oxides". In: *J. Phys. Chem. A* 107 (2003), pp. 2839–2847.

[141] S Hy et al. "Soft X-ray absorption spectroscopic and Raman studies on Li1.2Ni0.2Mn0.6O2 for lithium-ion batteries". In: *J. Phys. Chem. C* 116 (2012), pp. 25242–25247.

[142] W.-S. Yoon. "Oxygen contribution on Li-Ion intercalationdeintercalation in LiCoO2 investigated by O K-Edge and Co L-Edge X-ray absorption spectroscopy". In: *J. Phys. Chem. B* 106 (2002), pp. 2526–2532.

[143] Z Hu. "Hole distribution between the Ni 3d and O 2p orbitals in Nd2-xSrxNiO4-δ". In: *Phys. Rev. B* 61 (2000), pp. 3739–3744.

[144] W.-S. Yoon. "Investigation of the charge compensation mechanism on the electrochemically Li-Ion deintercalated Li1-xCo1/3Ni1/3Mn1/3O2 electrode system by combination of soft and hard X-ray absorption spectroscopy". In: *J. Am. Chem. Soc.* 127 (2005), pp. 17479–17487.

[145] B H Frazer et al. "The probing depth of total electron yield in the sub-keV range: TEY-XAS and X-PEEM". In: *Surf. Sci.* 537 (2003), pp. 161–167.

[146] Y Liang. "Covalent hybrid of spinel manganese-cobalt oxide and graphene as advanced oxygen reduction electrocatalysts". In: *J. Am. Chem. Soc.* 134 (2012), pp. 3517–3523.

[147] J Zheng. "Corrosion/fragmentation of layered composite cathode and related capacity/voltage fading during cycling process". In: *Nano Lett.* 13 (2013), pp. 3824–3830.

[148] D Aurbach. "Capacity fading of LixMn2O4 spinel electrodes studied by XRD and electroanalytical techniques". In: *J. Power Sources* 81 (1999), pp. 472–479.

[149] John B Goodenough and Youngsik Kim. "Challenges for Rechargeable Li Batteries". In: *Chem. Mater.* 22.3 (2010), pp. 587–603. ISSN: 08974756.

[150] S.K. Martha et al. "A short review on surface chemical aspects of Li batteries: A key for a good performance". In: *J. Power Sources* 189.1 (Apr. 2009), pp. 288–296. ISSN: 03787753.

[151] Won-Sub Yoon et al. "A comparative study on structural changes of LiCo1/3Ni1/3Mn1/3O2 and $LiNi_{0.8}Co_{0.15}Al_{0.05}O_2$ during first charge using in situ XRD". In: *Electrochem. commun.* 8.8 (Aug. 2006), pp. 1257–1262. ISSN: 13882481.

[152] P Whitfield et al. "Investigation of possible superstructure and cation disorder in the lithium battery cathode material LiCo1/3Ni1/3Mn1/3O2 using neutron and anomalous dispersion powder diffraction". In: *Solid State Ionics* 176.5-6 (Feb. 2005), pp. 463–471. ISSN: 01672738.

[153] Cheng-chi Pan et al. "Recent development of LiNixCoyMnzO2: Impact of micro/nano structures for imparting improvements in lithium batteries". In: *Trans. Nonferrous Met. Soc. China* 23.1 (Jan. 2013), pp. 108–119. ISSN: 10036326.

[154] K. C. Kam et al. "Electrochemical and Physical Properties of Ti-Substituted Layered Nickel Manganese Cobalt Oxide (NMC) Cathode Materials". In: *J. Electrochem. Soc.* 159.8 (July 2012), A1383–A1392. ISSN: 0013-4651.

[155] Ying S. Meng et al. "Combining Ab Initio Computation with Experiments for Designing New Electrode Materials for Advanced Lithium Batteries: Li1Ni1/3Fe1/6Co1/6Mn1/3O2". In: *J. Electrochem. Soc.* 151.8 (2004), A1134. ISSN: 00134651.

[156] Yanhuai Ding et al. "Effect of rare earth elements doping on structure and electrochemical properties of LiNi1/3Co1/3Mn1/3O2 for lithium-ion battery". In: *Solid State Ionics* 178.13-14 (May 2007), pp. 967–971. ISSN: 01672738.

[157] Daotan Liu, Zhaoxiang Wang, and Liquan Chen. "Comparison of structure and electrochemistry of Al- and Fe-doped LiNi1/3Co1/3Mn1/3O2". In: *Electrochim. Acta* 51.20 (May 2006), pp. 4199–4203. ISSN: 00134686.

[158] Li Qin Wang et al. "Synthesis and electrochemical properties of Mo-doped Li(Ni1/3Mn1/3Co1/3)O2 cathode materials for Li-ion battery". In: *J. Power Sources* 162.2 (Nov. 2006), pp. 1367–1372. ISSN: 03787753.

[159] James D. Wilcox, Efrain E. Rodriguez, and Marca M. Doeff. "The Impact of Aluminum and Iron Substitution on the Structure and Electrochemistry of $Li(Ni_{0.4}Co_{0.2y}M_y]Mn_{0.4})O_2$ Materials". In: *J. Electrochem. Soc.* 156.12 (2009), A1011. ISSN: 00134651.

[160] James Wilcox, Sebastien Patoux, and Marca Doeff. "Structure and Electrochemistry of $LiNi_{13}Co_{13y}M_yMn_{13}O_2$ (M=Ti,Al,Fe) Positive Electrode Materials". In: *J. Electrochem. Soc.* 156.3 (2009), A192. ISSN: 00134651.

[161] a. Van der Ven and G. Ceder. "Ordering in $Li_x(Ni_{0.5}Mn_{0.5})O_2$ and its relation to charge capacity and electrochemical behavior in rechargeable lithium batteries". In: *Electrochem. commun.* 6.10 (Oct. 2004), pp. 1045–1050. ISSN: 13882481.

[162] Siqi Shi et al. "First-principles studies of cation-doped spinel LiMn2O4 for lithium ion batteries". In: *Phys. Rev. B* 67.11 (Mar. 2003), p. 115130. ISSN: 0163-1829.

[163] Gang Wu, Shunnian Wu, and Ping Wu. "Doping-Enhanced Lithium Diffusion in Lithium-Ion Batteries". In: *Phys. Rev. Lett.* 107.11 (Sept. 2011), p. 118302. ISSN: 0031-9007.

[164] Feng Lin et al. "Surface reconstruction and chemical evolution of stoichiometric layered cathode materials for lithium-ion batteries." In: *Nat. Commun.* 5 (Jan. 2014), p. 3529. ISSN: 2041-1723.

[165] Eunseok Lee and Kristin a. Persson. "Structural and Chemical Evolution of the Layered Li-Excess Li x MnO 3 as a Function of Li Content from First-Principles Calculations". In: *Adv. Energy Mater.* (June 2014), n/a–n/a. ISSN: 16146832.

[166] S L Dudarev et al. "Electron-energy-loss spectra and the structural stability of nickel oxide:" in: 57.3 (1998), pp. 1505–1509.

[167] F. Zhou et al. “First-principles prediction of redox potentials in transition-metal compounds with LDA+U”. In: *Phys. Rev. B* 70.23 (Dec. 2004), p. 235121. ISSN: 1098-0121.

[168] B J Hwang et al. “A Combined Computational / Experimental Study on”. In: 183 (2003), pp. 3676–3682.

[169] Yukinori Koyama et al. “Solid-State Chemistry and Electrochemistry of LiCo1/3Ni1/3Mn1/3O2 for Advanced Lithium-Ion Batteries”. In: *J. Electrochem. Soc.* 151.10 (2004), A1545. ISSN: 00134651.

[170] D. K. Swanson and R. C. Peterson. “Polyhedral volume calculations”. In: *The Canadian Mineralogist* 18.2 (1980), pp. 153–156. eprint: `http://www.canmin.org/content/18/2/153.full.pdf+html`.

[171] Koichi Momma and Fujio Izumi. “VESTA: a three-dimensional visualization system for electronic and structural analysis”. In: *Journal of Applied Crystallography* 41.3 (2008), pp. 653–658.

[172] Penghao Xiao et al. “Calculations of Oxygen Stability in Lithium-Rich Layered Cathodes”. In: *J. Phys. Chem. C* 116.44 (Nov. 2012), pp. 23201–23204. ISSN: 1932-7447.

[173] J. Choi and a. Manthiram. “Role of Chemical and Structural Stabilities on the Electrochemical Properties of Layered LiCo1/3Ni1/3Mn1/3O2 Cathodes”. In: *J. Electrochem. Soc.* 152.9 (2005), A1714. ISSN: 00134651.

[174] I Gyuk et al. “Grid Energy Storage”. In: (2013), pp. 1–67.

[175] Z Yang et al. “Electrochemical Energy Storage for Green Grid”. In: *Chem. Rev.* 111 (2011), pp. 3577–3613.

[176] Verónica Palomares et al. “Na-ion Batteries, Recent Advances and Present Challenges to Become Low Cost Energy Storage Systems”. In: *Energy Environ. Sci.* 5.3 (2012), p. 5884. ISSN: 1754-5692.

[177] V L Chevrier and G Ceder. “Challenges for Na-ion Negative Electrodes”. In: *J. Electrochem. Soc.* 158.9 (2011), pp. 1011–1014.

[178] D. a. Stevens and J. R. Dahn. “High Capacity Anode Materials for Rechargeable Sodium-Ion Batteries”. In: *J. Electrochem. Soc.* 147.4 (2000), p. 1271. ISSN: 00134651.

[179] M. Saiful Islam and Craig A. J. Fisher. “Lithium and Sodium Battery Cathode Materials: Computational Insights Into Voltage, Diffusion and Nanostructural properties”. In: *Chem. Soc. Rev.* 43 (1 2014), pp. 185–204.

[180] Ashish Rudola et al. “$Na_2Ti_3O_7$: An Intercalation Based Anode for Sodium-ion Battery Applications”. In: *J. Mater. Chem. A* 1.7 (2013), p. 2653. ISSN: 2050-7488.

[181] Shaohua Guo et al. “High-performance Symmetric Sodium-ion Batteries Using a New, Bipolar O3-type Material, $Na_{0.8}Ni_{0.4}Ti_{0.6}O_2$”. In: *Energy Environ. Sci.* 8 (4 2015), pp. 1237–1244. ISSN: 1754-5692.

[182] Corinne Arrouvel, Stephen C. Parker, and M. Saiful Islam. "Lithium Insertion and Transport in the TiO_2-β Anode Material: A Computational Study". In: *Chem. Mater.* 21.20 (Oct. 2009), pp. 4778–4783. ISSN: 0897-4756.

[183] Mona Shirpour, Jordi Cabana, and Marca Doeff. "New Materials Based on a Layered Sodium Titanate for Dual Electrochemical Na and Li Intercalation Systems". In: *Energy Environ. Sci.* 6.8 (2013), p. 2538. ISSN: 1754-5692.

[184] Mona Shirpour, Jordi Cabana, and Marca Doeff. "Lepidocrocite-type Layered Titanate Structures: New Lithium and Sodium Ion Intercalation Anode Materials". In: *Chemistry of Materials* 26.8 (2014), pp. 2502–2512.

[185] Premkumar Senguttuvan and M Rosa Palacín. "$Na_2Ti_3O_7$: Lowest Voltage Ever Reported Oxide Insertion Electrode for Sodium Ion Batteries". In: (2011), pp. 4109–4111.

[186] Takayoshi Sasaki et al. "A Mixed Alkali Metal Titanate with the Lepidocrocite-like Layered Structure. Preparation, Crystal Structure, Protonic Form, and Acid-Base Intercalation Properties". In: *Chem. Mater.* 10.12 (1998), pp. 4123–4128. ISSN: 0897-4756.

[187] Tao Gao, Helmer Fjellvag, and Poul Norby. "Protonic Titanate Derived from $Cs_xTi_{2-x/2}Mg_{x/2}O_4$ (x = 0.7) with Lepidocrocite-type Layered Structure". In: *J. Mater. Chem.* 19 (6 2009), pp. 787–794.

[188] D. Groult, C. Mercey, and B. Raveau. "Nouveaux Oxydes $àDtructureenFeuillets$: $LesTitanatesdePotassiumnon - stoechiométriquesK_xM_yTi_{2-y}O_4$". In: *Journal of Solid State Chemistry* 32.3 (1980), pp. 289 –296. ISSN: 0022-4596.

[189] A. F. Reid, W. G. Mumme, and A. D. Wadsley. "A New Class of Compound $M_x^+A_x^{3+}Ti_{2-x}O_4$ ($0.60 < x < 0.80$) Typified by $Rb_xMn_xTi_{2-x}O_4$". In: *Acta Crystallogr. Sect. B Struct. Crystallogr. Cryst. Chem.* 24.9 (1968), pp. 1228–1233. ISSN: 05677408.

[190] Takayoshi Sasaki et al. "Preparation and Acid-Base Properties of a Protonated Titanate with the Lepidocrocite-like Layer Structure". In: *Chemistry of Materials* 7.5 (1995), pp. 1001–1007.

[191] W.A. England, J.B. Goodenough, and P.J. Wiseman. "Ion-exchange Reactions of Mixed Oxides". In: *Journal of Solid State Chemistry* 49.3 (1983), pp. 289 –299. ISSN: 0022-4596.

[192] Kong-yao Chen et al. "Carbon Coated $K_{0.8}Ti_{1.73}Li_{0.27}O_4$: A Novel Anode Material for Sodium-ion Batteries with a Long Cycle Life." In: *Chem. Commun. (Camb).* 51.9 (Jan. 2015), pp. 1608–11. ISSN: 1364-548X.

[193] John P. Perdew, Kieron Burke, and Matthias Ernzerhof. "Generalized Gradient Approximation Made Simple". In: *Phys. Rev. Lett.* 77 (18 1996), pp. 3865–3868.

[194] G. Kresse and D. Joubert. "From Ultrasoft Pseudopotentials to the Projector Augmented-wave Method". In: *Phys. Rev. B* 59 (3 1999), pp. 1758–1775.

[195] P. E. Blöchl. "Projector Augmented-wave Method". In: *Phys. Rev. B* 50 (24 1994), pp. 17953–17979.

[196] G. Kresse and J. Furthmüller. "Efficient Iterative Schemes for *ab initio* Total-energy Calculations Using a Plane-wave Basis Set". In: *Phys. Rev. B* 54 (16 1996), pp. 11169–11186.

[197] Stefan Grimme. "Semiempirical GGA-type density functional constructed with a long-range dispersion correction". In: *Journal of Computational Chemistry* 27.15 (2006), pp. 1787–1799. ISSN: 1096-987X.

[198] Benjamin J. Morgan and Graeme W. Watson. "GGA + U Description of Lithium Intercalation into Anatase TiO_2". In: *Phys. Rev. B* 82.14 (Oct. 2010), p. 144119. ISSN: 1098-0121.

[199] Ying Shirley Meng and M. Elena Arroyo-de Dompablo. "First principles computational materials design for energy storage materials in lithium ion batteries". In: *Energy Environ. Sci.* 2.6 (2009), p. 589. ISSN: 1754-5692.

[200] Daniel Sheppard et al. "A Generalized Solid-state Nudged Elastic Band Method". In: *The Journal of Chemical Physics* 136.7 (2012), p. 074103.

[201] Daniel Sheppard and Graeme Henkelman. "Paths to Which the Nudged Elastic Band Converges". In: *Journal of Computational Chemistry* 32.8 (2011), pp. 1769–1771. ISSN: 1096-987X.

[202] Daniel Sheppard, Rye Terrell, and Graeme Henkelman. "Optimization Methods for Finding Minimum Energy Paths". In: *The Journal of Chemical Physics* 128.13 (2008), p. 134106.

[203] Graeme Henkelman and Hannes Jónsson. "Improved Tangent Estimate in the Nudged Elastic Band Method for Finding Minimum Energy Paths and Saddle Points". In: *The Journal of Chemical Physics* 113.22 (2000), pp. 9978–9985.

[204] A Katogi et al. "Electrochemical Performance of C-Centered Lepidocrocite-Type Titanate for Na-Ion Battery". In: *18th International Meeting on Lithium Batteries (June 19-24, 2016)*. Ecs. 2016.

[205] Lorenzo Grande et al. "The lithium air battery: Still an emerging system or a practical reality?" In: *Adv. Mater.* 27.5 (2015), pp. 784–800. ISSN: 1521-4095.

[206] Bryan D. McCloskey et al. "On the mechanism of nonaqueous Li-O_2 electrochemistry on C and its kinetic overpotentials: Some implications for Li-air batteries". In: *J. Phys. Chem. C* 116.45 (2012), pp. 23897–23905. ISSN: 19327447.

[207] V Viswanathan et al. "Li-O_2 kinetic overpotentials: Tafel plots from experiment and first-principles theory". In: *J. Phys. Chem. Lett.* 4 (2013), pp. 556–560.

[208] Muhammed M. Ottakam Thotiyl et al. "The carbon electrode in nonaqueous Li-O_2 cells". In: *J. Am. Chem. Soc.* 135.1 (2013), pp. 494–500. ISSN: 00027863.

[209] Jeannette M. García, Hans W. Horn, and Julia E. Rice. "Dominant decomposition pathways for ethereal solvents in Li-O_2 batteries". In: *J. Phys. Chem. Lett.* 6.10 (2015), pp. 1795–1799. ISSN: 1948-7185.

[210] Bryan D. McCloskey et al. "Combining accurate O_2 and Li_2O_2 assays to separate discharge and charge stability limitations in nonaqueous Li-O_2 Batteries". In: *J. Phys. Chem. Lett.* 4.17 (2013), pp. 2989–2993. ISSN: 19487185.

[211] Liumin Suo et al. "A new class of solvent-in-salt electrolyte for high-energy rechargeable metallic lithium batteries." In: *Nat. Commun.* 4 (2013), p. 1481. ISSN: 2041-1723.

[212] Jiangfeng Qian et al. "High rate and stable cycling of lithium metal anode". In: *Nat. Commun.* 6 (2015), p. 6362. ISSN: 2041-1723.

[213] Yuki Yamada et al. "Unusual stability of acetonitrile-based superconcentrated electrolytes for fast-charging lithium-ion batteries". In: *J. Am. Chem. Soc.* 136.13 (2014), pp. 5039–5046. ISSN: 15205126.

[214] Giuseppe Antonio Elia et al. "Role of the lithium salt in the performance of lithium-oxygen batteries: A comparative study". In: *ChemElectroChem* 1.1 (2014), pp. 47–50. ISSN: 21960216.

[215] Yuxiang Hu et al. "Size effect of lithium peroxide on charging performance of Li-O_2 batteries". In: *Nanoscale* 600 (2014), pp. 177–180.

[216] H Beyer et al. "Thermal and electrochemical decomposition of lithium peroxide in non-catalyzed carbon cathodes for Li-air batteries." In: *Phys. Chem. Chem. Phys.* 15.26 (2013), pp. 11025–37. ISSN: 1463-9084.

[217] Colin M. Burke et al. "Enhancing electrochemical intermediate solvation through electrolyte anion selection to increase nonaqueous Li-O_2 battery capacity". In: *Proc. Natl. Acad. Sci.* 112.30 (2015), p. 201505728. ISSN: 0027-8424.

[218] Iromie Gunasekaraa et al. "A study of the influence of lithium salt anions on oxygen reduction reactions in Li-Air batteries". In: *J. Electrochem Soc.* 162 (6 2015), A1055–A1065.

[219] Stefano Meini et al. "The role of electrolyte solvent stability and electrolyte impurities in the electrooxidation of Li_2O_2 in Li-O_2 batteries". In: *J. Electrochem. Soc.* 161.9 (2014), A1306–A1314. ISSN: 0013-4651.

[220] B. D. McCloskey et al. "Limitations in rechargeability of Li-O_2 batteries and possible origins". In: *J. Phys. Chem. Lett.* 3.20 (2012), pp. 3043–3047.

[221] Bryan D. McCloskey et al. "Solvents critical role in nonaqueous lithium oxygen battery". In: *J. Phys. Chem. Lett.* 2 (2011), pp. 1161–1166. ISSN: 1948-7185.

[222] M.W. Schmidt. "General atomic and molecular electronic structure system". In: *J. Comput. Chem.* 14.11 (1993), pp. 1347–1363. ISSN: 1096-987X.

[223] A. Vogel et al. *Practical Organic Chemistry*. Vol. 5th. 1989.

[224] Raphael F. Ribeiro et al. “Use of solution-phase vibrational frequencies in continuum models for the free energy of solvation”. In: *J. Phys. Chem. B* 115.49 (2011), pp. 14556–14562. ISSN: 15206106.

[225] Won-jin Kwak et al. “A Mo_2C/Carbon nanotube composite cathode for lithium oxygen batteries with high energy efficiency and long cycle life”. In: *ACS Nano* 9.4 (2015), pp. 4129–4137. ISSN: 1936-0851.

[226] Jun Lu et al. “A nanostructured cathode architecture for low charge overpotential in lithium-oxygen batteries.” In: *Nat. Commun.* 4 (2013), p. 2383. ISSN: 2041-1723.

[227] Ken Sakaushi, Tim-Patrick Fellinger, and Markus Antonietti. “Bifunctional metal-free catalysis of mesoporous noble carbons for oxygen reduction and evolution reactions”. In: *ChemSusChem* 8.7 (2015), pp. 1156–1160. ISSN: 1864-564X.

[228] Bryan D. McCloskey et al. “On the efficacy of electrocatalysis in nonaqueous Li-O_2 batteries”. In: *Journal of the American Chemical Society* 133.45 (2011), pp. 18038–18041.

[229] Sampson Lau and Lynden A. Archer. “Nucleation and growth of lithium peroxide in the Li-O_2 battery”. In: *Nano Letters* 15.9 (2015), pp. 5995–6002.

[230] Won-sub Yoon et al. “Investigation of the Charge Compensation Mechanism on the Electrode System by Combination of Soft and Hard X-ray Absorption Spectroscopy”. In: 1 (2005), pp. 17479–17487.

[231] Young-Ah Jeon et al. “A first principles investigation of new cathode materials for advanced lithium batteries”. In: *J. Electroceramics* 17.2-4 (Dec. 2006), pp. 667–671. ISSN: 1385-3449.